APPLIED COMPUTATIONAL ELECTROMAGNETICS SOCIETY JOURNAL

July 2014
Vol. 29 No. 7
ISSN 1054-4887

The ACES Journal is abstracted in INSPEC, in Engineering Index, DTIC, Science Citation Index Expanded, the Research Alert, and to Current Contents/Engineering, Computing & Technology.

The illustrations on the front cover have been obtained from the research groups at the Department of Electrical Engineering, The University of Mississippi.

THE APPLIED COMPUTATIONAL ELECTROMAGNETICS SOCIETY

JOURNAL

Vol. 29 No. 7 July 2014

TABLE OF CONTENTS

Uniaxial Dielectric Waveguide Filter Design Accounting for Losses Using Mode Matching Technique

Luke Murphy [1], Joseph Mautz [1], Mohsen Yazdani [1], Ercument Arvas [1], and Samir Tozin [2]

[1] Department of Electrical Engineering and Computer Science
Syracuse University, Syracuse, NY 13244, USA
lemurphy@syr.edu, jmautz@syr.edu, myazdani@syr.edu, earvas@syr.edu

[2] Deptartment of Electrical Engineering
Ajman University of Science and Technology, Ajman, UAE
s.tozin@ajman.ac.ae

Abstract **─** Dielectric filters can provide compact solutions for filter design problems. However, most dielectrics exhibit uniaxial properties, as well as, losses that will undoubtedly affect performance if not accounted for. This paper derives dispersion relations for lossy uniaxial media in dielectric waveguides and also accounts for lossy conducting walls. The waveguide discontinuity problem in the presence of lossy uniaxial media and finite conductivity waveguide walls, is calculated by mode matching technique and the results are applied to a Ka band filter. The design specifications for the proposed filter are a 32.5 GHz center frequency with 6%. Good agreement between simulated and measured results are shown.

Index Terms **─** Band-Pass Filter (BPF), Computer-Aided Design (CAD), dielectric waveguide filters, microwave filters, Mode-Matching Technique (MMT) and uniaxial media.

I. INTRODUCTION

Waveguide filters offer far superior performance to microstrip filters and dielectric filled waveguide filters significantly reduce waveguide filter size without sacrificing filter performance [1]. In addition to high performance, low manufacturing cost and small size, dielectric waveguide filters allow for flip-chip bonding; which makes for easy integration in millimeter-wave systems [2-3]. At millimeter-wave frequencies, dielectric waveguide filters also circumvent radiation loss; which is common in planar filters [4]. Recently, [5-6] use mode matching/hybrid method in the analysis of waveguide class filter problems. Wexler [7] first mentioned the advantages of choosing the Mode Matching Technique (MMT) versus all other methods when solving a class of waveguide problems. In [8-10], the MMT is applied to analyze dielectric waveguide and SIW filters as well as couplers. However, the MMT has never been applied to a lossy uniaxial dielectric waveguide filter with non-PEC walls. This paper will use the MMT to design and simulate a dielectric waveguide filter that is manufactured on a lossy uniaxial media with finite conductivity in the waveguide walls. The filter is designed in the Ka band, due to interest expressed by the manufacturing company that graciously manufactured and measured the filter free of charge.

II. DISPERSION RELATION IN LOSSY UNIAXIAL MEDIA

In order to account for a lossy dielectric in the MMT dispersion relations, Maxwell's equations must be modified. From [11], one finds Maxwell's equations for a conducting media. In this paper, it is assumed the relative permittivity tensor $\overline{\overline{\varepsilon_r}}$ takes the form of:

$$\overline{\overline{\varepsilon_r}} = \begin{bmatrix} \varepsilon & 0 & 0 \\ 0 & \varepsilon_y & 0 \\ 0 & 0 & \varepsilon \end{bmatrix}. \quad (1)$$

Submitted On: July 3, 2013
Accepted On: July 25, 2014

Replacing the relative permittivity tensor in (1) with that of the relative permittivity tensor for a lossy uniaxial media:

$$\overline{\overline{\varepsilon_{cd}}} = \begin{bmatrix} \varepsilon - j\tau\varepsilon & 0 & 0 \\ 0 & \varepsilon_y - j\tau\varepsilon_y & 0 \\ 0 & 0 & \varepsilon - j\tau\varepsilon \end{bmatrix}. \quad (2)$$

Putting (2) into Maxwell's equation, multiplying by the dot product of $\left(\bar{\bar{\varepsilon}}_{cd}^{-1}\right)^{-1}$ and then taking the curl, we obtain:

$$\nabla \times \left(\bar{\bar{\varepsilon}}_{cd}^{-1} \cdot (\nabla \times H)\right) = j\omega\varepsilon_0(\nabla \times E). \quad (3)$$

Substituting the $\nabla \times E$ term of Maxwell's equation into (3) gives:

$$\nabla \times \left(\bar{\bar{\alpha}}_{cd} \cdot (\nabla \times H)\right) = j\omega\varepsilon_0(-j\omega\mu_0 H), \quad (4)$$

where $\bar{\bar{\alpha}}_{cd} = \bar{\bar{\varepsilon}}_{cd}^{-1}$. Assuming propagation is in the $\hat{z}$ direction and solving for the k_z of the H_z components provide the dispersion relation. After some tedious but straight forward calculations, the $\hat{z}$-components of (4) are given by:

$$\left(\alpha_{22}\frac{\partial^2}{\partial x \partial z} - \alpha_{23}\frac{\partial^2}{\partial x \partial y} - \alpha_{12}\frac{\partial^2}{\partial y \partial z} + \alpha_{13}\frac{\partial^2}{\partial y^2}\right)H_x + \left(-\alpha_{12}\frac{\partial^2}{\partial x \partial z} + \alpha_{23}\frac{\partial^2}{\partial x^2} + \alpha_{11}\frac{\partial^2}{\partial y \partial z} - \alpha_{13}\frac{\partial^2}{\partial x \partial y}\right)H_y + \left(\alpha_{12}\frac{\partial^2}{\partial x \partial y} - \alpha_{22}\frac{\partial^2}{\partial x^2} - \alpha_{11}\frac{\partial^2}{\partial y^2} + \alpha_{12}\frac{\partial^2}{\partial x \partial y}\right)H_z = k_o^2 H_z. \quad (5)$$

It can be seen that the coupling effect of H_x and H_y makes the calculation of k_z difficult for uniaxial media. Later in this paper, MMT is carried out to analyze the TE_{10} mode. This assumption enforces the conditions on (5) such that $H_y = E_x = k_y = 0$. Under these conditions, using Gauss's law and knowing from calculations that $\alpha_{23} = \alpha_{12} = \alpha_{12} = 0$, simplifies (5) to:

$$-\alpha_{22}\frac{\partial^2}{\partial z^2}H_z - \alpha_{22}\frac{\partial^2}{\partial x^2}H_z - \alpha_{11}\frac{\partial^2}{\partial y^2}H_z = k_o^2 H_z. \quad (6)$$

Under the assumption in a waveguide, H_z is of the form $\cos(k_x x)\cos(k_y y)\,e^{-jk_z z}$, solving for k_z in (6) provides the dispersion relation for lossy media:

$$k_z = j\sqrt{k_x^2 - {k_0^2}/{\alpha_{22}}} = j\sqrt{k_x^2 - \left(\varepsilon_y - j\tau\varepsilon_y\right)k_0^2}, \quad (7)$$

where $k_x = m\pi/a$ and a is the x dimension of the dielectric waveguide in Fig. 1.

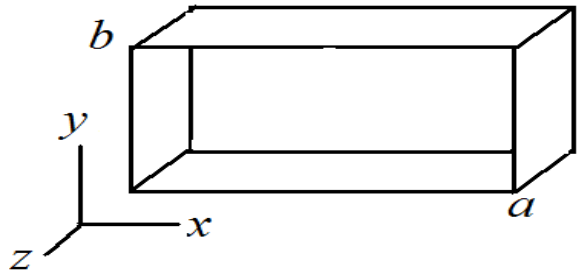

Fig. 1. Rectangular waveguide dimension reference.

III. LOSS IN CONDUCTOR WALLS

Most MMT calculations of the dielectric waveguides assume perfect conducting walls. In practice however, metallic walls exhibit a finite conductivity, σ_c and therefore cause attenuation of the signal. Under the assumption of TE_{10} mode of propagation, Kong's [12] perturbation method is used to calculate the attenuation for the waveguide wall dimensions that are defined in Fig. 1:

$$\alpha_c = \frac{P_w}{2P_f}, \quad (8)$$

where P_w represents the time-average power loss in the walls and P_f is the time-average power flowing through a cross section of the waveguide. P_f and P_w are defined as:

$$P_f = \frac{1}{2}Re\{\iint \boldsymbol{E} \times \boldsymbol{H}^* \, dx\, dy\}, \quad (9)$$

$$P_w = 2P_{w,x=0} + 2P_{w,y=0}, \quad (10)$$

where $P_{w,x=0}$ and $P_{w,y=0}$ is the power loss on the conducting walls at x=0 and y=0, respectively. The factor of two arises because all four walls must be considered. $P_{w,x=0}$ and $P_{w,y=0}$ are calculated by integrating the square of the current density on the waveguide wall multiplied by the surface resistance over the length of the wall, namely:

$$P_{w,x=0} = \int_0^b J_s(x=0) \cdot J_s^*(x=0) R_s \, dy, \quad (11)$$

$$P_{w,y=0} = \int_0^a J_s(y=0) \cdot J_s^*(y=0) R_s \, dx, \quad (12)$$

where $J_s = \hat{n} \times H$ and

$$R_s = \sqrt{\frac{\omega\mu_0}{2\sigma_c}}. \quad (13)$$

The assumption of only TE_{10} of mode propagation states only the existence of:

$$E_y = E_0 \sin\frac{\pi x}{a} e^{-jk_z z}, \quad (14)$$

$$H_x = Y_0 E_0 \sin\frac{\pi x}{a} e^{-jk_z z}, \quad (15)$$

$$H_z = Y_0 E_0 \cos\frac{\pi x}{a} e^{-jk_z z}, \quad (16)$$

in the waveguide, where E_0 is a wave amplitude coefficient and Y_0 is the admittance that relates the H-field amplitude to the E-field amplitude. Using (14)-(16) in (9) and (10) provides the attenuation constant, due to finite conductivity in the waveguide walls as:

$$\alpha_c = \frac{4Y_0 R_s(a+b)}{ab}. \quad (17)$$

It is important to note again that this attenuation constant is only valid for dominant TE_{10} mode analysis.

IV. MODE MATCHING FORMULATION

Figure 2 shows a waveguide step discontinuity. Assuming only TE_{m0} modes propagating in the waveguide, one can express the electric and magnetic fields in region A as a sum of the incident and reflected waves from the junction at z=0:

$$E_y^A = \sum_{m=1}^{M} A_m^+ \sin\frac{m\pi x}{a} e^{-\gamma_{am} z} + A_m^- \sin\frac{m\pi x}{a} e^{\gamma_{am} z}, \quad (18)$$

$$H_x^A = \sum_{m=1}^{M} Y_{am} A_m^- \sin\frac{m\pi x}{a} e^{\gamma_{am} z} - Y_{am} A_m^+ \sin\frac{m\pi x}{a} e^{-\gamma_{am} z}. \quad (19)$$

In region B, the fields are expressed as:

$$E_y^B = \sum_{n=1}^{K} B_n^+ \sin\frac{n\pi x}{c} e^{-\gamma_{bn} z} + B_n^- \sin\frac{n\pi x}{c} e^{\gamma_{bn} z}, \quad (20)$$

$$H_x^B = \sum_{n=1}^{K} Y_{bn} B_n^- \sin\frac{n\pi x}{c} e^{\gamma_{bn} z} - Y_{bn} B_n^+ \sin\frac{n\pi x}{c} e^{-\gamma_{bn} z}, \quad (21)$$

where in Fig. 2, A_m^+, B_m^- are unknown incident wave amplitude coefficients and A_m^-, B_m^+ are the reflected wave amplitudes in their respective region. In (14)-(16), the propagation constant for a respective region is:

$$\gamma_z = \alpha_c + jk_z, \quad (22)$$

where α_c and k_z are defined by (17) and (7), respectively, and

$$Y_i = \frac{k_z}{j\omega\mu_0}. \quad (23)$$

The propagation constant (k_z) and admittance (Y_i) are the two calculated values used in determining the unknown wave amplitude coefficients of the TE_{10} mode, because the MMT equations are only valid at z=0 and $0 \leq x \leq c$, they account for dielectric and conductor loss of wave amplitudes at this finite location. The propagation constant of (22) is also used later on to account for losses in the connecting sections of waveguides for the TE_{10} mode as well. Setting the tangential fields at z=0 equal to each other, assuming TE10 excitation and making use of mode orthonogality, one can calculate the transmission coefficients:

$$S_{21} = \left(\sum_{v=1}^{K}\left(\sum_{m=1}^{M}\left(\frac{2}{a} Y_{am} H_{mv} H_{mp}\right) + Y_{bv}\frac{c}{2}\delta_{vp}\right)\right)^{-1} (2Y_{a1}H_{1v})\ for\ p = 1,2,\ldots K. \quad (24)$$

The reflection coefficients are given by:

$$S_{11} = \frac{2}{a}\sum_{p=1}^{K}\left(H_{mp}S_{21}\right) - \delta_{m1} \quad \text{for } m = 1,2,\ldots M, \quad (25)$$

where

$$H_{ij} = \int_0^c \sin\frac{i\pi x}{a} \sin\frac{j\pi x}{c}\, dx, \quad (26)$$

where S_{21} are the transmission coefficients of the discontinuity, S_{11} are the reflection coefficients of the discontinuity, M are the number of modes in region A and K are the number of modes in region B. The reader is invited to explore [13] on MMT, in order to gain a full understanding on MMT formulation.

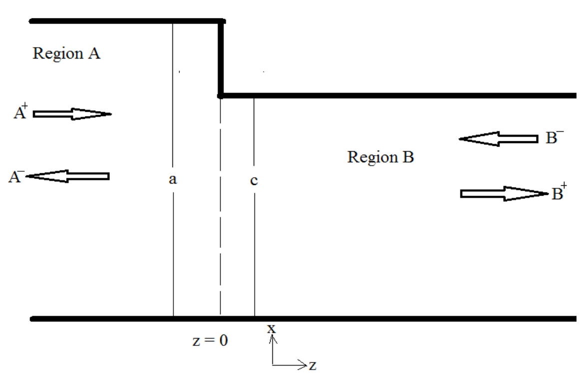

Fig. 2. Waveguide step discontinuity between region A and Region B.

V. FILTER DESIGN

A three pole filter with 6% bandwidth in the Ka band is designed using a dielectric with ε=67 and ε_y=61, due to expressed interest from the filter manufacturer. The filter is designed using Hong and Lancaster's [14] method to calculate filter coupling coefficients (k_{ij}) from g values.

This method provides coupling coefficients $k_{12}=k_{23}=0.107$. Using the resonant peak method of [14], coupling coefficients are then calculated and compared with ideal coupling coefficients to provide initial filter dimensions. Typically, the inductive coupling irises between resonators are kept thin with respect to waveguide dimensions, as shown by [15]. Bearing this in mind, Fig. 3 shows calculated coupling coefficients assuming the thickness (d) of the coupling irises is set to the minimum that manufacturing tolerances allow. One can see from Fig. 3, that if the dielectric is not treated as uniaxial, the coupling coefficients vary drastically. Using the results of Fig. 3 as a starting point and S-parameter theory to cascade the discontinuities with respective connecting waveguide sections, the filter dimensions are given in Fig. 4 after the first and third resonator lengths were optimized for return loss.

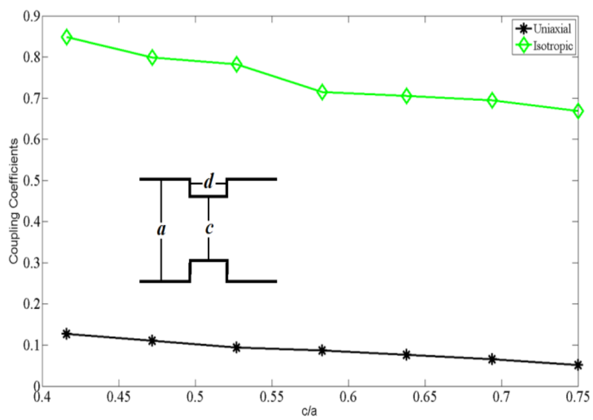

Fig. 3. Coupling coefficients for isotropic and uniaxial media for varying ratios of c/a and d=0.127 mm. Insert displays the junction and coordinate system under analysis.

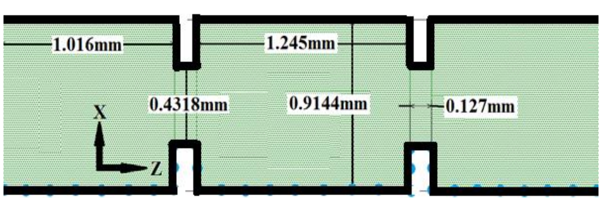

Fig. 4. Dimensions of initial filter.

VI. RESULTS

A narrowband waveguide filter is designed and simulated at 32.5 GHz. The dielectric is assumed to have a thickness of 0.254 mm, τ = 3e-4 and σ_c=3.5e7. The waveguide is excited with a TE_{10} mode using an optimized microstrip-to-waveguide transition, as was done in [16]. The exact dimensions of the transition are omitted at the request of the manufacture. The post-optimization results provided by the MMT are in Fig. 5, with measured filter performance in solid circles and results from a commercial FEM solver are also given for comparison (solid blue). The measured results of Fig. 5 show a VSWR of 2:1 or better from 31.6-33.8 GHz, with a center frequency of 32.68 GHz. The insertion loss is 6 dB or better in this band, with the passband ripple better than 1 dB peak-to-peak. It should be noted that according to the manufacturer 6 dB of insertion loss is acceptable. Figure 6 shows the manufactured filter above the word liberty on a US penny for size comparison. One can see good agreement between MMT and measured results. After analysis, it was discovered that the dimensions of the filter varied slightly from those in Fig. 4. These dimensional changes are noted in Fig. 6. It was also discovered that the donated substrate had higher dielectric loss and lower conductivity than initially estimated. However, when the adjusted losses and dimensional differences are accounted for in the MMT analysis, one can notice that there is now excellent agreement in Fig. 7 between the MMT and measured results.

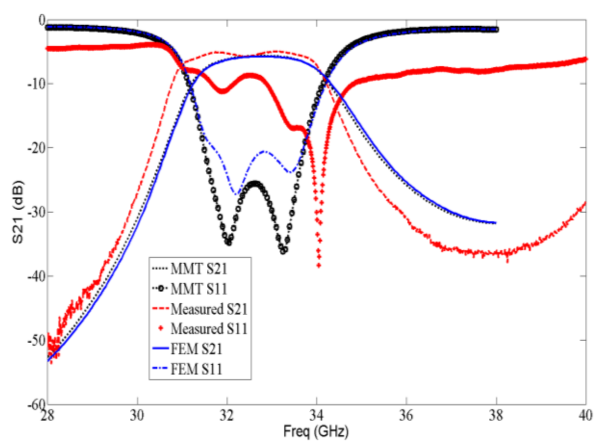

Fig. 5. Measured filter performance vs. simulated performance in black triangles.

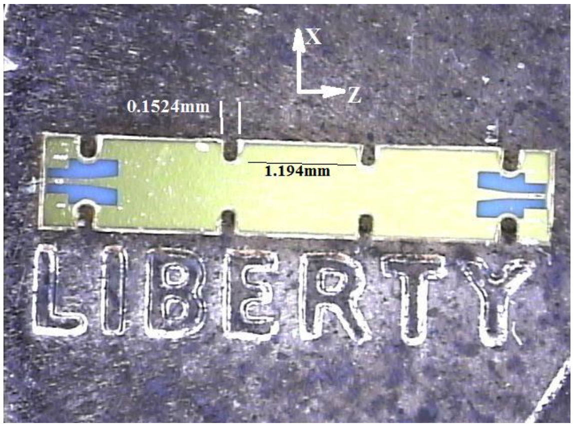

Fig. 6. Manufactured filter next to the word LIBERTY on a US penny for size comparison.

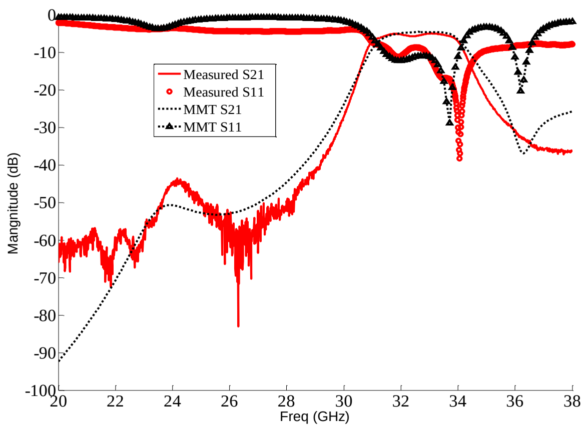

Fig. 7. Measured filter performance (solid circles) vs. simulated performance with adjusted dimension and loss numbers (black triangles).

VII. CONCLUSION

Derivations are presented for the propagation constant of a dielectric waveguide when the dielectric is assumed to exhibit uniaxial properties. Using this propagation constant with the MMT, a filter is designed, analyzed and manufactured. The MMT accounts for dielectric losses and conductor wall losses. It is shown that accounting for uniaxial media and losses in the analysis of dielectric filters using the MMT allows for accurate prediction of filter performance. The manufactured dielectric filter shows excellent agreement with simulated results.

ACKNOWLEDGEMENTS

The authors would like to thank Dielectric Laboratories for the donation of material and assistance in manufacturing. We would also like to thank Mark Carney for his assistance in debugging during testing.

REFERENCES

[1] C. Y. Change and W. C. Hsu, "Novel planar, square-shaped, dielectric-waveguide, single-, and dual-mode filters," *IEEE Trans. on Microwave Theory and Tech.*, vol. 50, no. 11, pp. 2527-2536, 2002.

[2] A. C. Kundu, "Broadband TEM-mode planar-rectangular dielectric waveguide bandpass filter and its miniaturization," *IEEE MTT-S Int. Microwave Symp. Dig.*, Phoenix, AZ, pp. 381-384, 2002.

[3] M. Ito, et al., "A 60-GHz-band planar dielectric waveguide filter for flip-chip modules," *IEEE Trans. on Microwave Theory and Tech.*, vol. 49, no. 12, pp. 2431-2436, 2001.

[4] H. C. Chen, et al., "All-planar dual-mode asymmetric filters at ka-band," *IEEE Microwave and Wireless Comp. Letters*, vol. 12, no. 3, pp. 111-113, 2003.

[5] S. Liu, et al., "Rectangular conducting waveguide filled with uniaxial anisotropic media: a modal analysis and dyadic green's function," *PIER*, vol. 25, pp. 111-129, 2000.

[6] P. Grassi, et al., "Analysis of inhomogeneously filled waveguide devices by a hybrid mode matching-finite element technique," *IEEE AP-S Int. Symp.*, vol. 2, pp. 161-164, June 2003.

[7] A. Wexler, "Solution of waveguide discontinuities by modal analysis," *In IEEE Trans. on MTT*, vol. 15, no. 9, pp. 508-517, September 1967.

[8] R. Rezaiesarlak, et al, "Hybrid of moment method and mode matching technique for full-wave analysis of SIW circuits," *ACES Journal*, vol. 26, no. 8, pp. 688-695, 2011.

[9] Z. Kordiboroujeni, et al, "Mode-matching design of substrate-integrated waveguide couplers," *Symps. on Electromag. Compatibility, Asia-Pacific*, pp. 701-704, 2012.

[10] J. Bornemann and F. Taringou, "Substrate-integrated waveguide filter design using mode-matching techniques," *Proc. of 41st European Microwave Confer.*, pp. 1-4, October 2011.

[11] R. F. Harrington, "Time-harmonic electromagnetic fields," *McGraw-Hill*, New York, 1961.

[12] J. A. Kong, "Electromagnetic wave theory," *EMW Publishing*, Massachusetts, 2005.
[13] T. Itoh, "Numerical techniques for microwave and millimeter-wave passive structures," 1st ed., *New York: Wiley-Interscience*, 1989.
[14] J. H. Hong and M. J. Lancaster, "Microstrip filters for RF/microwave applications," 1st ed., *New York: John Wiley & Sons, Inc.*, pp. 40-130, 2001.
[15] F. Arndt, et al, "Modal s-matrix method for the optimum design of inductively direct-coupled cavity filters," *IEE Proc. Micro., Ant. and Prop.*, vol. 133, no. 5, pp. 341-350, 1986.
[16] Z. Sotoodeh, et al, "A novel bandpass waveguide filter structure in SIW technology," *PIER*, vol. 2, pp. 141-148, 2008.

Luke Murphy received his B.Sc. degree from Rensselaer Polytechnic Institute, Troy, NY in 2007. In 2009 he earned his M.Sc. degree from Syracuse University, Syracuse, NY and is currently completing his Ph.D degree at Syracuse University. From 2010 he has interned and worked at Dielectric Laboratories, Inc. in Cazeonvia, NY designing RF filters and other passive RF components. His research interests are in electromagnetic theory, metamaterials and microwave devices.

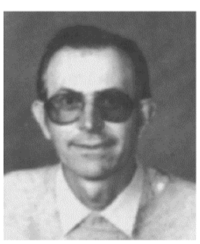

Joseph R. Mautz was born in Syracuse, NY, in 1939. He received his B.Sc., M.Sc. and Ph.D. degrees in Electrical Engineering from Syracuse University in 1961, 1965 and 1969, respectively. Until July 1993, he was a Research Associate with the Electrical Engineering and Computer Science Department, Syracuse University, where he worked on radiation and scattering problems. Currently, he is affiliated with the Electrical Engineering and Computer Science Department at the same university. His primary fields of interest are electromagnetic theory and applied mathematics.

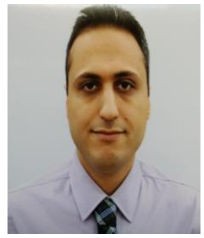

Mohsen Yazdani was born in Tehran, Iran. He received his Masters degree from Iran University of Science and Technology, Tehran, Iran. He earned his Ph.D. degree at Syracuse University, Syracuse, NY in 2014. He is currently working as a Post-Doc at UCLA, Los Angeles, CA. His research interests include electromagnetic scattering, antennas and microwave devices.

Ercument Arvas received his B.Sc. and M.Sc. degrees from the Middle East Technical University, Ankara, Turkey in 1976 and 1979, respectively, and the Ph.D. degree from Syracuse University, Syracuse, NY in 1983; all in Electrical Engineering. From 1984 to 1987, he was with the Electrical Engineering Department, Rochester Institute of Technology, Rochester, NY. In 1987, he joined the Electrical Engineering and Computer Science Department, Syracuse University, where he is currently a Professor in the Electrical Engineering and Computer Science Department. His research and teaching interests are in electromagnetic scattering and microwave devices.

Samir L. Tozin earned a B.S.E.E. degree from Seattle University in 1995 and his Ph.D. degree from Syracuse University in 2004. From 1997 to 2009, he was with Anaren Microwave in East Syracuse, New York. From 2002 to 2009, he taught Microwave Engineering courses at Syracuse University. He is currently working as an Assistant Professor at Ajman University of Science and Technology in the United Arab Emirates. His current interests are in the research and development of passive and active microwave devices as well as antennas.

Electromagnetic Shielding of Resonant Frequency-Selective Surfaces in Presence of Dipole Sources

G. Lovat, R. Araneo, and S. Celozzi

Department of Astronautical, Electrical and Energetic Engineering
University of Rome "Sapienza", Via Eudossiana 18, 00184 Roma, Italy
giampiero.lovat, rodolfo.araneo, salvatore.celozzi@uniroma1.it

Abstract **─** The shielding problem consisting in the interaction between a dipole source and a Frequency-Selective Surface (FSS) is investigated. The Array Scanning Method (ASM) is adopted to take into account all the propagating and evanescent waves, which constitute the spectrum of the dipole and all the propagating and evanescent Floquet modes, which constitute the spectrum of the diffracted field by the FSS. The main differences with respect to the shielding of a conventional plane-wave source are pointed out, especially in terms of resonant frequencies, operating bandwidth and transmission levels.

Index Terms **─** Electromagnetic shielding, frequency selective surfaces and periodic structures.

I. INTRODUCTION

Frequency Selective Surfaces (FSSs) are periodic structures along two dimensions, often planar. They may consist of either metallic elements or apertures cut in a metallic plate, periodically arranged in a two-dimensional (2-D) array; multi-layer lattices are generally considered. The main characteristic of an FSS is its capability to be effectively reflecting Electromagnetic (EM) fields in a given frequency range and almost completely transparent out of this interval, showing filtering properties. FSSs are attractive for many applications and can act as polarizers, filters, subreflectors, RAMs, superstrates for antennas, shields; e.g., [1]. The FSS EM behavior and performance mainly depend on the geometry of the single element and on the spatial periods; moreover, in general, they are also quite sensitive to the characteristics of the incident wave (incident angles and polarization, if a conventional plane-wave excitation is used) [2]. In recent years, in addition to the study of artificial periodic screens with high-pass behaviors [3], [4], many efforts have been spent in order to design FSSs with miniaturized elements, polarization and angular stability and multiband operation [5]-[11].

However, very often, the incident field has been typically assumed as that of a uniform plane wave; only recently, the interaction between a finite source (such as an elemental dipole) and an infinite periodic structure has been addressed [4], [12]-[18] since the conventional Floquet theory cannot be applied directly and some alternatives must be explored.

The novelty of the present investigation with respect to published papers is resumed as follows:

i) First of all, as far as we know, this is the first time that the interaction between a dipole source and a resonant infinite periodic screen is considered. In previous works, the considered periodic screens were basically high-pass structures with no resonant properties.

ii) The resonant behavior of the considered structures allows us to investigate how classical figures of merit, such as level of transmission, resonant frequency, resonant bandwidth, etc., change when a finite dipole source is considered instead of a classical plane-wave excitation. In fact, when the dipole is close to the periodic screen the evanescent part of its spectrum can strongly interact with the periodic screen; thus, spoiling the classical plane-wave response

iii) Some peculiar behaviors are pointed out when vertical dipoles are considered. While far-

Submitted On: October 2, 2013
Accepted On: July 14, 2014

interacting horizontal dipoles mainly behave as suitably polarized plane waves, far-interacting vertical dipoles do not have the corresponding plane-wave counterparts; so the response of the periodic screens to such sources may be particularly interesting.

In this paper, the shielding properties of resonant FSSs in the presence of dipole sources in their proximity are studied. The frequency-selective behavior is first studied in the presence of a conventional plane-wave excitation in order to point out the standard and generally considered response; then more realistic electric and magnetic dipole sources characterized by different distances and orientations are analyzed.

II. DESCRIPTION OF THE PROBLEM

The EM configuration is reported in Fig. 1. It consists of an incident far or near field (which can be either that of a uniform plane wave or that of a near electric or magnetic-dipole source, respectively) impinging on an FSS periodic along the x and y directions with spatial periods p_x and p_y.

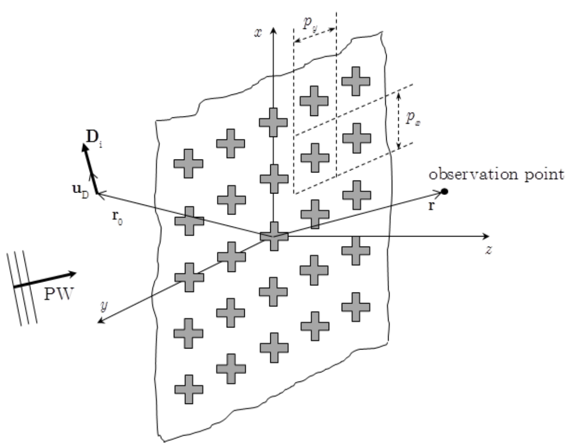

Fig. 1. Two-dimensional (2-D) periodic screen, excited either by a finite-dipole $\mathbf{D}_i$ or a plane-wave (PW) source.

The unit cell of the periodic FSS is constituted by Perfectly Conducting (PEC) elements or apertures cut in a PEC plane; a dielectric foam ($\varepsilon_r = 1$) is considered as host medium: different dielectric hosts call for more sophisticated numerical acceleration techniques [19], [20] and for simplicity are not considered here, since the main features are not affected by this choice (except when unconventional substrates are used [21]).

A time-harmonic dependence $e^{j\omega t}$ is assumed and suppressed throughout. The electric or magnetic shielding effectiveness (SE) is adopted as a performance parameter [22].

III. PLANE-WAVE EXCITATION

It is well known that in the presence of a plane-wave excitation (which is a particular type of Floquet-periodic source) the analysis can be simplified by restricting the computational domain (which in principle, is infinite) to a single unit cell by enforcing periodic boundary conditions and using a periodic Green's function [23]. The integral equation which describes the problem can next be obtained by enforcing the Electric-Field Integral Equation (EFIE); i.e., the null of the total tangential electric field on the PEC elements of the unit cell. The total electric field $\mathbf{E}_{\mathrm{tot}}$ is the sum of the incident plane-wave field $\mathbf{E}_{\mathrm{inc}}$ and the scattered field $\mathbf{E}_{\mathrm{sc}}$ given by:

$$\mathbf{E}_{\mathrm{sc}}\ \mathbf{r}\ = \int_S \underline{\mathbf{G}}_{\mathrm{p}}^{EJ}\ \mathbf{r},\mathbf{r}'\ \cdot \mathbf{J}_S\ \mathbf{r}'\ \mathrm{d}\mathbf{r}', \qquad (1)$$

where $\underline{\mathbf{G}}_{\mathrm{p}}^{EJ}$ is the EJ-type dyadic periodic Green's function, $\mathbf{J}_S$ is the unknown current density induced over the surface S of the conductors within the unit cell and $\mathbf{r}$ and $\mathbf{r}'$ are the vectors from the origin to the source and observation points, respectively. The solution of the EFIE can be obtained by expanding the unknown $\mathbf{J}_S$ through suitable vector basis functions and applying a Galerkin testing procedure for the final discretization. From the knowledge of $\mathbf{J}_S$, the scattered field $\mathbf{E}_{\mathrm{sc}}$ (and thus, the total field $\mathbf{E}_{\mathrm{tot}}$) can finally be obtained.

In dealing with FSSs constituted by arrays of apertures cut in a PEC plane, the aforementioned integral equation can still be constructed with the electric current density $\mathbf{J}_S$ defined on the PEC surface of the unit cell. As an alternative, the equivalence theorem may be applied by enforcing the continuity of the tangential magnetic field on the apertures of the unit cell surface *A*; thus, deriving an integral equation whose unknowns are equivalent magnetic currents $\mathbf{M}_A$. It is well-known that the kernel of the integral equation does not change; there is only a change in the unknown and in the incident field (the electric field in the former case, the magnetic field in the latter one).

Actually, to efficiently solve the derived integral equations by means of the MoM technique, it is numerically more convenient to recast them in a Mixed-Potential Integral Equation form (MPIE) [24], [25] by introducing the magnetic vector and electric scalar potentials $\mathbf{A}$ and V for electric sources $\mathbf{J}_S$ (and possibly the electric vector and magnetic scalar potentials $\mathbf{F}$ and W for magnetic sources $\mathbf{M}_A$), respectively; so that the convolution terms can be expressed as:

$$\begin{aligned}\mathbf{E}(\mathbf{J}) &= \underline{\mathbf{G}}^{EJ} \otimes \mathbf{J} = -j\omega\mathbf{A} - \nabla V = \\ &= -j\omega\underline{\mathbf{G}}^{A} \otimes \mathbf{J} + \frac{1}{j\omega}\nabla\left(G^{V} \otimes \nabla\cdot\mathbf{J}\right)\end{aligned}, \quad (2a)$$

$$\begin{aligned}\mathbf{H}(\mathbf{J}) &= \underline{\mathbf{G}}^{HJ} \otimes \mathbf{J} = \frac{1}{\mu_0}\nabla\times\mathbf{A} = \\ &= \frac{1}{\mu_0}\left(\nabla\times\underline{\mathbf{G}}^{A}\right)\otimes\mathbf{J}\end{aligned}, \quad (2b)$$

$$\begin{aligned}\mathbf{E}(\mathbf{M}) &= \underline{\mathbf{G}}^{EM} \otimes \mathbf{M} = -\frac{1}{\varepsilon_0}\nabla\times\mathbf{F} = \\ &= \frac{1}{\varepsilon_0}\left(\nabla\times\underline{\mathbf{G}}^{F}\right)\otimes\mathbf{M}\end{aligned}, \quad (2c)$$

$$\begin{aligned}\mathbf{H}(\mathbf{M}) &= \underline{\mathbf{G}}^{HM} \otimes \mathbf{M} = -j\omega\mathbf{F} - \nabla W = \\ &= -j\omega\underline{\mathbf{G}}^{F} \otimes \mathbf{M} + \frac{1}{j\omega}\nabla\left(G^{W} \otimes \nabla\cdot\mathbf{M}\right)\end{aligned}, \quad (2d)$$

where the symbol $\otimes$ denotes the superposition integral, while $\underline{\mathbf{G}}^{A,F}$ and $G^{V,W}$ are the potential periodic 2-D Green's functions for electric or magnetic currents and charges, respectively; calculated by means of the Ewald method, the spectral and spatial representations of the periodic Green's function are combined to obtain a final expression in terms of a sum of two fast-decaying Gaussian convergent series [24]-[26]. The Ewald method has efficiently been applied also for 1-D and 3-D periodic Green's functions [27], [28].

A standard MoM procedure is then considered; either the PEC parts or the apertures in the unit cell can be discretized through non-overlapping triangles and the unknown current densities ($\mathbf{J}_S$ or $\mathbf{M}_A$, respectively) can be expanded by a set of second-order subdomain basis functions, which provide a linear-normal/quadratic-tangent (LN/QT) representation of the vector quantities [29] and result more accurate and smoother than conventional RWG basis functions and first-order triangular patches (LL) [30]. All the singular terms present in the source integrals (proportional to $1/\left|\mathbf{r}-\mathbf{r}'\right|$) can be extracted and integrated analytically [31], while the remaining (source and testing) integrals can be computed by means of standard Gaussian formulas [32].

IV. DIPOLE EXCITATION

The first step in the application of the ASM is the expression of the finite source as a superposition of infinite auxiliary Floquet periodic sources having the same periods of the original periodic structure. The well-known Floquet theory [23] can then be applied to each elemental Floquet-periodic problem (FPP, characterized by the values of the phase shifts q_x and q_y); thus, restricting the computational domain to a unit cell. Once the auxiliary FPPs are solved, the solution of the original problem is reconstructed by superposition through the ASM identity. In fact, for 2-D periodic configurations, the ASM exploits the following identity:

$$\begin{aligned}\delta(\mathbf{r}-\mathbf{r}_0) &= p_{xy}\int_{-\frac{\pi}{p_y}}^{+\frac{\pi}{p_y}}\int_{-\frac{\pi}{p_x}}^{+\frac{\pi}{p_x}}\sum_{m,n=-\infty}^{+\infty}\delta(\mathbf{r}-\mathbf{r}_{mn})\,\cdot \\ &\cdot\, \mathrm{e}^{-j\left(q_x m p_x + q_y n p_y\right)}\,\mathrm{d}q_x\mathrm{d}q_y\end{aligned}, \quad (3)$$

where

$$p_{xy} = \frac{p_x p_y}{(2\pi)^2}, \quad (4)$$

$\delta(\bullet)$ is the Dirac delta generalized function, $\mathbf{r}_{mn} = \mathbf{r}_0 + \mathbf{p}_{mn}$, with $\mathbf{r}_0 = \mathbf{u}_x x_0 + \mathbf{u}_y y_0 + \mathbf{u}_z z_0$

and $\mathbf{p}_{mn} = \mathbf{u}_x m p_x + \mathbf{u}_y n p_y$. Therefore, the single aperiodic dipole source $\mathbf{D}_i$ (where $\mathbf{D}_i$ can be either $\mathbf{J}_i$ or $\mathbf{M}_i$) directed along the unit vector $\mathbf{u}_{\mathrm{D}}$ can be expressed as:

$$\mathbf{D}_i(\mathbf{r}) = D_0 \delta(\mathbf{r} - \mathbf{r}_0)\mathbf{u}_{\mathrm{D}} = \\ = p_{xy} \int_{-\frac{\pi}{p_y}}^{+\frac{\pi}{p_y}} \int_{-\frac{\pi}{p_x}}^{+\frac{\pi}{p_x}} \mathbf{D}_i^{\mathrm{FP}}(\mathbf{r}, q_x, q_y) \, \mathrm{d}q_x \mathrm{d}q_y, \quad (5)$$

with

$$\mathbf{D}_i^{\mathrm{FP}}(\mathbf{r}, q_x, q_y) = D_0 \sum_{m,n=-\infty}^{+\infty} \delta(\mathbf{r} - \mathbf{r}_{mn}) \cdot \\ \cdot \mathrm{e}^{-j(q_x m p_x + q_y n p_y)} \mathbf{u}_{\mathrm{D}}. \quad (6)$$

For each auxiliary source $\mathbf{D}_i^{\mathrm{FP}}$ with phase shifts q_x and q_y, we have a single FPP; which can be solved as described in the previous section. With respect to the canonical problem involving a plane-wave excitation, the only difference is the incident field, which is now produced by a 2-D phased array of dipoles in free space. The total field due to each auxiliary source $\mathbf{D}_i^{\mathrm{FP}}$ in the presence of the periodic structure is the sum of the incident field and of the field scattered by the periodic loading. The final step of the ASM procedure is the reconstruction of the total field produced by the dipole source through the superposition of the auxiliary total fields by means of the ASM identity (3).

Several details on the numerical implementation of the ASM for 2-D periodic structures can be found in [17]; features of the configurations considered in this work are presented in the next Section.

V. NUMERICAL RESULTS

Two different resonant FSSs are considered as case studies: a metallic Jerusalem-Cross (JC) and a Double-Loop (DL), shown in Figs. 2 (a) and 2 (b), respectively; with the relevant geometric parameters.

The structures have been designed in order to present the first resonant frequency at about 1.9 GHz.

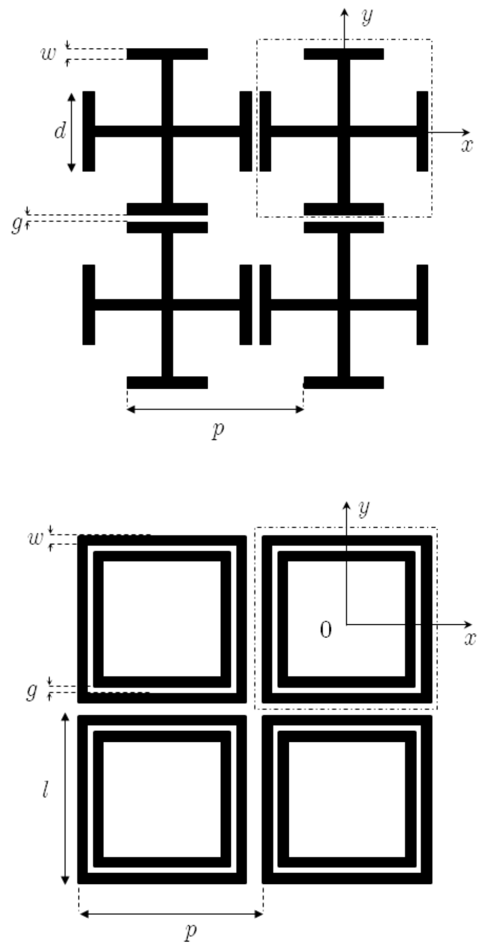

Fig. 2. Unit cells (dashed areas) of the two considered FSSs: Jerusalem-Cross (JC) and Double-Loop (DL). Parameters: p=3.44 cm, d=2.24 cm, w=0.16 cm and g=0.08 cm for the JC FSS and p=3.66 cm, l=3.33 cm, w=0.3 cm and g=0.3 cm for the DL FSS.

In all the reported results, both the dipole source and the observation point for SE evaluations have been located along the z axis (i.e., (x, y)=(0, 0), in the center of the unit cell); moreover, the observation point has also been placed in the far field at z>50 p, for both the structures. In Fig. 3, we report the SE of the JC for incident (a) TE and (b) TM plane waves at θ=0, π/6, π/3 as a function of frequency f along the ϕ=0 plane. As it can be seen, for TE incidence, the resonant frequency of the periodic screen is quite stable at f_{res}=1.9 GHz; whereas, for TM incidence is more sensitive to the incident angle, although it remains between 1.9 and 2 GHz.

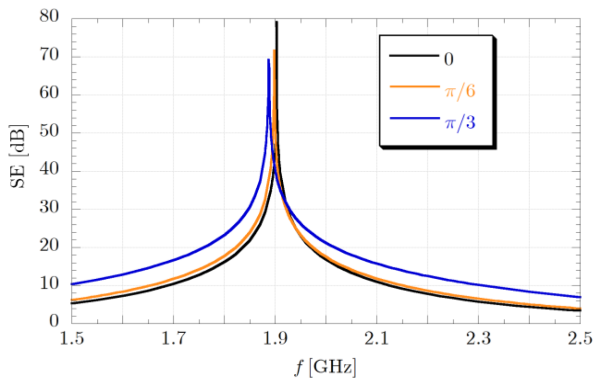

(a)

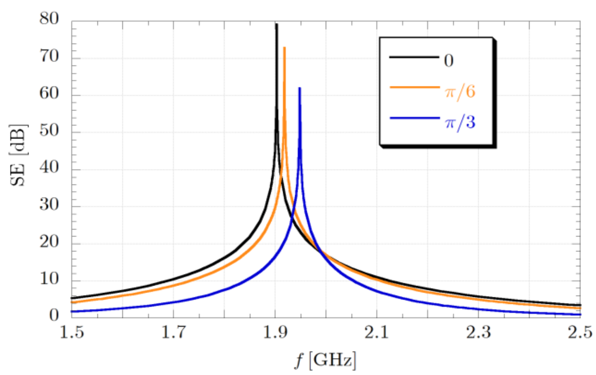

(b)

Fig. 3. SE of the metallic JC FSS in Fig. 2 as a function of frequency under: (a) TE and (b) TM plane-wave incidence for different incidence angles θ along the ϕ=0 plane.

It is then interesting to study how the SE changes by placing a dipole source at z_s closer and closer to the screen; thus, considering a real near-field source. This is illustrated in Fig. 4 at the operating frequency f_{res}=1.9 GHz. It can be seen that the SE for both horizontal and vertical dipoles of both electric and magnetic type can change by almost 20 dB with small variations of z_s (from 5 mm to 30 mm); whereas, for larger values of z_s, the horizontal dipole results converge to the normally-incident plane-wave SE (and the horizontal dipole; thus, gains the characteristics of a far-field source). This is consistent with the fact that a Horizontal Electric Dipole (HED) behaves in the far field as a TE plane wave, while a Horizontal Magnetic Dipole (HMD) as a TM plane wave; since source and observation points lie along the z axis, the associated TE and TM plane waves behave as normally incident TEM plane waves.

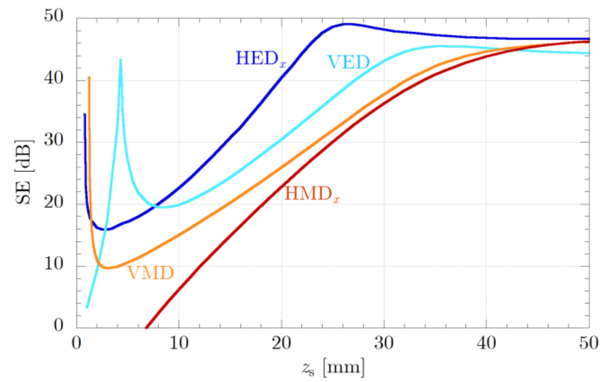

Fig. 4. SE of the JC FSS in Fig. 2 as a function of the dipole-screen distance z_s for different dipole types and orientations at the resonant frequency f_{res}=1.9 GHz for normal plane-wave incidence.

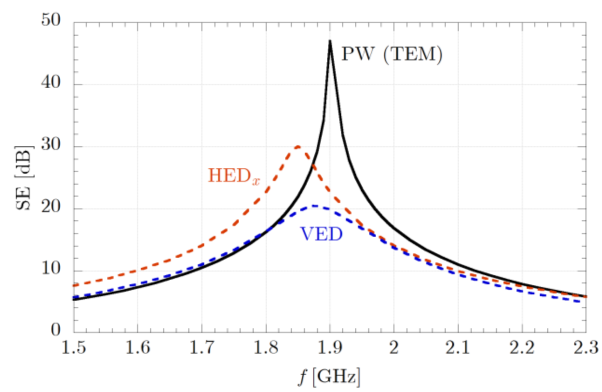

(a)

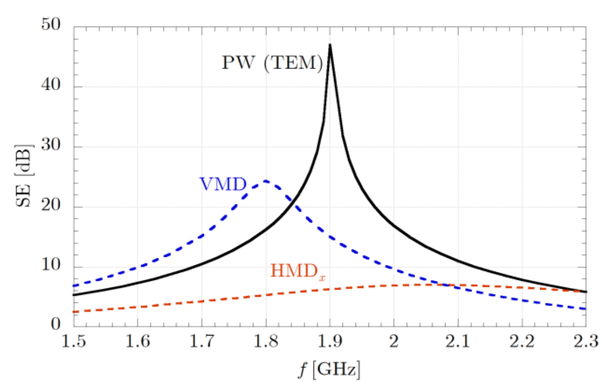

(b)

Fig. 5. SE of the JC FSS in Fig. 2 as a function of frequency for: (a) electric and (b) magnetic dipoles at the dipole-screen distance z_s=10 mm.

On the other hand, since vertical dipoles do not have a far field in their direction, it is not obvious that for large z_s their SE tends to a plane-wave SE; as it can be seen in Fig. 4, this actually occurs for the considered structure in the Vertical-Magnetic-Dipole (VMD) case, but not in the Vertical-Electric-Dipole (VED) case.

In general, for all the dipole sources the SE decreases by decreasing the dipole-screen distance z_s; however, for the VED, the SE presents a peak when the source is placed at a critical distance z_c very close to the screen at z_c=4.3 cm. Moreover, for z_s=0 the SE for the HED$_x$ and the VMD tends to infinity, while for the VED and the HMD$_x$ assumes a finite (low) value. Such a behavior can easily be understood taking into account that for z_s=0 the dipoles lie on the PEC part of the JC element, so that the HED x and VMD are short-circuited (and the relevant radiated field is zero), while the radiation of the VED and HMD$_x$ are maximized.

In order to understand how the frequency-selective behavior varies in the presence of a finite source close to the screen, in Fig. 5 the SE is presented as a function of frequency using a conventional TEM plane-wave source and both an electric and a magnetic dipole (Figs. 5 (a) and 5 (b), respectively) with different orientations and with the dipole source placed at z_s=10 mm.

It can be observed that both the resonant frequency, the relevant bandwidth and the SE peak value change significantly, depending on the dipole type and orientation. In particular, assuming that the dominant part of the electric-dipole spectrum is constituted by TE plane waves and that of the magnetic-dipole spectrum by TM plane waves, it can be understood why the SE of a VMD and of a HMD presents stronger differences with respect to the SE of a normally incident plane wave. It is worth noting that in the HMD case the resonant behavior has completely disappeared.

In Fig. 6, the SE of the DL for incident (a) TE and (b) TM plane waves is reported at θ=0, π/6, π/3 as a function of frequency along the ϕ=0 plane. Two resonances are present and the shielding performance is quite similar for both polarizations; in particular, while the first resonance at f_{res1}≃2 GHz is quite sensitive to the incident angle, the second resonance at f_{res2}=2.32 GHz is almost independent of the characteristics of the incident plane wave. Moreover, it is interesting to note that this type of screen is characterized by a frequency of total transmission f_{TT}=2.25 GHz (for which SE=0 db), which does not depend at all on the plane-wave properties.

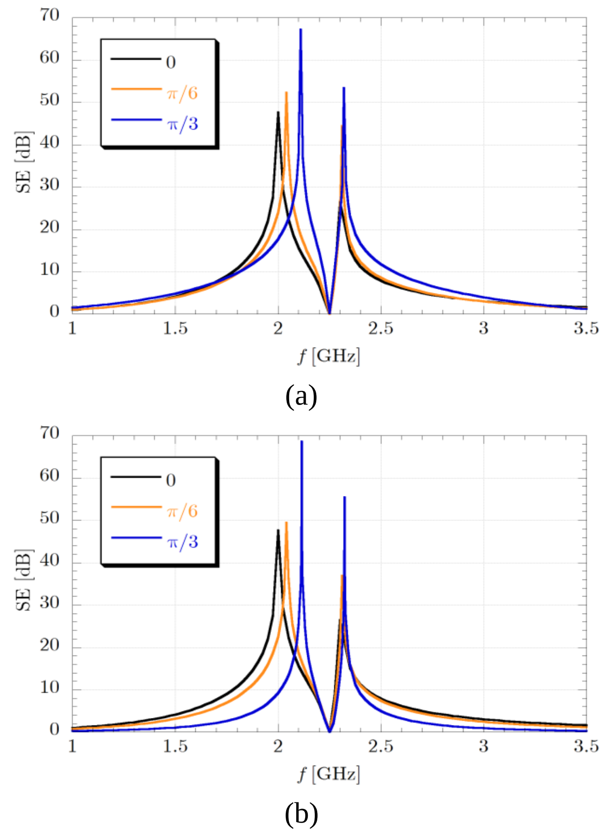

Fig. 6. SE of the DL FSS in Fig. 2 as a function of frequency under: (a) TE and (b) TM plane-wave incidence for different incidence angles θ along the ϕ=0 plane.

When a dipole source is considered, the operation is similar to that already illustrated for the JC screen, except for the fact that now the SE for the HED$_x$ and the VMD does not tend to infinity for source points approaching the screen plane, since in this case the source does not lie on a PEC part of the screen. This is shown in Fig. 7 at the operating frequency f_{res1}=2 GHz, where it can be seen that the SE monotonically decreases to low SE values by decreasing the dipole-screen distance z_s except for the VMD, which presents a SE peak at the critical distance z_c=3.3 cm and maintains a considerably large SE value also for very small z_s (always larger than 20 db); the latter is consistent with the well-known fact that a closed loop strongly interacts with an orthogonal magnetic dipole.

Finally, also for the DL FSS, the SE is presented as a function of frequency using a conventional TEM plane-wave source and both an electric and a magnetic dipole placed at z_s=10 mm (Figs. 8 (a) and 8 (b), respectively) with different orientations. It can be observed, that also for this structure, both the resonant frequencies and the SE peak values strongly depend on the dipole type and orientation. In particular, the resonant characteristics almost completely disappear when a VED or an HMD source is considered. Finally, it is interesting to note that in the presence of dipole sources, the total transmission phenomenon is still present at the frequency f_{TT}=2.25 GHz.

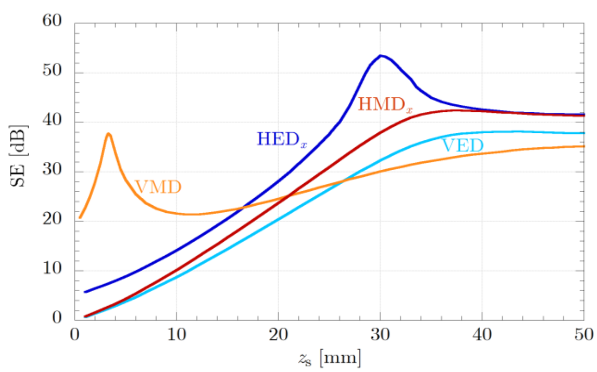

Fig. 7. SE of the DL FSS in Fig. 2 as a function of the dipole-screen distance z_s for different dipole types and orientations at the first resonant frequency f_{res1}=2 GHz for normal plane-wave incidence.

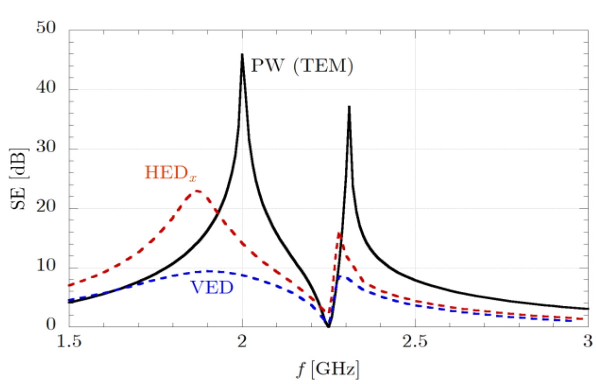

(a)

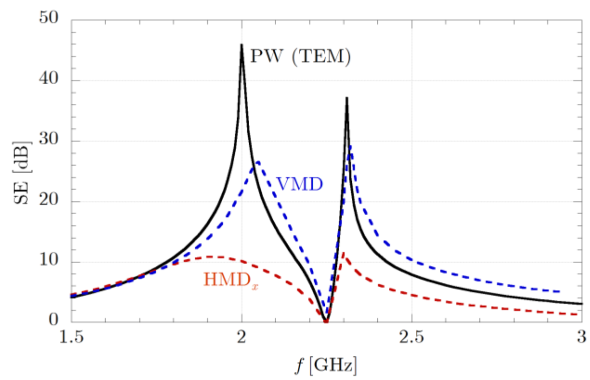

(b)

Fig. 8. SE of the DL FSS in Fig. 2 as a function of frequency for: (a) electric and (b) magnetic dipoles at the dipole-screen distance z_s=10 mm.

VI. CONCLUSION

The shielding characteristics of resonant frequency-selective periodic screens based on metallic FSSs in the presence of both plane-wave far-field and dipole near-field sources have been investigated. After an analysis based on a conventional plane-wave excitation, the interaction between the resonant screen and a finite near-field source placed in its proximity has been studied in detail, through a periodic MoM approach in conjunction with the Array Scanning Method. In particular, this analysis method allows for taking into account all the propagating and evanescent waves constituting the spectrum of the dipole source. It has been shown how the presence of finite sources can affect the resonant frequency and the relevant bandwidth of a frequency-selective screen; thus, calling for reliable numerical tools for the analysis and design and demonstrating how conclusions drawn on the basis of conventional PW excitation are not representative of the actual behavior of frequency selective shielding surfaces.

REFERENCES

[1] B. A. Munk, “Frequency selective surfaces: theory and design,” *New York: Wiley*, 2000.
[2] A. S. Barlevy and Y. Rahmat-Samii, “On the electrical and numerical properties of high q resonances in frequency selective surfaces,” *Progress In Electromagnetics Research*, vol. 22, pp. 1-27, 1999.
[3] G. Lovat, P. Burghignoli, and S. Celozzi, “Shielding properties of a wire-medium screen,”

IEEE Trans. Electromagn. Compat., vol. 50, no. 1, pp. 80-88, February 2008.

[4] R. Araneo, G. Lovat, and S. Celozzi, "Shielding effectiveness of periodic screens against finite high-impedance near-field sources," *IEEE Trans. Electromagn. Compat.*, vol. 53, no. 3, pp. 706-716, August 2011.

[5] J. van Tonder and U. Jakobus, "Infinite periodic boundary conditions in FEKO," *ACES Journal*, vol. 24, no. 6, pp. 584-591, 2009.

[6] B. Lin, S. Du, H. Zhang, and X. Ye, "Design and simulation of frequency-selective radome together with a monopole antenna," *ACES Journal*, vol. 25, no. 7, pp. 620-625, 2010.

[7] A. Yakovlev, C. Simovski, S. Tretyakov, and G. Hanson, "Accurate and rapid analysis of high impedance surfaces: plane-wave and surface-wave analytical models," *In ACES Conference Paper-Modeling Techniques for Periodic Structures and Metamaterial Applications-I*, 2010.

[8] J. Romeu and Y. Rahmat-Samii, "Fractal FSS: a novel dual-band frequency selective surface," *IEEE Trans. Antennas Propag*., vol. 48, no. 7, pp. 1097-1105, July 2000.

[9] S. Barbagallo, A. Monorchio, and G. Manara, "Small periodicity FSS screens with enhanced bandwidth performance," *Electronics Letters*, vol. 42, pp. 382-384, 2006.

[10] K. Sarabandi and N. Behdad, "A frequency selective surface with miniaturized elements," *IEEE Trans. Antennas Propag*., vol. 55, no. 5, pp. 1239-1245, May 2007.

[11] B. Sanz-Izquierdo, E. A. Parker, J. B. Roberson, and J. C. Batchelor, "Singly and dual polarized convoluted frequency selective structures," *IEEE Trans. Antennas Propag.*, vol. 58, no. 3, pp. 690-696, March 2010.

[12] A. M. Attiya, "Dyadic green's function of an elementary point source above a periodically-defected-grounded dielectric slab," *Progress In Electromagnetics Research B*, vol. 4, pp. 127-145, 2008.

[13] G. Lovat, "Near-field shielding effectiveness of 1-D periodic planar screens with 2-D near-field sources," *IEEE Trans. Electromagn. Compat.*, vol. 51, no. 3, pp. 708-719, August 2009.

[14] G. Lovat and P. Burghignoli, "Propagation and field excitation in metalstrip grating waveguides: homogeneous model and full-wave analysis," *IEEE Antennas Wireless Propag. Lett*., vol. 8, pp. 708-711, 2009.

[15] S. Paulotto, G. Lovat, P. Baccarelli, and P. Burghignoli, "Green's function calculation for a line source exciting a 2-D periodic printed structure," *IEEE Microw. Wireless Compon. Lett*., vol. 20, no. 4, pp. 181-183, April 2010.

[16] S. Paulotto, P. Baccarelli, P. Burghignoli, G. Lovat, G. Hanson, and A. Yakovlev, "Homogenized green's functions for an aperiodic line source over planar densely periodic artificial impedance surfaces," *IEEE Trans. Microw. Theory Tech*., vol. 58, no. 7, pp. 1807-1817, July 2010.

[17] G. Lovat, R. Araneo, and S. Celozzi, "Dipole excitation of periodic metallic structures," *IEEE Trans. Antennas Propag*., vol. 59, no. 6, pp. 2178-2189, June 2011.

[18] G. Lovat, R. Araneo, and S. Celozzi, "Planar and bulk resonant periodic screens against plane-wave and electric-dipole excitations," *In Proc. IEEE Electromagn. Compat. Symp.*, pp. 623-628, August 5-10, 2012.

[19] G. Valerio, P. Baccarelli, S. Paulotto, F. Frezza, and A. Galli, "Regularization of mixed-potential layered media greens functions for efficient interpolation procedures in planar periodic structures," *IEEE Trans. Antennas Propag.*, vol. 57, no. 1, pp. 122-134, January 2009.

[20] H. Bahadori, H. Alaeian, and R. Faraji-Dana, "Computation of periodic green's functions in layered media using complex images technique," *Progress In Electromagnetics Research*, vol. 112, pp. 225-240, 2011.

[21] G. Lovat, P. Burghignoli, and S. Celozzi, "A tunable ferroelectric antenna for fixed-frequency scanning applications," *IEEE Antennas Wireless Propag. Lett.*, vol. 5, pp. 353-356, 2006.

[22] R. Araneo, G. Lovat, S. Celozzi, and M. D'Amore, "Shielding performance of nanostructured transparent thin films loading apertures of metallic enclosures excited by dipole sources," *In Proc. IEEE Electromagn. Compat. Symp*., pp. 214-219, August 14-19, 2011.

[23] A. F. Peterson, S. L. Ray, and R. Mittra, "Computational methods for electromagnetics," *Piscataway, NJ: IEEE Press*, 1998.

[24] I. Stevanovic, P. Crespo-Valerio, K. Blagovi´c, F. Bongard, and J. R. Mosig, "Integral-equation analysis of 3-D metallic objects arranged in 2-D lattices using the ewald transformation," *IEEE Trans. Microw. Theory Tech*., vol. 54, no. 10, pp. 3688-3697, October 2006.

[25] J. Su, X. W. Xu, M. He, and K. Zhang, "Integral equation analysis of frequency selective surfaces using ewald transformation and lattice symmetry," *Progress In Electromagnetics Research*, vol. 121, pp. 249-269, 2011.

[26] S. Oroskar, D. R. Jackson, and D. R. Wilton, "Efficient computation of the 2D periodic green's function using the ewald method," *J. Comput. Phys.*, vol. 219, pp. 899-911, September 2006.

[27] F. Capolino, D. Wilton, and W. Johnson, "Efficient computation of the 3D green's function for the

helmholtz operator for a linear array of point sources using the ewald method," *J. Comput. Phys.*, vol. 223, no. 1, pp. 250-261, 2007.
[28] G. Lovat, P. Burghignoli, and R.Araneo, "Efficient evaluation of the three-dimensional periodic green's function through the ewald method," *IEEE Trans. Microw. Theory Tech.*, vol. 56, no. 9, pp. 2069-2075, 2008.
[29] K. R. Aberegg, A. Taguchi, and A. F. Peterson, "Application of higher-order vector basis functions to surface integral equation formulations," *Radio Sci.*, vol. 31, pp. 1207-1213, September 1996.
[30] R. Araneo and G. Lovat, "Analysis of the shielding effectiveness of metallic enclosures excited by internal sources through an efficient method of moment approach," *ACES Journal*, vol. 25, no. 7, pp. 600-611, July 2010.
[31] R. D. Graglia, "On the numerical integration of the linear shape functions times the 3-D green's function or its gradient on a plane triangle," *IEEE Trans. Antennas Propag.*, vol. 41, no. 10, pp. 1448-1455, October 1993.
[32] D. A. Dunavant, "High degree efficient symmetrical gaussian quadrature rules for the triangle," *Intern. J. Num. Meth. Engin.*, vol. 21, pp. 1129-1148, June 1985.

Giampiero Lovat received his Laurea degree (*cum laude*) in Electronic Engineering and his Ph.D. degree in Applied Electromagnetics from Sapienza University of Rome, Rome, in 2001 and 2005. From January 2004 to July 2004 he was a Visiting Scholar at the University of Houston, Houston, TX. In 2005, he joined the Department of Electrical Engineering, Sapienza University of Rome, where he is currently an Assistant Professor. His current research interests include electrodynamics of graphene and carbon nanotubes, energy harvesting by means of piezoelectric nanowires, leaky waves, periodic structures, artificial materials and electromagnetic shielding.

Rodolfo Araneo received his M.S. (cum laude) and Ph.D. degrees in Electrical Engineering from the University of Rome "La Sapienza", Rome, in 1999 and 2002. His research activity is mainly in the field of EMC and includes numerical and analytical techniques for modeling high-speed printed circuit boards, shielding, and transmission line analysis. He has authored more than 110 papers in international journals and conference proceedings.

Salvatore Celozzi is Full Professor of Electrical Engineering with the Department of Astronautical, Electrical and Energetic Engineering at the University of Rome "La Sapienza." Celozzi has published more than 120 papers in international journals or conference proceedings, mainly in the fields of electromagnetic shielding and transmission lines. He served as Associate Editor of the IEEE Electromagnetic Compatibility (1995-2000) and authored a book on Electromagnetic Shielding for Wiley in 2008. His current research interests include transmission lines, electromagnetic compatibility, meta and piezo-materials and numerical methods in electromagnetics.

Physical Optics Analysis for RCS Computation of a Relatively Small Complex Structure

Amin B. Gorji [1], Bijan Zakeri [1], and Reza C. Janalizadeh [2]

[1] Faculty of Electrical and Computer Engineering
Babol Noshirvani University of Technology, Babol, Iran
amin.gorji@stu.nit.ac.ir, zakeri@nit.ac.ir

[2] School of Electrical and Computer Engineering
University of Tehran, Tehran, Iran
r.janalizadeh@ut.ac.ir

Abstract **─** High-frequency methods are well known as a convenient approach for treating Electromagnetic (EM) problems regarding electrically large structures. In this paper however, this method is proposed as a proper tool for computing the mono-static Radar Cross Section (RCS) of a relatively small complex structure. This claim has been verified via simulation through a frequency range of 100 MHz to 10 GHz and measurement for the structure of this work. In this regard, initially, RCS computation via the Method of Moments (MoM) has been executed. As this method leads to rigorous and time consuming computations, Physical Optics (PO) has been utilized for the same purpose. These computations have been carried out by employing the Integral Equation (IE) and asymptotic solver of CST Microwave Studio (MWS). PO proves to be time-efficient compared to MoM. Graphs comparing PO and MoM-computed RCS are illustrated. In addition, the similarity of the results obtained by PO and MoM has been thoroughly discussed. Correlation between these results has been observed. Also, mean and standard deviation values for PO RCS-error have been provided for the entire simulation frequency. As dimension to wavelength ratio (D/λ) of the structure increases, the convergence of these two methods for RCS computation becomes satisfactory. Finally, measurement has been accomplished at frequency of 8.5 GHz to validate PO computations.

Index Terms **─** Complex structure, Integral Equation (IE), Method of Moments (MoM), Physical Optics (PO) and Radar Cross Section (RCS).

I. INTRODUCTION

Target detection has been of great interest in both civilian and military applications [1]-[17]; e.g., through wall imaging during rescue operations in disastrous areas, identification of objects buried under rough surface, ships floating over the sea surface and targets inside vegetation. Characterization of Electromagnetic (EM) wave propagation and scattering from targets provides data for Radar Cross Section (RCS) prediction and Synthetic Aperture Radar (SAR) image construction of corresponding targets [18]-[20].

RCS computation and scattering analysis of electrically large targets located in natural environment via the Method of Moments (MoM), have been under study for many years. However, complexities due to large target size and multi-interactions between the target and surrounding media, make the simulation process much more rigorous; especially in high frequencies. However, high frequency methods such as Geometrical Optics (GO), Physical Optics (PO), Geometrical Theory of Diffraction (GTD), Physical Theory of Diffraction (PTD), Shooting and Bouncing Rays (SBR), etc., have been applied to the EM scattering of these structures with good accuracy and convincing physical insight [21]-[25]. Meanwhile, the RCS of electrically small simple targets located above rough surfaces has been computed accurately

Submitted On: February 2, 2013
Accepted On: July 25, 2014

via GO, PO and Iterative Physical Optics (IPO) [26]-[27].

A complex structure consists of several reflectors within a radar resolution cell. According to this definition, almost all real world maritime targets are complex structures. For such targets, there is no analytical relationship between the target's surface and its RCS.

In this paper, the RCS of a relatively small *complex* structure have been computed via PO and MoM. Then the similarity of RCS results have been assessed. A minimum dimension to wavelength ratio (D/λ), resulting in precise RCS computation by means of PO, is then obtained. The rest of the paper is organized as follows: In section II, a relatively small model of a vessel has been introduced as the complex structure. The geometry of the problem and simulation frequency range is included in this section. In section III, the methods by which RCS computation has been performed are introduced. The IE and asymptotic solver of the commercial software CST Microwave Studio (MWS) have been employed for this purpose. Resulted RCS plots, error tables and correlation graphs for three view angles: azimuth, elevation along the length and elevation along the width are provided and analyzed through the frequency range of 100 MHz to 10 GHz in section IV. A minimum D/λ for an accurate RCS computation by means of PO is investigated in this section. Finally, in section V, measurement has been accomplished at 8.5 GHz for azimuth view in order to validate PO for the RCS computation of the vessel.

II. STRUCTURE PROFILE & SIMULATION SETUP

A. Model description

The complex structure selected for RCS computation is the scaled model of a typical vessel depicted in Fig. 1. Also, Table 1 provides dimensions for the same structure.

B. Geometry of the problem

The simulation has been performed for three different view aspects: azimuth, elevation along the length of the vessel and elevation along the width of the vessel. As depicted in Fig. 1 (a), azimuth view aspect is demonstrated by sweeping φ from 0 to 2π, elevation along the length view is acquired while sweeping θ from 0 to π, as shown in Fig. 1 (b) and elevation along the width view is attained while sweeping θ from 0 to π, as in Fig. 1 (c); in which θ and φ are elevation and azimuth angles, respectively.

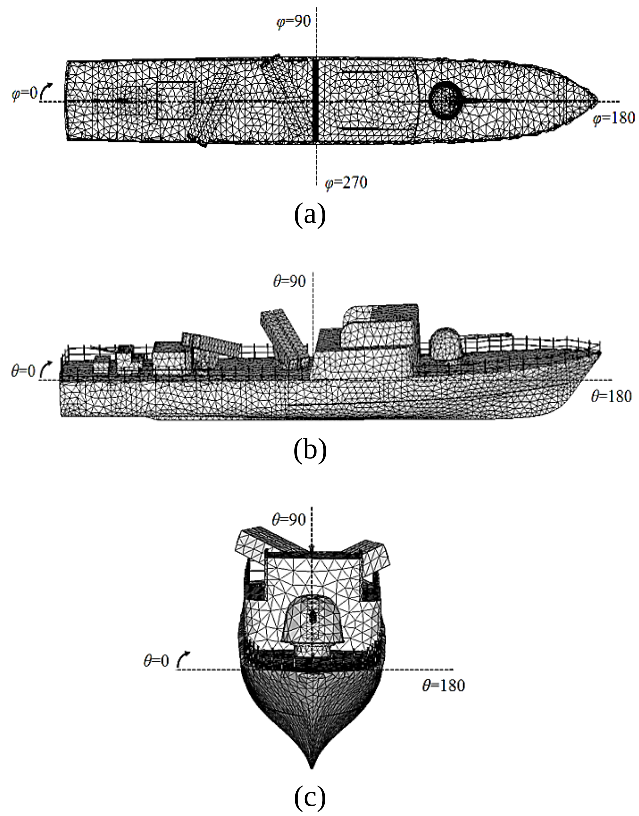

Fig. 1. View aspects for the meshed vessel: (a) azimuth, (b) elevation along the length and (c) elevation along the width.

Table 1: Dimensions of the structure

Width	Length	Height
8.25 cm	58.75 cm	6.27 cm

C. Frequency range

PO approximation gives convenient and simple expressions for the scattering cross section and therefore is widely used. This approximation contains wavelength dependence and the results are often in good agreement with experimental data, even though it is difficult to establish exactly how valid PO is for a general case [28].

Previous numerical studies using MoM and FDTD have given broad assessments of the reliability of PO. For instance, the validity and accuracy study of PO method for the reduced-size lens antennas and rough surface scattering models [26]-[27], [29]. In the former study, it has been shown that PO can be used for analyzing lens antennas typically larger than 5λ, where λ is the wavelength. In [27], quite acceptable results have been shown using GO and PO for the RCS prediction of a PEC target with dimensions 4λ/3×2λ/3×λ above a Gaussian random rough surface, with Z_s=Z_0 (0.2+j0.02), rms height of 5 cm and correlation length of 40 cm at 2 GHz frequency. Also, the RCS of an object with surface impedance Z_s=Z_0 (0.2+j0.02) and dimensions less than 8λ and more than 1.5λ has been precisely computed in the same frequency in the same work.

In this work, the central simulation frequency is chosen in a manner which the corresponding minimum D/λ determined by the height (smallest dimension) of the structure is identical to the lower limits of D/λ (approximately 1) in works mentioned previously [26], [27]. In this case, RCS precision is analyzed in the vicinity of a frequency, which PO RCS computation of prototype objects is performed with an adequate accuracy.

III. METHODS OF ANALYSIS

A. Physical optics

It is common practice in the analysis of EM boundary-value problems to use auxiliary vector potentials $\vec{A}$ and $\vec{F}$ as aids in obtaining solutions for the electric $\vec{E}$ and magnetic $\vec{H}$ fields. The vector potentials are given by:

$$\vec{A} = \frac{\mu_0}{4\pi}\int_V \vec{J}(\vec{r}')\frac{e^{-jk|\vec{r}-\vec{r}'|}}{|\vec{r}-\vec{r}'|}dv', \tag{1}$$

and

$$\vec{F} = \frac{\varepsilon_0}{4\pi}\int_V \vec{M}(\vec{r}')\frac{e^{-jk|\vec{r}-\vec{r}'|}}{|\vec{r}-\vec{r}'|}dv', \tag{2}$$

where $\vec{J}$ and $\vec{M}$ are electric and magnetic current sources, respectively and k is the wavenumber.

PO is a method for approximating high frequency surface currents. If the object is large compared to a wavelength and the surface is smooth (radius of curvature is much greater than a wavelength), $\vec{J}$ may be well approximated by the current that would exist if the surface were a conducting plane tangential to the surface at the point $\vec{r}'$. In this case $\vec{J}_s = 2\hat{n}\times\vec{H}^i$ in the region illuminated by the incident field, while $\vec{M}_s = 0$. Subscript s demonstrates the surface nature of the current source and $\hat{n}$ is the unit vector normal to the surface. The $\hat{i}\cdot\hat{n}<0$ holds for the region illuminated by the incident field, where $\hat{i}$ is a unit vector in the direction of incidence. Assuming $(\nabla\cdot\vec{A})=0$, the EM fields are:

$$\vec{E} = -j\omega\vec{A}, \tag{3}$$

and

$$\vec{H} = \frac{1}{\mu_0}\nabla\times\vec{A}. \tag{4}$$

Suppose the structure depicted in Fig. 1 is illuminated by an incident plane wave as:

$$\vec{E}^i(\vec{r}) = E^i e^{-jk(\hat{i}.\vec{r})}\hat{e}^i. \tag{5}$$

The surface current will be:

$$\vec{J}_s(\vec{r}') = \frac{2}{\eta_0}E^i e^{-jk(\hat{i}.\vec{r}')}\hat{n}\times(\hat{i}\times\hat{e}^i), \tag{6}$$

where

$$\vec{H}^i = \frac{1}{\eta_0}(\hat{i}\times\vec{E}^i), \tag{7}$$

has been used for the relation between the incident plane wave magnetic and electric fields and η_0=120π ohm is the free space characteristic impedance. The far-field magnetic vector potential is well known as:

$$\vec{A}_{ff} = \frac{\mu_0}{4\pi}\frac{e^{-jk|\vec{r}|}}{|\vec{r}|}\int_V \vec{J}(\vec{r}')e^{jk(\vec{r}'\cdot\hat{r})}dv'. \tag{8}$$

Therefore, the far-field scattered electric field will be:

$$\vec{E}^s_{ff} = -jk\frac{e^{-jk|\vec{r}|}}{2\pi|\vec{r}|}E^i \int_S \left(\hat{i}(\hat{n}\cdot\hat{e}^i) - \hat{e}^i(\hat{n}\cdot\hat{i})\right)e^{-j2k(\hat{i}\cdot\vec{r}')}ds', \tag{9}$$

where the BAC-CAB identity has been used for the cross product $\hat{n}\times(\hat{i}\times\hat{e}^i)$. As is usually the case, the antenna receives the component of the scattered wave along the direction of the polarization of the incident wave $\hat{e}^i$. Thus, the far-filed scattered electric field received by the antenna will be:

$$\begin{aligned}\vec{E}^s_r &= (\vec{E}^s_{ff}\cdot\hat{e}^i)\hat{e}^i \\ &= jk\frac{e^{-jk|\vec{r}|}}{2\pi|\vec{r}|}E^i\int_S(\hat{n}\cdot\hat{i})e^{-j2k(\hat{i}\cdot\vec{r}')}ds'\hat{e}^i.\end{aligned} \tag{10}$$

Regarding the definition of RCS as:

$$\sigma = \lim_{|\vec{r}|\to\infty} 4\pi |\vec{r}|^2 \frac{\left|\vec{E}_r^s\right|^2}{\left|\vec{E}^i\right|^2} , \qquad (11)$$

we get:

$$\sigma = \frac{k^2}{\pi} \left| \int_S (\hat{n}\cdot\hat{i}) e^{-j2k(\hat{i}\cdot\vec{r}')} ds' \right|^2 , \qquad (12)$$

for the scattering cross section of a conducting body. While robust, PO does not account for the fields diffracted by edges or those from multiple reflections, so supplemental corrections are usually added to it. The PO method is used extensively in high-frequency reflector antenna analysis, as well as radar cross section prediction [30], [31].

The asymptotic solver of CST MWS is based on the SBR method and accounts for the multiple scattering effect [32]. It computes PO scattered fields too. As the effect of the sea rough surface and the vessel structure itself on multiple scattering has been neglected, only RCS calculations via PO have been done.

The SBR method was developed to predict the multiple-bounce backscatter from complex objects. It uses the ray optics model to determine the path and amplitude of a ray bundle, but uses a PO based scheme that integrates surface currents deposited by the ray at each bounce point. The SBR method is used in RCS prediction of cavities [25] and image formation of targets [33]. Also, it is used to predict wave propagation and scattering in complex urban environments to determine the coverage for cellular telephone service [34].

B. Method of moments

CST MWS incorporates an integral equation solver [32]. This solver employs a MoM discretization with a surface integral formulation of the electric and magnetic field. In other words, the discretization of the calculation area is reduced to the object boundaries; thus, leading to a linear equation system with fewer unknowns than volume methods. In order to reduce the numerical complexity, a Multilevel Fast Multipole Method (MLFMM) approach has been used.

IV. RESULTS AND DISCUSSION

RCS computation and scattering analysis of electrically large targets via MoM, possesses complexities which result in rigorous simulation processes; especially in high frequencies. This issue has also been confronted during the RCS computation of the vessel. PO has been employed in order to solve this complication.

Referring to [26], [27], it is seen that PO provides precise results for the RCS of simple objects with a minimum D/λ of 1. During this work, the same D/λ has been chosen to assess the accuracy of PO RCS computations. As for the vessel, this minimum has been used to acquire the central value of the simulation frequency. As in a constant frequency, the height of the vessel results in the minimum D/λ, a value of 1 for this parameter is analogous to a simulation frequency of 5 GHz. However, in order to thoroughly analyze the reliability of PO, a symmetric 10 GHz frequency range has been set providing results for D/λs' much less than those cited in [26], [27].

Graphs comparing PO and MoM RCS are provided in Fig. 2. From Fig. 2, it is evident that as frequency increases, results from PO converge satisfyingly to results of MoM for most of the observation range. As stated previously, PO does not account for the fields diffracted by edges. Considering azimuth graphs in Fig. 2, especially in 600 MHz, it is seen that PO RCS deviates dramatically from MoM results for observation angels corresponding to the front and tail of the vessel. This is due to the fact that the excitation wave is incident on edges located in these positions. Obviously, this error is negligible in high frequencies. This error consumption rises from the fact that the dimensions of the structure are increasing electrically and partitions of the structure approach PO approximation validity region. Therefore, PO requirements are partially fulfilled.

Recalling the fact that PO approximation is valid only for a large target with a smooth surface, it is seen that the convergence in azimuth graphs reaches to a maximum for side views ($\varphi = \pi/2$ and $3\pi/2$). This is due to the fact that the excitation field is mainly incident upon the side walls of the vessel, which can be interpreted as infinite planes in higher frequencies. Also, as seen in Fig. 2, the complexity of RCS rises as frequency increases due to the increase in the resolution of the transceiver.

Tables 2-4 provide the mean and standard deviation of RCS error, devoting a chance of quantitative assessment of PO functionality. In addition, the dimensions of the vessel in terms of the simulation wavelength and the RCS average value have been shown. As seen in Table 2, the RCS average is approximately 5 dBsm more than RCS error for a minimum D/λ of 1. Considering the azimuth view, the main contribution to RCS is due to the vessel sidewalls, which results in precise PO RCS due to its large dimensions. Therefore, explaining the low error average. Also, for elevation along the width view, the difference between RCS average and RCS error is distinguishable. In this case PO rays are incident upon the central section of the structure, which its cross range is mainly a smooth PEC surface. Therefore, RCS is precisely computed for this view too. This can be also inferred from graphs of Fig. 2 in high frequencies. For elevation along the length however, the error is considerable compared to the RCS average itself. While MoM accounts for the effect of the scatterers set on the infrastructure of the vessel, PO requirements are not met because these scatterers are generally small compared to the wavelength; and although several reflectors are mounted on the main structure, they are not detected by the transceiver resolution cell during PO simulation. This effect is crystal clear in Fig. 2 for 1, 3 and 5 GHz, where the objects on the vessel contribute to MoM backscattered fields, which results in higher RCS values compared to PO backscattering, which possesses low RCS for central values of θ.

In order to grasp a deeper knowledge about the error values in the range of PO reliability, we will consider the data provided in Table 2 for the central frequency (5 GHz). Assume the vessel is an object with an isotropic RCS pattern with RCS average value. This object has an RCS value of 0.04 square-meters and an RCS toleration value of 0.008 square-meters. Therefore, it is concluded that the detected cross section may oscillate between 0.032 and 0.048 square-meters, which implies the fact that this amount of error may not cause complications from a target detection standpoint. The standard deviation in this region however, occupies a considerable interval, which means the error values are quite extensive in range. In other words, while RCS error is high for specific observations, it is negligible in other view angels in each single frequency.

Although, mean and standard deviation are the main parameters used for analyzing the distribution of a variable, in order to better analyze PO and MoM datasets, the Pearson Product-Moment Correlation Coefficient (PPMCC) defined in equation (13) has been used:

$$r = \frac{\sum_m \sum_n (A_{mn} - \overline{A})(B_{mn} - \overline{B})}{\sqrt{(\sum_m \sum_n (A_{mn} - \overline{A})^2)(\sum_m \sum_n (A_{mn} - \overline{A})^2)}} . \quad (13)$$

This criterion is a measure of the linear correlation between two variables A and B, where $\overline{A}$ and $\overline{B}$ are their mean values, respectively. r is limited to [-1,1], where 1 implies total positive correlation, 0 implies no correlation and -1 represents total negative correlation.

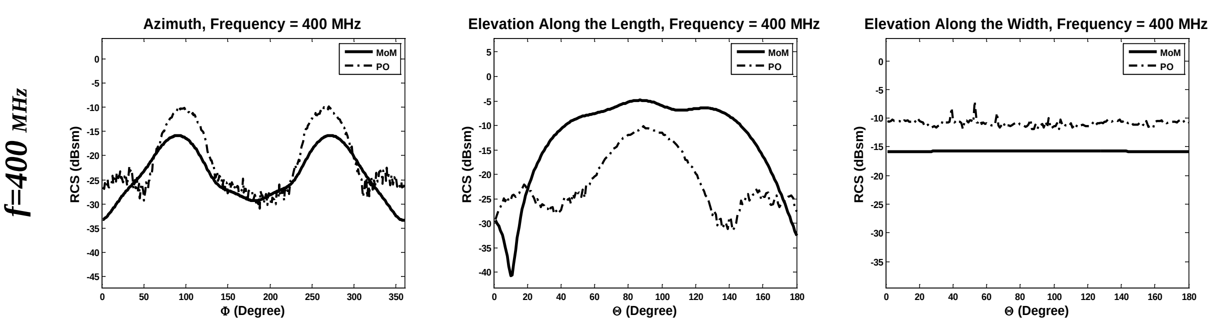

Fig. 2. Comparison of RCS obtained by MoM and PO (dashed marker). Columns represent view aspects azimuth, elevation along the length and elevation along the width.

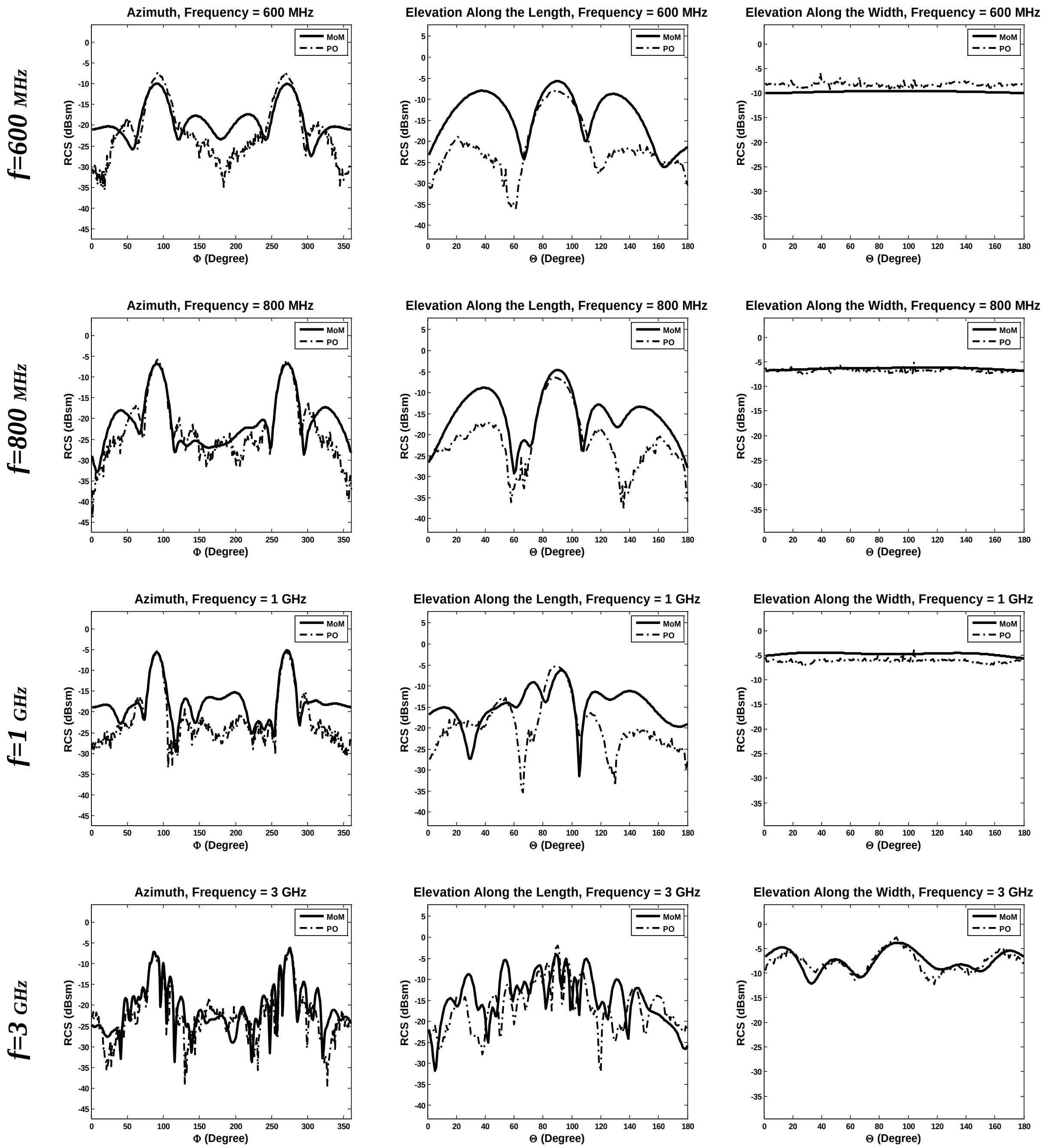

Fig. 2-continued. Comparison of RCS obtained by MoM and PO (dashed marker). Columns represent view aspects azimuth, elevation along the length and elevation along the width. Rows represent each simulation frequency.

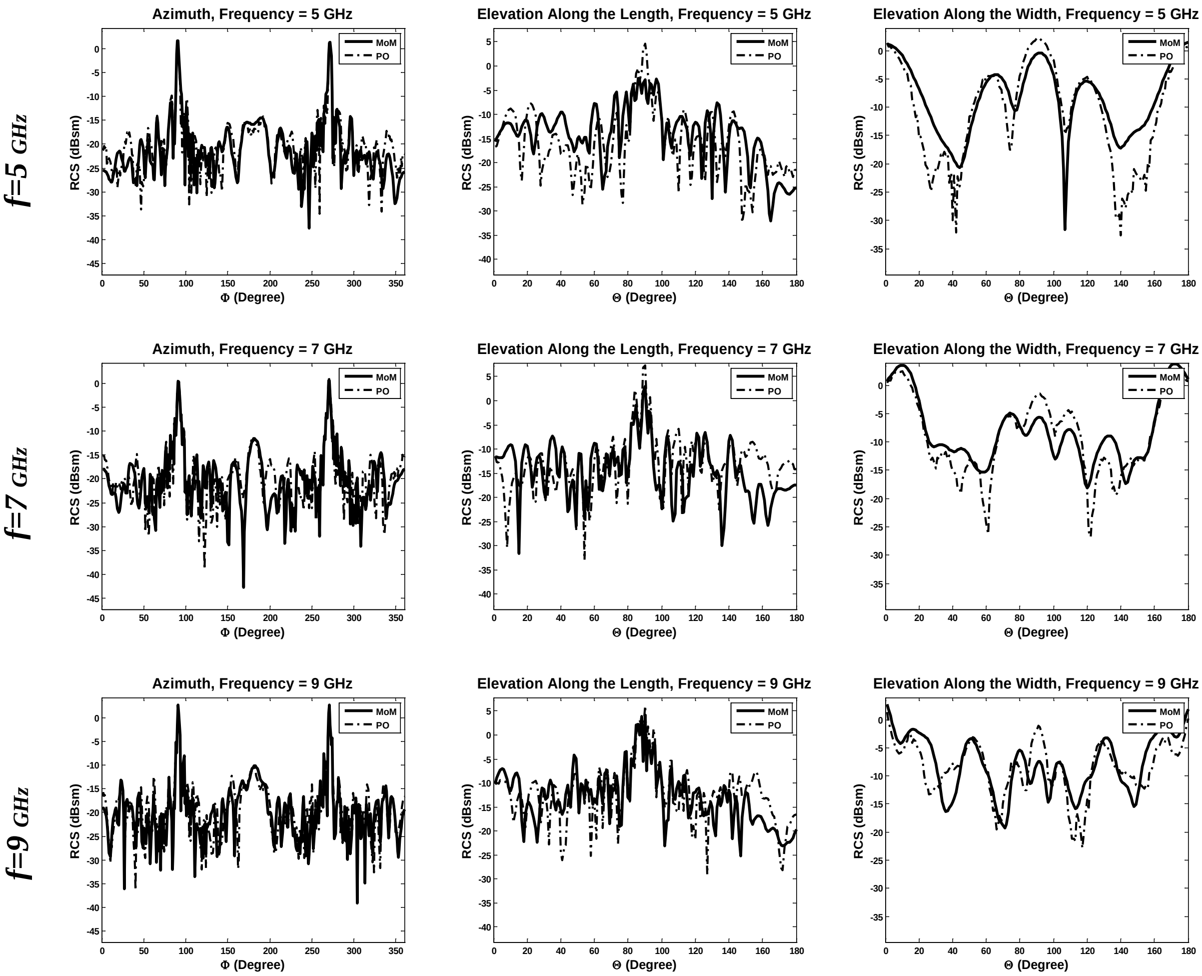

Fig. 2-continued. Comparison of RCS obtained by MoM and PO (dashed marker). Columns represent view aspects azimuth, elevation along the length and elevation along the width. Rows represent each simulation frequency.

Table 2: Error table for azimuth view

Frequency (GHz)	0.4	0.6	0.8	1	3	5	7	9
Length/λ	0.78	1.17	1.56	1.95	5.87	9.79	13.7	17.62
Width/λ	0.11	0.16	0.22	0.27	0.82	1.37	1.92	2.47
Height/λ	0.08	0.12	0.16	0.2	0.62	1.04	1.46	1.88
RCS Avg. (dBsm)	-21.07	-16.62	-15.46	-14.35	-16.65	-14.27	-14.55	-13.74
Error Avg. (dBsm)	-18.4	-18.98	-21.68	-19.4	-22.16	-20.79	-19.49	-18.02
Error Std. (dBsm)	-16.56	-18.16	-21.02	-20.21	-21.16	-17.52	-16.66	-12.96

Table 3: Error table for elevation along the length view

Frequency (GHz)	0.4	0.6	0.8	1	3	5	7	9
Length/λ	0.78	1.17	1.56	1.95	5.87	9.79	13.7	17.62
Width/λ	0.11	0.16	0.22	0.27	0.82	1.37	1.92	2.47
Height/λ	0.08	0.12	0.16	0.2	0.62	1.04	1.46	1.88
RCS Avg. (dBsm)	-8.65	-11.06	-12.08	-12.97	-11.51	-10.81	-10.46	-8.64
Error Avg. (dBsm)	-9.26	-12.57	-14.6	-14.74	-13.06	-10.64	-10.01	-10.74
Error Std. (dBsm)	-10.55	-13	-14.52	-14.75	-12.17	-5.9	-4.27	-7.52

Table 4: Error table for elevation along the width view

Frequency (GHz)	0.4	0.6	0.8	1	3	5	7	9
Length/λ	0.78	1.17	1.56	1.95	5.87	9.79	13.7	17.62
Width/λ	0.11	0.16	0.22	0.27	0.82	1.37	1.92	2.47
Height/λ	0.08	0.12	0.16	0.2	0.62	1.04	1.46	1.88
RCS Avg. (dBsm)	-15.76	-9.73	-6.37	-4.73	-6.97	-5.01	-3.51	-5.33
Error Avg. (dBsm)	-12.49	-13.58	-16.74	-10.26	-13.79	-8.690	-8.260	-8.29
Error Std. (dBsm)	-18.85	-17.76	-18.16	-15.71	-15.03	-7.79	-7.03	-8.37

The PPMCC computed for MoM and PO RCS has been plotted in Fig. 3. High values of *r* imply the fact that let alone the error, PO RCS has followed the pattern and complexities of precise MoM results. For instance, in Fig. 3 (a), correlation values are close to its maximum. As depicted in Fig. 2 for azimuth view, PO results represent the main features of RCS computed by MoM. Applying the same analysis to Fig. 3 (b), the minimum of correlation occurs in the vicinity of 4 GHz. Analyzing this based on graphs provided in Fig. 2, it is seen that this interpretation is in good agreement with RCS plots for 1, 3 and 5 GHz, explained previously via error tables. As for elevation along the width view, it is inferred from Fig. 3 (c) that the correlation coefficient is generally less than the azimuth case. Still, high correlateion is seen for most of the bandwidth. The same result is concluded from Fig. 2, where PO RCS follows the main aspects of MoM RCS.

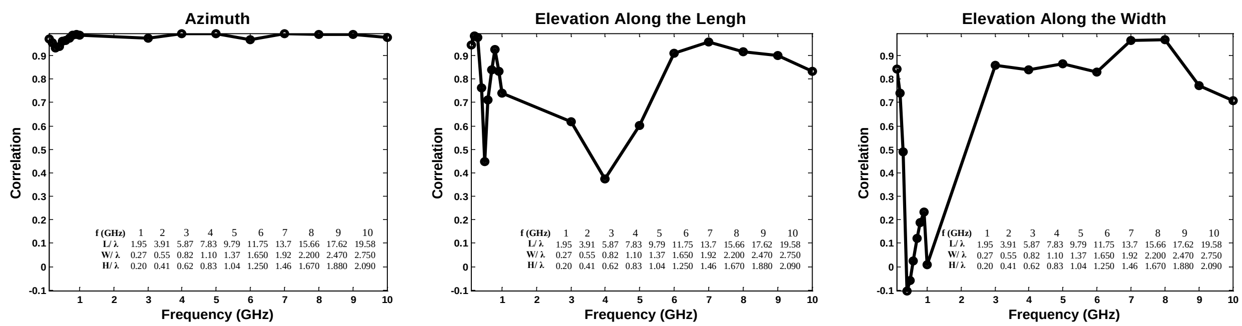

(a) (b) (c)

Fig. 3. Correlation graphs between MoM and PO for: (a) azimuth, (b) elevation along the length and (c) elevation along the width. D/λ value regarding each frequency are also provided in the tables.

V. RCS MEASUREMNET

In previous sections, it has been concluded that PO is an expedient replacement for MoM. Confirmation of results provided by PO via measurement will be the final validation for this analysis. Figure 4 shows the designed complex structure in a tapered anechoic chamber located on a pylon of 1 m height. A Continuous Wave (CW) measurement scenario has been carried out, employing the X band standard horn antenna with vertical polarization. RCS measurement has been accomplished at 8.5 GHz for azimuth view in 438 points. The structure is in the far-field of the transceiver with 3 m distance.

Comparison of measurement data with MoM and PO RCS is presented in Figs. 5 and 6, respectively. Also, the average of measured RCS along with the mean and standard deviation of MoM and PO computed RCS are provided in Tables 5-6. As seen in these tables, the average error is close to the RCS mean value itself. However, it should be noted that although the error mean and standard deviation are from the same order of the RCS average, considering the dimensions of the vessel, this error is not misleading as long as detection purposes are of concern. Also, it is seen that measured RCS values are in partial agreement with data provided in Table 2.

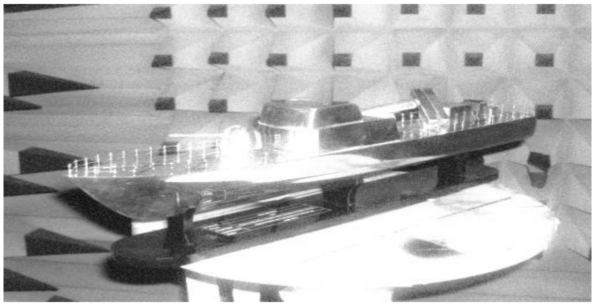

Fig. 4. Designed vessel in anechoic chamber.

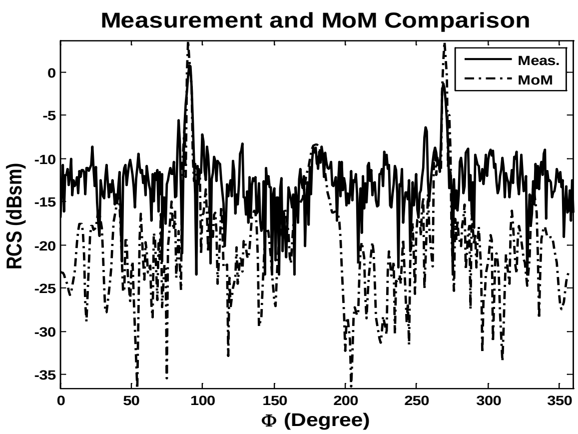

Fig. 5. Comparison of measured and MoM-computed RCS at 8.5 GHz.

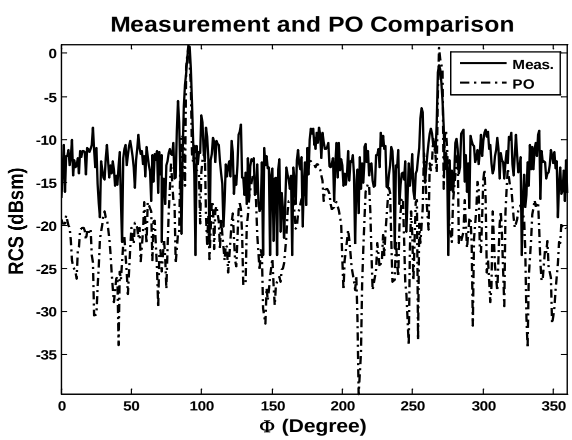

Fig. 6. Comparison of measured and PO-computed RCS at 8.5 GHz.

Table 5: Comparison of measured and MoM-computed RCS

RCS Avg. (dBsm)	Error Avg. (dBsm)	Error Std. (dBsm)
-11.13	-11.99	-8.79

Table 6: Comparison of measured and PO-computed RCS

RCS Avg. (dBsm)	Error Avg. (dBsm)	Error Std. (dBsm)
-11.13	-12.66	-12.38

VI. CONCLUSION

Due to complexities of MoM, PO has been used for RCS prediction of the vessel studied through this paper. On account of this, it has been demonstrated that PO results are invaluable tolerating the cost of temporal erroneous outcomes. Although as defined, PO best suits for EM problems of electrically large structures, it has shown credible for large values of D\λ during this work. Convergence of results obtained by PO and MoM are acceptable as the minimum D\λ exceeds 1. Although, error values may seem in considerable comparison with the structures' RCS itself, it should be noted that the impact of this error from target detection standpoint is negligible as the RCS of the structure is not considerable itself. On the other hand, it should be bolded that while the dimensions of complex structures increase, they actually meet PO approximation for high frequency analysis; which consequently results in RCS error reduction.

Error tables provided in this work can serve as a benchmark for quality assessment of future studies involving the development of enhanced high-frequency methods. Studies on the reliability of RCS prediction of maritime targets can be continued, while accounting for the effect of multiple scattering caused by the sea rough surface.

REFERENCES

[1] R. Firoozabadi, E. L. Miller, C. M. Rappaport, and A. W. Morgenthaler, “Subsurface sensing of buried objects under a randomly rough surface using scattered electromagnetic field data,” *IEEE Trans. Geosci. Remote Sens.*, vol. 45, no. 1, pp. 104-117, January 2007.

[2] G. Wang, Y. Zhang, and M. Amin, “New approach for target locations in the presence of wall ambiguities,” *IEEE Trans. Aerosp. Electron. Syst.*, vol. 42, no. 1, pp. 301-315, January 2006.

[3] Y. S. Yoon and M. G. Amin, “High-resolution through-the-wall radar imaging using beamspace MUSIC,” *IEEE Trans. Antennas Propag.*, vol. 56, no. 6, pp. 1763-1774, June 2008.

[4] P. C. Chang, R. J. Burkholder, J. L. Volakis, R. J. Marhefka, and Y. Bayram, “High-frequency EM

characterization of through-wall building imaging," *IEEE Trans. Geosci. Remote Sens.*, vol. 47, no. 5, pp. 1375-1387, May 2009.

[5] T. K. Chan, Y. Kuga, and A. Ishimaru, "Experimental studies on circular SAR imaging in clutter using angular correlation function technique," *IEEE Trans. Geosci. Remote Sens.*, vol. 37, no. 5, pp. 2192-2197, September 1999.

[6] S. Kidera, T. Sakamoto, and T. Sato, "High-resolution and real-time UWB radar imaging algorithm with direct waveform compensations," *IEEE Trans. Geosci. Remote Sens.*, vol. 46, no. 11, pp. 3503-3513, November 2008.

[7] L. Du, Y. Wang, W. Hong, W. Tan, and Y. Wu, "A three-dimensional range migration algorithm for downward-looking 3D-SAR with single transmitting and multiple-receiving linear array antennas," *EURASIP J. Adv. Signal Process.*, vol. 2010, article ID 957916, pp. 15, 2010.

[8] B. R. Mahafza and M. Sajjadi, "Three-dimensional SAR imaging using linear array in transverse motion," *IEEE Trans. Aerosp. Electron. Syst.*, vol. 32, no. 1, pp. 499-510, January 1996.

[9] S. Jun, X. L. Zhang, J. Y. Yang, and W. Chen, "APC trajectory design for one-active linear-array three-dimensional imaging SAR," *IEEE Trans. Geosci. Remote Sens.*, vol. 48, no. 3, pp. 1470-1486, March 2010.

[10] W. Matthias and G. Markus, "Initial ARTINO radar experiments," *presented at the 8th European Conference on Synthetic Aperture Radar*, Aachen, Germany, June 2010.

[11] J. M. Lopez- Sahcnez and J. Fortuny-Guash, "3D radar imaging using range migration techniques," *IEEE Trans. Antennas Propag.*, vol. 48, no. 5, pp. 728-737, May 2000.

[12] J. Fortuny-Guash and J. M. Lopez-Sahcnez, "Extension of the 3-D range migration algorithm to cylindrical and spherical scanning geometries," *IEEE Trans. Antennas Propag.*, vol. 49, no. 10, pp. 1434-1444, October 2001.

[13] X. J. Xu and R. M. Narayanan, "Three-dimensional interferometric ISAR imaging for target scattering diagnosis and modeling," *IEEE Trans. Image Process.*, vol. 10, no. 7, pp. 1094-1102, July 2001.

[14] Budillon, A. Evangelista, and G. Schirinzi, "Three-dimensional SAR focusing from multipass signals using compressive sampling," *IEEE Trans. Geosci. Remote Sens*., vol. 49, no. 1, pp. 488-499, January 2011.

[15] W. Qi, M. Xing, G. Lu, and Z. Bao, "High-resolution three-dimensional radar imaging for rapidly spinning targets," *IEEE Trans. Geosci. Remote Sens.*, vol. 46, no. 1, pp. 22-30, January 2008.

[16] G. Fornaro, D. Reale, and F. Serafino, "Four-dimensional SAR imaging for height estimation and monitoring of single and double scatterers," *IEEE Trans. Geosci. Remote Sens.*, vol. 47, no. 1, pp. 224-237, January 2009.

[17] S. Kidera, T. Sakamoto, and T. Sato, "High-resolution 3-D imaging algorithm with an envelope of modified spheres for UWB through-the-wall radars," *IEEE Trans. Antennas Propag.*, vol. 57, no. 11, pp. 3520-3529, November 2009.

[18] Y. Zhang, D. Huang, and J. Chen, "Combination of asymptotic phase basis functions and matrix interpolation method for fast analysis of monostatic RCS," *Applied Computational Electromagnetics Society (ACES) Journal*, vol. 28, no. 1, pp. 49-56, January 2013.

[19] Z. Liu, R. Chen, J. Chen, and Z. Fan, "Using adaptive cross approximation for efficient calculation of monostatic scattering with multiple incident angles," *Applied Computational Electromagnetics Society (ACES) Journal*, vol. 26, no. 4, pp. 325-333, April 2011.

[20] A. R. Mallahzadeh, J. Rashed-Mohassel, and M. Soleimani, "RCS computation of targets using three dimensional scalar parabolic equation," *Applied Computational Electromagnetics Society (ACES) Journal*, vol. 22, no. 2, pp. 254-259, July 2007.

[21] G. A. Deschamps, "Ray techniques in electromagnetics," *Proc. IEEE*, vol. 60, no. 9, pp. 1022-1035, September 1972.

[22] J. B. Keller, "Geometrical theory of diffraction," *J. Opt. Soc. Amer.*, vol. 52, pp. 116-119, February 1962.

[23] P. Y. Ufimtsev, "Method of edge waves in the physical theory of diffraction," (in Russian) *Transl.:Metod krayevykh volnv fizicheskoy teorii difraktsiiIzd-Vo Sov*, Radio, pp. 1-243, 1962.

[24] R. Solimene, A. Buonanno, F. Soldovieri, and R. Pierri, "Physical optics imaging of 3-D PEC objects: vector and multipolarized approaches," *IEEE Trans. Geosci. Remote Sens.*, vol. 48, no. 4, pp. 1799-1808, April 2010.

[25] S. L. H. Ling and R. Chou, "Shooting and bouncing rays: calculating the RCS of an arbitrarily shaped cavity," *IEEE Trans. Antennas Propagat.*, vol. 37, pp. 194-205, February 1989.

[26] H. Biglary and M. Dehmollaian, "Scattering of an object above a rough surface with impedance boundaries using IPO and FMM," *presented at IEEE Antennas and Propagation Society International Symposium*, Chicago, IL, July 8-14, 2012.

[27] H. Biglary and M. Dehmollaian, "RCS of a target above a random rough surface with impedance boundaries using GO and PO methods," *presented*

at IEEE Antennas and Propagation Society International Symposium, Chicago, IL, July 8-14, 2012.

[28] A. Ishimaru, "Electromagnetic wave propagation, radiation and scattering," 1st ed., *Englewood Cliffs, NJ: Prentice-Hall*, 1991.

[29] N. T. Nguyen, A. Rolland, and R. Sauleau, "Range of validity and accuracy of the hybrid GO-PO method for the analysis of reduced-size lens antennas: benchmarking with BoR-FDTD," *presented at Asia-Pacific Microwave Conference*, Macau, December 16-20, 2008.

[30] T. F. Eibert, "Modeling and design of offset parabolic reflector antennas using physical optics and multilevel fast multipole method accelerated method of moments," *presented at IEEE Multitopic Conference*, Islamabad, December 23-24, 2006.

[31] J. Perez and M. F. Catedra, "Application of physical optics to the RCS computation of bodies modeled with NURBS surfaces," *IEEE Trans. Antennas Propagat.*, vol. 42, pp. 1404-1411, October 1994.

[32] www.cst.com

[33] R. Bhalla and Hao Ling "A fast algorithm for signature prediction and image formation using the shooting and bouncing ray technique," *IEEE Trans. Antennas Propagat.*, vol. 43, pp. 727-731, July 1995.

[34] I. Y. Kelly, G. Benavides, R. Bhalla, H. Ling, W. J. Vogel, and H. D. Foltz, "Urban channel propagation modeling using the shooting and bouncing ray technique," *presented at IEEE Antennas and Propagation Society International Symposium*, Montreal, Quebec, Canada, July 13-18, 1997.

Amin B. Gorji was born in Cardiff, UK, in 1989. He received his B.Sc. degree in Eelectrical Engineering from Babol Noshirvani University of Technology, Babol, Iran in 2011. He is currently advancing his M.Sc. degree in Electromagnetics Engineering at Babol Noshirvani University of Technology. Since 2011, he has been an Assistant and Researcher with the Antenna and Microwave Laboratory, Babol Noshirvani University of Technology. His scientific fields of interest include microwave imaging based on time-reversal methods, measurement techniques of radar cross section and EM numerical techniques for solving scattering and radiation problems.

Bijan Zakeri was born in Babol, Iran in 1974. He received his M.Sc. and Ph.D. degrees in Electromagnetics Engineering from Amirkabir "Polytechnic" University of Technology, Tehran, Iran in 1999 and 2007, respectively. Since 2010, he is an Assistant Professor with Babol Noshirvani University of Technology, Babol, Iran. He also is the Director of Antenna and Microwave Laboratory and the Head of the Radar Research Team at Babol Noshirvani University of Technology. In 2011, he became the Head of the joint research project of Iran Marine Industries Organization (MIO) and Babol Noshirvani University of Technology entitled "*RCS, IR, and Acoustic Signature Reduction of Surface Naval Ships.*" He is currently a member of the Iranian Association of Information and Communication Technology. His current research activities are in the fields of computational electromagnetics, inverse scattering, radar microwave subsystems design, UWB antenna and Polin-SAR remote sensing.

Reza C. Janalizadeh was born in Rorkee, India in 1990. Since 2009, he has been preceding his B.Sc. undergraduate studies in Electrical Engineering at the University of Tehran, Tehran, Iran. In 2012, he joined the Antenna and Microwave Laboratory, Babol Noshirvani University of Technology, Babol, Iran as a Researcher in electromagnetic scattering field areas. His research interests include microwave radar remote sensing, EM scattering and wave propagation, inverse scattering and computational electromagnetics.

Small Reconfigurable Monopole Antenna Integrated with PIN Diodes for Multimode Wireless Communications

N. Ojaroudi [1], Y. Ojaroudi [2], S. Ojaroudi [2], Y. Ebazadeh [3], and M. Shirgir [3]

[1] Young Researchers and Elite Club
Islamic Azad University, Ardabil Branch, Ardabil, Iran
n.ojaroudi@yahoo.com

[2] Young Researchers and Elite Club
Islamic Azad University, Germi Branch, Germi, Iran
y.ojaroudi@iaugermi.ac.ir, s.ojaroudi.p@gmai.com

[3] Islamic Azad University, Germi Branch, Germi, Iran
y.ehazadeh@iaugermi.ac.ir, mehdi_shirgir@yahoo.com

Abstract **─** A new printed reconfigurable monopole antenna with multi-resonance and switchable dual band-notched performances is presented, whose frequency characteristics can be reconfigured electronically to have both a single or dual-band notch function to block interfering signals from Wireless Local Area Network (WLAN) for 5-6 GHz and/or X-band communications around 9-10 GHz. The presented antenna consists of a square radiating patch with H-shaped slot and a ground plane with a pair of L-shaped parasitic structures. We use two PIN diodes across the antenna configuration that by changing the on/off conditions of the PIN diodes, the antenna can be used for multimode applications. In the proposed structure, when D_1=ON & D_2=OFF, an UWB antenna with a multi-resonance characteristic can be achieved and we can give additional resonances at higher frequency bands that provides a wide usable fractional bandwidth of more than 125% (3.02-12.43). By changing the condition of integrated diodes to D_1=OFF & D_2=ON, the pair of rotated T-shaped slots at radiating patch have converted to H-shaped slot and the L-shaped parasitic structures have converted to inverted Ω-shaped structure. The proposed antenna can be used to generate either single or dual notch band to isolate and block any interference in the UWB frequency range.

Index Terms **─** PIN diode, reconfigurable antenna and UWB wireless communications.

I. INTRODUCTION

In UWB communication systems, one of key issues is the design of a compact antenna while providing a wideband characteristic over the whole operating band. Consequently, a number of microstrip antennas with different geometries have been experimentally characterized. Moreover, other strategies to improve the impedance bandwidth, which do not involve a modification of the geometry of the planar antenna have been investigated [1-3].

The frequency range for UWB systems between 3.1-10.6 GHz will cause interference to the existing wireless communication systems; for example, the WLAN for IEEE 802.11a operating in 5.15-5.35 GHz and 5.725-5.825 GHz bands and X-band communication systems, so the UWB antenna with a band-notched function is required. Lately, to generate the frequency band-notched function, several modified planar monopole antennas with band-notched characteristic have been reported [4-5].

In this paper, a reconfigurable square monopole antenna with single or dual-band notched and multi-resonance performances is presented. In the proposed structure, multimode operation is provided by changing the on/off

Submitted On: January 31, 2013
Accepted On: July 23, 2014

1054-4887 © 2014 ACES

conditions of the PIN diodes, that the antenna can be used to generate either a single or dual notch band to isolate and block any interference in the WLAN and/or X-band frequency bands. The size of the designed antenna is smaller than the UWB antennas with band-notched function reported recently [6-9].

II. ANTENNA DESIGN

The presented small square monopole antenna fed by a microstrip line is shown in Fig. 1, which is printed on FR4 substrate of thickness of 1.6 mm, permittivity of 4.4 and loss tangent of 0.018.

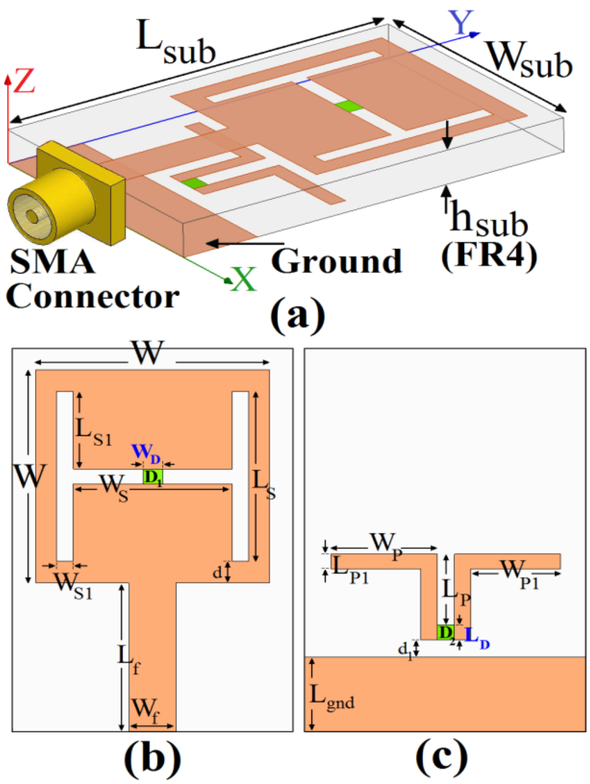

Fig. 1. Geometry of the proposed antenna: (a) side view, (b) top layer and (c) bottom layer.

The basic monopole antenna structure consists of a square patch, a feed line and a ground plane. The square patch has a width W. The patch is connected to a feed line of width W_f and length L_f. The width of the microstrip feed line is fixed at 2 mm, as shown in Fig. 1. On the other side of the substrate, a conducting ground plane is placed. The proposed antenna is connected to a 50- SMA connector for signal transmission. The final values of proposed design parameters are as follows: W_{sub}=12 mm, L_{sub}=18 mm, h_{sub}=1.6 mm, W_f=2 mm, L_f=7 mm, W=10 mm, W_S=6 mm, L_S=8 mm, W_{S1}=1 mm, L_{S1}=3.75 mm, L_{S2}=2 mm, W_P=4.75 mm, L_P=3.5 mm, W_P=4.25 mm, L_{P1}=0.5 mm, W_D=0.5 mm, L_D=0.5 mm, d=1 mm, d_1=0.75 mm and L_{gnd}=3.5 mm.

III. RESULTS AND DISCUSSIONS

The proposed microstrip monopole antenna with various design parameters was constructed and the numerical and experimental results of the input impedance and radiation characteristics are presented and discussed. Ansoft HFSS simulations are used to optimize the design and agreement between the simulation and measurement is obtained [10].

A. UWB antenna (D_1=ON and D_2=OFF)

The configuration of the presented reconfigurable monopole antenna was shown in Fig. 1. Geometry for the monopole antenna with a ground etch (Fig. 2 (a)), with a pair of rotated T-shaped slots (Fig. 2 (b)) and with a pair of rotated T-shaped slots and L-shaped parasitic structures (Fig. 2 (c)) are compared in Fig. 2.

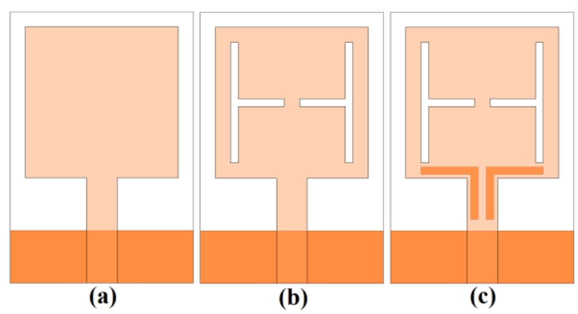

Fig. 2. (a) Basic structure (a square monopole antenna with a ground etch), (b) the antenna with a pair of rotated T-shaped slots and (c) antenna with a pair of rotated T-shaped slots and a pair of L-shaped conductor-backed plane.

Simulated VSWR characteristics for the structures that were shown in Fig. 2 are compared in Fig. 3. As shown in Fig. 3, it is observed that the upper frequency bandwidth is affected by using these structures and we can give additional resonances at higher bands that provide a wide usable fractional bandwidth.

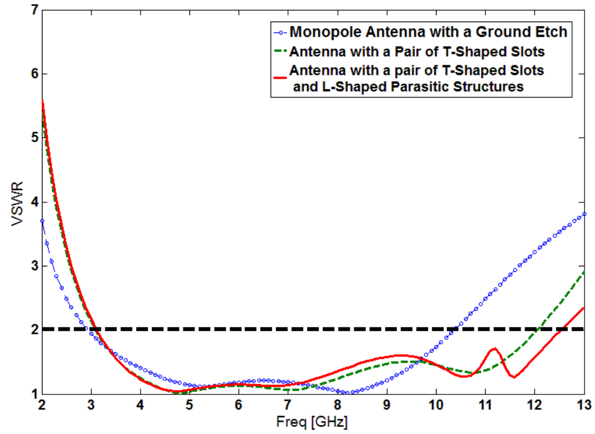

Fig. 3. Simulated VSWR characteristics for the various structures shown in Fig. 2.

In order to understand the phenomenon behind this multi-resonance performance, the simulated current distributions for the proposed antenna on the radiating patch at the third resonance frequency (10.7 GHz) is presented in Fig. 4 (a). It is found that by inserting a pair of rotated T-shaped slots, a new resonance at 10.7 GHz can be achieved. Another important design parameter of this multi-resonance performance is a pair of inverted L-shaped parasitic structure, that by adding this structure in the ground plane fourth resonance at 11.5 GHz has been obtained. The simulated current distributions for the proposed UWB antenna in the ground plane at 11.5 GHz (fourth resonance) are presented in Fig. 4 (b). As shown in Fig. 4 (b), the current flows are more dominant around of the L-shaped parasitic structures [11-13].

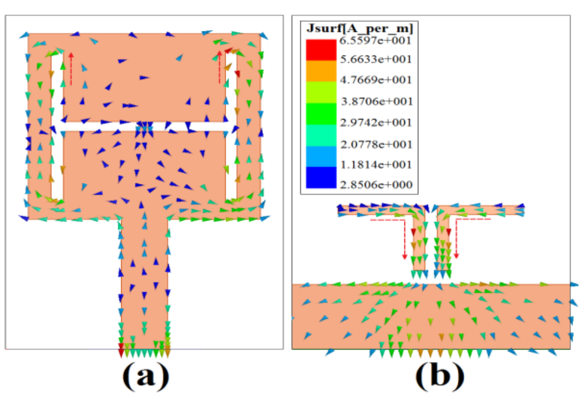

Fig. 4. Simulated surface current distributions for the UWB antenna: (a) on the radiating patch at 10.7 GHz and (b) in the ground plane at 11.5 GHz.

B. Single and/or dual band-notched antenna (D_1=OFF and/or D_2=ON)

In the proposed antenna configuration, by changing the conditions of the PIN diodes, the desired band notching characteristics can be achieved. Geometry for the UWB monopole antenna (D_1=ON and D_2=OFF) (Fig. 5 (a)), with a single band-notched function (D_1=OFF and D_2=OFF) (Fig. 5 (b)) and with dual band-notched function (D_1=OFF and D_2=ON) (Fig. 5 (c)) are compared in Fig. 5.

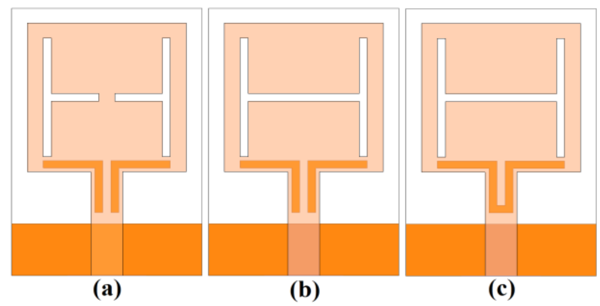

Fig. 5. Various structures for the proposed reconfigurable antenna: (a) D_1=ON & D_2=OFF, (b) D_1=OFF & D_2=OFF and (c) D_1=OFF & D_2=ON.

Simulated VSWR characteristics for the structures that were shown in Fig. 5 are compared in Fig. 6. As shown in Fig. 6, it is observed that the lower frequency band-notched function is affected by using an H-shaped slot on the radiating patch and by using an Ω-shaped conductor-backed plane, a dual band-notched performance has been obtained.

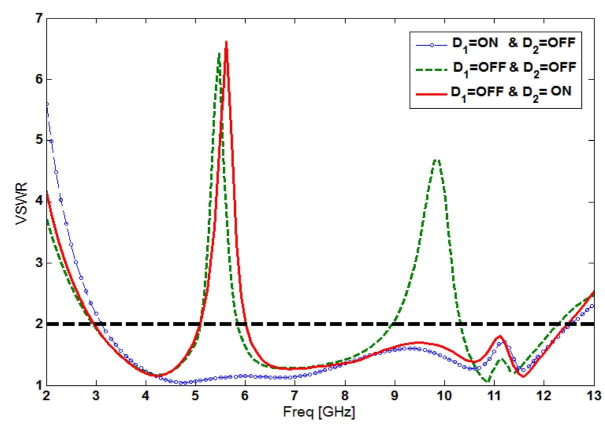

Fig. 6. Simulated VSWR characteristics for the various structures shown in Fig. 5.

To know the phenomenon behind this single or/and dual band-notched performance, the simulated current distributions for the proposed dual band-notched antenna on the radiating patch at 5.5 GHz (first band-notched) is presented in Fig. 7 (a). It is found that by inserting an H-shaped slot at radiating patch, a single band-notched function around 5-6 GHz can be achieved. Another important design parameter of this multi band-notched performance is an inverted Ω–shaped conductor-backed plane. By adding this structure in the ground plane, dual band-notched function has been obtained. The simulated current distributions for the proposed antenna in the ground plane at 9.5 GHz (second frequency band-notched) is presented in Fig. 7 (b). As shown in Fig. 7 (b), the current flows are more dominant around of the inverted Ω-shaped parasitic structure [14].

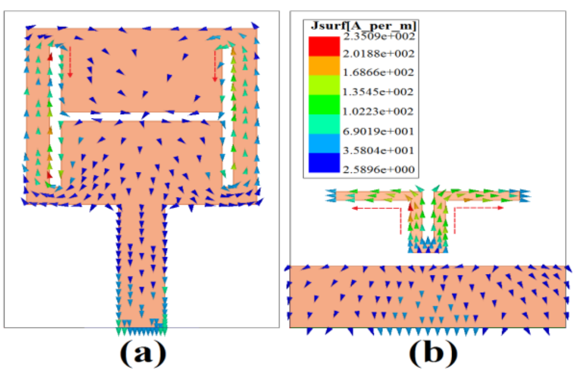

Fig. 7. Simulated surface current distributions for the antenna at the notched frequencies: (a) on the radiating patch at 5.5 GHz and (b) in the ground plane at 9.5 GHz.

For applying the DC voltage to PIN diodes, metal strips with dimensions of 1.2 mm ×0.6 mm were used inside the main slots. In the introduced design, HPND-4005 beam lead PIN diodes [15] with extremely low capacitance were used. For biasing PIN diodes, a 0.7 volt supply is applied to metal strips. The PIN diodes exhibit an ohmic resistance of 4.6 Ω and capacitance of 0.017 pF in the on and off states, respectively. By turning diodes on, the embedded H-shaped slot was converted to the pair of T-shaped slot and the metal L-shaped strips are connected to each other and become a Ω-shaped strip. The desired notched frequency bands can be selected by varying the states of the PIN diodes, which changes the total equivalent length of the strip and slot structures.

The proposed microstrip monopole antenna with final design as shown in Fig. 8, was built and tested and the VSWR and characteristic was measured using a network analyzer.

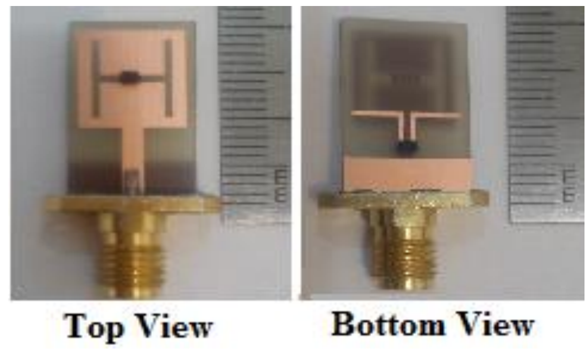

Fig. 8. Photograph of the realized antenna.

The radiation patterns have been measured inside an anechoic chamber using a double-ridged horn antenna as a reference antenna placed at a distance of 2 m. Also, a two-antenna technique using a spectrum analyzer and a double-ridged horn antenna as a reference antenna placed at a distance of 2 m, is used to measure the radiation gain in the z axis direction (x-z plane) [16].

The measured and simulated VSWR characteristics of the proposed antenna in multimode operations were shown in Fig. 9. The presented antenna has the frequency band of 3.02 to over 12.43 GHz, with a variable single and/or dual band-stop performance.

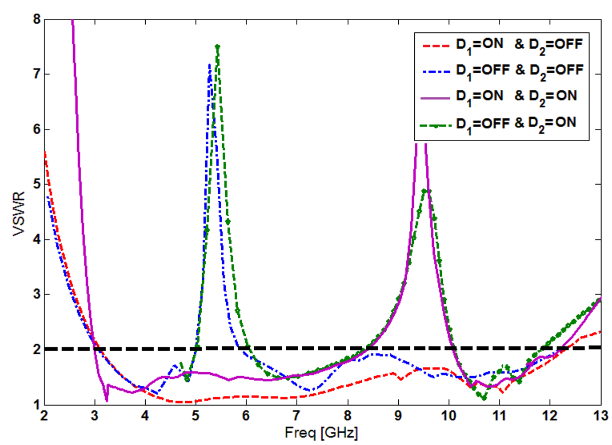

Fig. 9. Measured VSWR characteristics for the proposed antenna.

However, as seen, there exists a discrepancy between measured data and the simulated results. This discrepancy is mostly due to a number of parameters, such as the fabricated antenna dimensions as well as the thickness and dielectric constant of the substrate on which the antenna is fabricated and the wide range of simulation frequencies. In a physical network analyzer measurement, the feeding mechanism of the proposed antenna is composed of a SMA connector and a microstrip line (the microstrip feed-line is excited by a SMA connector); whereas, the simulated results are obtained using the HFSS, that in HFSS by default, the antenna is excited by a wave port that it is renormalized to a 50-Ohm full port impedance at all frequencies. In order to confirm the accurate return loss characteristics for the designed antenna, it is recommended that the manufacturing and measurement processes need to be performed carefully. Moreover, SMA soldering accuracy and FR4 substrate quality need to be taken into consideration.

Figure 10 depicts the measured and simulated radiation patterns of the proposed antenna, including the co-polarization and cross-polarization in the H-plane (x-z plane) and E-plane (y-z plane). It can be seen that quasi-omnidirectional radiation pattern can be observed on x-z plane over the whole UWB frequency range, especially at the low frequencies. The radiation pattern on the y-z plane displays a typical figure-of-eight, similar to that of a conventional dipole antenna. It should be noticed that the radiation patterns in E-plane become imbalanced as frequency increases, because of the increasing effects of the cross-polarization. The patterns indicate at higher frequencies and more ripples can be observed in both E and H-planes, owing to the generation of higher-order modes. [17-18].

Measured maximum gain levels of the proposed antenna with different conditions of active elements were shown in Fig. 11. The antenna gain has a flat property, which increases by the frequency. As illustrated, two sharp decreases of maximum gain in the notched frequency bands at 5.5 and 9 GHz are shown in Fig. 11. As seen, the proposed antenna has sufficient and acceptable gain levels in the operation bands [19].

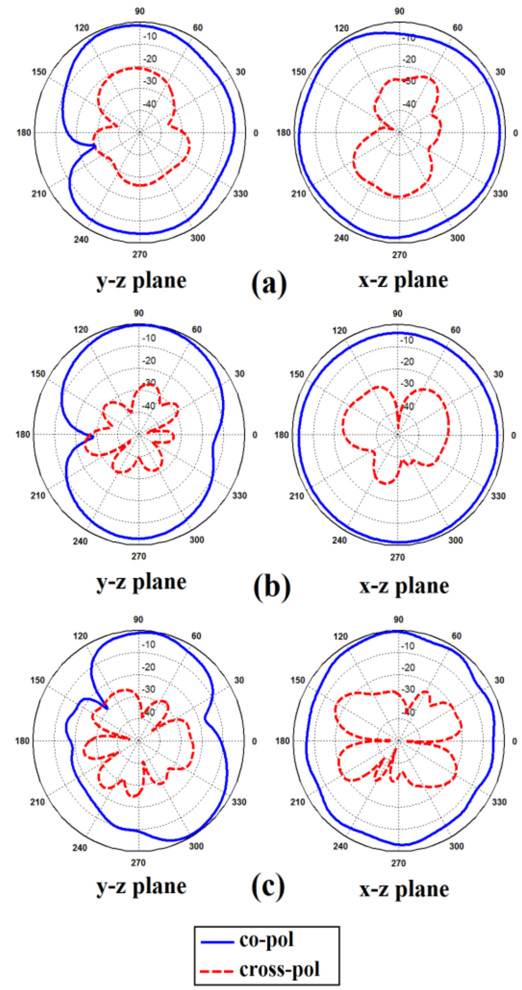

Fig. 10. Measured radiation patterns of the antenna for D_1=OFF & D_2=ON: (a) 4 GHz, (b) 7.5 GHz and (c) 11 GHz.

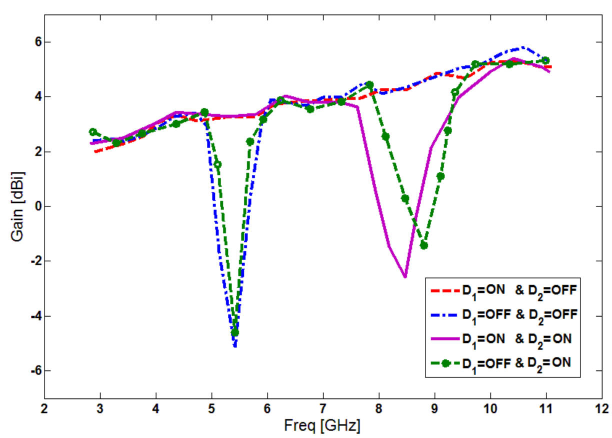

Fig. 11. Measured maximum gain characteristics for the proposed antenna.

IV. CONCLUSION

A new reconfigurable monopole antenna with electrically switchable notch band and multi-resonance functions for UWB applications is presented. The antenna is reconfigurable to suppress unwanted interfering signals by using PIN diodes integrated within the antenna configuration. By changing the on/off conditions of the PIN diodes, the antenna can be used to generate either a single or dual notch band to isolate and block any interference in the X-band and/or WLAN frequency bands. Simulated and experimental results show that the proposed antenna could be a good candidate for UWB applications.

ACKNOWLEDGMENT

The authors are thankful to MWT Company staff for their help (www.microwave-technology.com).

REFERENCES

[1] H. Schantz, "The art and science of ultra wideband antennas," *Artech House*, 2005.

[2] N. Ojaroudi, "Design of ultra-wideband monopole antenna with enhanced bandwidth," *21st Telecommunications Forum, TELFOR 2013*, Belgrade, Serbia, pp. 1043-1046, November 27-28, 2013.

[3] N. Ojaroudi, "A new design of koch fractal slot antenna for ultra-wideband applications," *21st Telecommunications Forum, TELFOR 2013*, Belgrade, Serbia, pp. 1051-1054, November 27-28, 2013.

[4] N. Ojaroudi, "Application of protruded strip resonators to design an UWB slot antenna with WLAN band-notched characteristic," *Progress In Electromagnetics Research C*, vol. 47, pp. 111-117, 2014.

[5] N. Ojaroudi, "Small microstrip-fed slot antenna with frequency band-stop function," *21st Telecommunications Forum, TELFOR 2013*, Belgrade, Serbia, pp. 1047-1050, November 27-28, 2013.

[6] D. Piazza, P. Mookiah, M. D'Amico, and K. R. Dandekar, "Experimental analysis of pattern and polarization reconfigurable circular patch antennas for MIMO systems," *IEEE Trans. Veh. Technol*, vol. 59, pp. 2352-2362, 2010.

[7] S. L. S. Yang, A. A. Kishk, and K. F. Lee, "Frequency reconfigurable u-slot microstrip patch antenna," *IEEE Antennas Wirel. Propag. Lett.*, vol. 7, pp. 127-129, 2008.

[8] S. Nikolaou, N. D. Kingsley, G. E. Ponchak, J. Papapolymerou, and M. M. Tentzeris, "UWB elliptical monopoles with a reconfigurable band notch using MEMS switches actuated without bias lines," *IEEE Trans. Antennas Propag.*, vol. 57, pp. 2242-2251, 2009.

[9] Y. Li, W. Li, and W. Yu, "A switchable UWB slot antenna using SIS-HSIR and SIS-SIR for multi-mode wireless communications applications," *Applied Computational Electromagnetics Society (ACES) Journal*, vol. 27, no. 4, pp. 340-351, April 2012.

[10] "Ansoft high frequency structure simulation (HFSS)," ver. 13, *Ansoft Corporation*, 2010.

[11] N. Ojaroudi, "Design of microstrip antenna for 2.4/5.8 GHz RFID applications," *German Microwave Conference, GeMic 2014*, RWTH, Aachen University, Germany, March 10-12, 2014.

[12] N. Ojaroudi, "Microstrip monopole antenna with dual band-stop function for UWB applications," *Microw. Opt. Technol. Lett.*, vol. 56, pp. 818-822, 2014.

[13] N. Ojaroudi, "Circular microstrip antenna with dual band-stop performance for ultra-wideband systems," *Microw. Opt. Technol. Lett.*, vol. 56, pp. 2095-2098, 2014.

[14] M. R. Hamid, P. S. Hall, P. Gardner, and F. Ghanem, "Switched WLAN wideband tapered slot antenna," *Electronics Letters*, vol. 46, pp. 23-24, 2010.

[15] HPND-4005, "Beam lead PIN diode," *Avago Technologies*.

[16] K. C. Chen and R. Prasad, "Cognitive radio networks," *John Wiley & Sons*, West Sussex, United Kingdom, 2009.

[17] N. Ojaroudi, N. Ghadimi, and Y. Ojaroudi, "UWB microstrip-fed slot antenna with band-rejection performance using an SRR conductor-backed plane," *Applied Computational Electromagnetics Society (ACES) Journal*, vol. 29, no. 3, pp. 203-207, 2014.

[18] N. Ojaroudi, M. Mehranpour, S. Ojaroudi, and Y. Ojaroudi, "Application of the protruded structures to design an UWB slot antenna with band-notched characteristic," *Applied Computational Electromagnetics Society (ACES) Journal*, vol. 29, no. 2, pp. 184-189, 2014.

[19] N. Ojaroudi, S. Amiri, and F. Geran, "A novel design of reconfigurable monopole antenna for UWB applications," *Applied Computational Electromagnetics Society (ACES) Journal*, vol. 28, no. 6, pp. 633-639, July 2013.

Evolutionary Design of a Wide Band Flat Wire Antenna for WLAN and Wi-Fi Applications

Giovanni Andrea Casula, Giorgio Montisci, Alessandro Fanti, Paolo Maxia, and Giuseppe Mazzarella

Dipartimento di Ingegneria Elettrica ed Elettronica
Università di Cagliari, Piazza D'Armi, 09123 Cagliari, Italy
a.casula@diee.unica.it, mazzarella@diee.unica.it, giorgiom@diee.unica.it, paolo.maxia@diee.unica.it, alessandro.fanti@diee.unica.it

Abstract ─ This paper presents a wire antenna for multi-band WLAN application, having a very simple geometry, designed using the Structure-Based Evolutionary Programming; an innovative antenna design technique, based on evolutionary programming. The chosen fitness function includes far-field requirements, as well as wideband input matching specifications. The latter requirements, which must be present in every useful antenna design, allow to stabilize the algorithm and to design both optimal and robust antennas. The antenna has been analysed with NEC-2 during the evolutionary process and the outcome of the procedure shows a very good performance; with a -10dB bandwidth that covers the required frequencies for multi-band WLAN applications (2.4/5.2/5.8 GHz) and beyond, and an end-fire gain greater than 10 dB. The NEC-2 results have been also compared to the ones obtained by a well-assessed, general purpose, 3D electromagnetic software, HFSS by Ansys, showing a very good agreement.

Index Terms ─ Evolutionary programming, wide band antennas and wire antennas.

I. INTRODUCTION

The rapid development of short-range radio links in the mobile communications industry, such as Bluetooth (BT), Wi-Fi and Wireless Local Area Network (WLAN), calls for antennas offering wideband operations covering the whole WLAN services. The desirable frequency bands required to a single antenna are: 2.4-2.484 GHz for BT applications, 2.4 GHz and 5 GHz for Wi-Fi applications (following HiperLan protocol) and 2.4 GHz, 5.2 GHz and 5.8 GHz for WLAN applications (following WLAN IEEE 802.11 standards).

Different WLAN antennas in planar technology have been recently proposed, based on known antenna concepts, but showing either a multiband [1] or a tuneable behavior [2]. So, significant improvements are yet to be reached, though a few wideband wire antennas have been proposed [3]. In the past literature, antenna design has been performed at different levels, from simple formulas [4] to sophisticated synthesis techniques [5]-[13], heuristic models [14] and random optimization procedures [15]. All of them, however, require a quite detailed specification of the antenna structure from the beginning, so that they can be more or less considered as dimensioning approaches.

A significant breakthrough can be achieved only by exploring new design concepts, allowing more general solution spaces to be searched in an effective way. Among them, Structure-Based Evolutionary Design (SED) has recently emerged as a new design paradigm [16-18]. SED provides a method for automatically creating a high-level working structure description, delivering elegant human-like solutions not anticipated by the programmer, requiring only a minimum amount of pre-supplied human knowledge, analysis and information. With SED, if we have to design a wire antenna following predetermined requirements, the procedure is able to look for the final design among all possible wire antennas. Therefore, SED can be used to automatically

Submitted On: May 7, 2013
Accepted On: July 25, 2014

search, in this very huge solution space, for novel antenna configurations, which can be significantly more performant than antennas developed using standard techniques.

In this work, a very simple wire antenna is proposed covering the full WLAN range. The proposed antenna has been designed exploiting the power of the Structure-Based Evolutionary Design (SED).

II. STRUCTURE-BASED EVOLUTIONARY DESIGN

The traditional approach to the design of wire antennas starts by choosing a well-defined antenna structure, able to comply with the design specifications and whose parameters need to be suitably optimized. Besides, a good design requires also a continuous human monitoring, especially to trim the initial structure to better fit the antenna specifications, together with a deep knowledge and experience in order to effectively change the structure under design. This traditional approach is quite expensive and therefore, design techniques without human interaction are of increasing interest, as long as they are able to provide equal or better results. This can be achieved only when no initial structure is assumed, since this choice (by necessity fixed in a fully automated procedure) can constrain too strongly the final solution.

An effective way to pursuit this approach is SED. SED is a new global random search method derived by the strategy first proposed by Koza [19]. The SED approach mimics the behavior of the natural evolution for the search of the individual showing the best adaptation to the local environment (in our case, to the requirement we set). As a matter of fact, Darwin stated that “the natural system is founded on the descent with modification” [20], since what is commonly named natural selection, is a process leading to biological units better matched to local changing environments. Therefore, from a conceptual point of view, design approaches based on natural selection should be formulated as a search for antennas fulfilling a set of antenna specifications (the local changing environment), rather than as optimization of a given performance index. SED allows following this paradigm and in a way closer to how natural selection works. Natural selection has, in fact, a number of peculiar characteristics. First, if we look at it in a functional, or effective way, it works at the organ level. Moreover, it allows an enormous variability, which is limited only by some broad-sense constraints.

Each individual in SED is a “computer program;” i.e., a sequential set of unambiguous instructions completely (and uniquely) describing the physical structure of an admissible antenna and its realization. In the practical implementation of SED, populations of antennas (descriptions traditionally stored as tree structures) are genetically bred; this breeding is made using the Darwinian principle of survival and reproduction of the fittest, along with recombination operations appropriate for mating computer programs. Tree structures can be easily evaluated in a recursive manner; every tree node has an operator function and every terminal node has an operand, making mathematical expressions easy to evolve and to be evaluated. At each iterative step, the fitness of those individuals is evaluated, in order to select the ones best adapted to the design specifications. Then, a new population is obtained, by a suitable implementation of standard “evolutionary” operators like cross-over and mutation.

As a matter of fact, the SED does not require any antenna model, neither asks for a structure locked from the beginning, but it considers a virtually infinite solution space, defined only by very loose constraints. SED allows to automate the whole project (and not only its repetitive parts) and provides original solutions, not achievable using standard design techniques. This is obtained since the whole antenna is described in terms of elementary parts (wire segments, junctions, and so on) and of their spatial relations (distance, orientation). In this way, the final antenna is sought for in an enormous search space, with a very large number of degrees of freedom, which leads to better solutions both in terms of performance and overall dimensions.

SED optimization process starts with a random initial population and it may move in different directions, converging to different results for the final designed antenna. SED start point is totally random; it is a global optimization method, particularly suitable for solving problems with several parameters and no clear starting location in the solution space. The solution space; i.e., the set of admissible solutions in which the procedure looks for the optimum, has the power of the continuum. This is the main advantage of SED, since it allows exploring and evaluating, general structure configurations, but on the other hand, it can lead to a severely ill-conditioned synthesis problem. As a consequence, a naive implementation usually does not work, since different starting populations lead to completely different final populations, possibly containing only individuals poorly matched to the requirements (a phenomenon similar to the occurrence of traps in optimization procedures).

A suitable stabilization is therefore needed. This role can be accomplished by suitable structure requirements, or forced by imposing further constraints, not included in the structure requirements. Whenever possible, the former ones are the better choice and should be investigated first. Typically, a high number N of individuals for a certain number of generations must be evaluated in order to obtain a good result from the design process. Since each individual can be evaluated independently from each other, the design process is strongly parallelizable and this can significantly reduce the computation time.

The main operators used in SED to build up the new generations are:

1. Cross-over: switching one sub-tree of an individual with a randomly selected sub-tree from another individual in the population. The expressions resulting from a single cross-over can be either quite close or very different from their initial parents. This sudden jump from an individual to a very different one is a powerful trap-escaping mechanism.
2. Mutation: modifies a whole node in the selected individual. In order to maintain integrity, operations must be fail-safe; therefore, the type of information the node holds must be taken into account.

The performance of each individual in the population is measured by a suitable fitness function, tailored to the problem at hand. Different fitness functions, built from different requirements, can lead to completely different results; each one best fitted to the corresponding original requirements.

SED has been used here to design a wideband wire antenna with an end-fire radiation pattern and a very simple geometry, operating in a range from L to C frequency bands, namely from 1 GHz to 6 GHz and with a very good input matching. Apart from these simple "constraints." SED does not assume any other a priori information on the antenna structure, building up the structure of the individuals-antennas as the procedure evolves.

In the design process, each individual in the population represents an admissible antenna. The performances of each antenna are evaluated by NEC-2 [21], a well assessed Method of Moments code, successfully used to model a wide range of wire antennas and considered as one of the reference electromagnetic software. The best individual obtained by the SED has been analysed also using a well-assessed, general purpose, 3D electromagnetic software, HFSS by Ansys. The results obtained by HFSS have been compared with NEC-2 simulations, showing a very good agreement.

III. ANTENNA STRUCTURE AND DESIGN

SED is a global random search procedure, looking for individuals best fitting a given set of specifications. These individuals are described as instruction sets and internally represented as trees. The main steps of the whole evolutionary design can be summarized in the flowchart of Fig. 1.

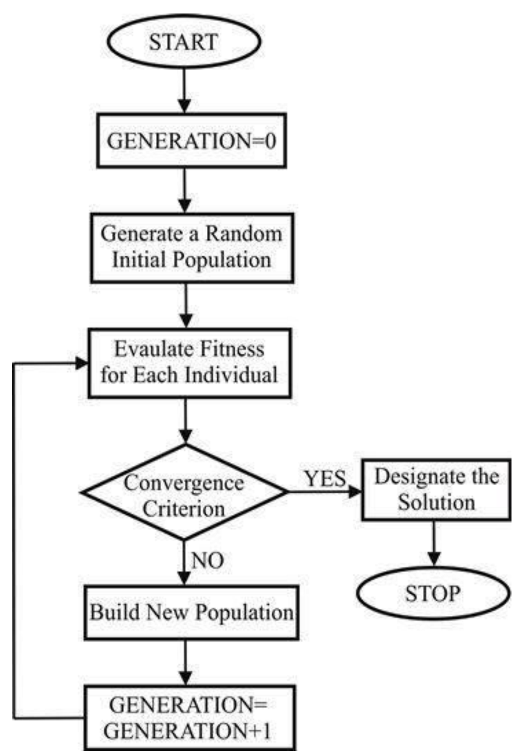

Fig. 1. Flowchart of the evolutionary design.

The initial structure of each individual of the population (antenna) generated by SED, is depicted in Fig. 2 (a) and is composed by a principal vertical wire (the main dipole in Fig. 2 (a)), connected to the feeding port on its bottom side and by a number N (chosen by SED) of wires connected to the upper side of the Main Dipole with an arbitrary length and orientation in space. At the remote end of each of the N wires, the SED procedure can connect zero, one or more further wires; still with arbitrary length and orientation, and so on, in an iterative manner. The structure is finally mirrored with respect to the horizontal plane, as indicated in Fig. 2 (a).

The proposed antenna is a broadband antenna, whose principle is not based on the principle of self-similarity like the bi-conical, spiral or log-periodic antennas. As shown in Fig. 2, where both the antenna geometry (Fig. 2 (a)) and the final designed antenna after the optimization process (Fig. 2 (b)) are depicted, the designed antenna is simply a branched dipole antenna suitably arranged in space. This choice strongly simplifies the antenna feeding network (which is simply a dipole feeding node) with respect to other broadband antennas, such as log-periodic dipole antennas (which need a twisted cable feeding network).

Each individual is built up using one of the following operations:

1. Add a wire according to the present directions and length.
2. Transform the end of the last added wire in a branching point.
3. Modify the present directions and length.
4. Stretch (or shrink) the last added wire.

This mixed representation largely increases the power of the standard genetic operations (mutation and cross-over), since each element can evolve independently from the others. Of course, after each complete antenna is generated, its geometrical coherency is verified, and incoherent antennas (e.g., an antenna with two elements too close, or even intersecting) are discarded.

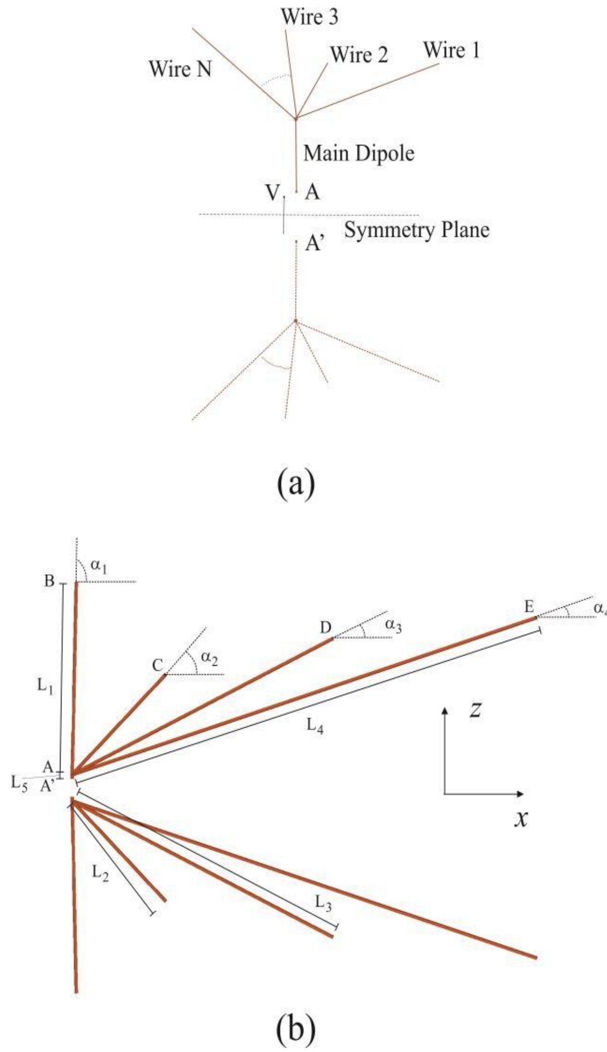

Fig. 2. (a) Wire antenna geometry and (b) geometry of the final designed wire antenna after optimization: L_1=195.1 mm, L_2=144.6 mm, L_3=311.8 mm, L_4=522 mm, α_1=88.6° mm, α_2=44.7°, α_3=25.6° and α_4=17.4°.

The SED approach has been implemented in Java, while the analysis of each individual has been implemented in C++ (using the freeware source code Nec2cpp) and checked using the freeware tool 4nec2. The integration with NEC-2 has mainly been achieved through three classes:

1. A parser for the conversion of the s-expressions, represented as n-ary trees, in the equivalent NEC input files.
2. A NecWrapper, which writes the NEC listing to a file, launches a NEC2 instance in a separate process and parses the output generated by NEC.
3. An Evaluator, which calculates the fitness using the output data generated by NEC.

The evaluation procedure for each individual (i.e., for each antenna) can be described by the flowchart in Fig. 3.

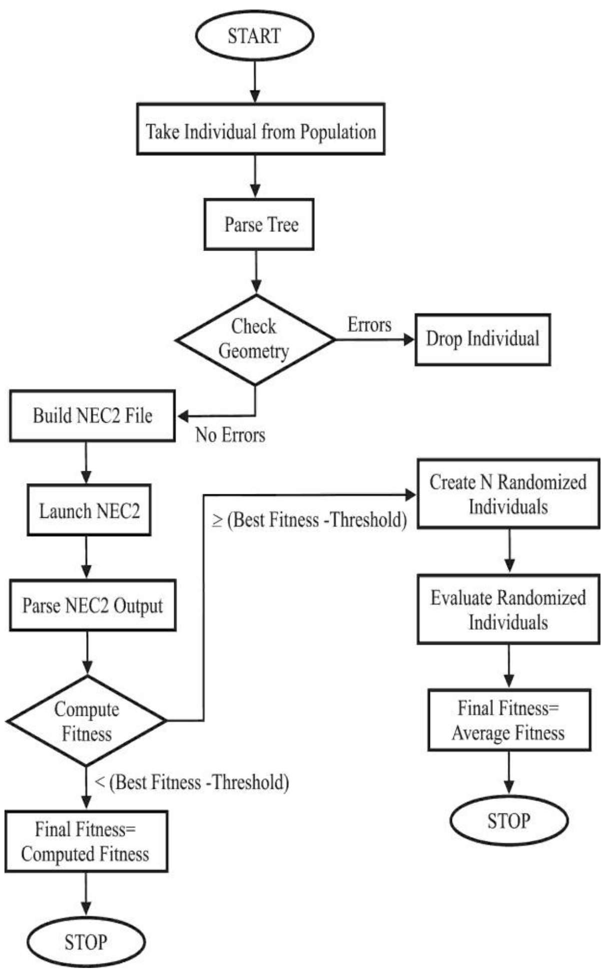

Fig. 3. Flowchart of the evaluation procedure for each individual of the population.

In the first step of the evolutionary design, N individuals are randomly built. Then, an iterative procedure starts, where the fitness of each individual is evaluated and the next generation of the population is built assigning a larger probability of breeding to the individuals with the highest fitness. The iterative procedure ends when suitable stopping rules are met (i.e., when the individual-antenna fulfills, within a predetermined tolerance, the specified requirements).

After each antenna has been generated, its geometrical coherency is verified, and incoherent antennas (e.g., an antenna with two elements too close, or even intersecting) are discarded. Then it is analysed by NEC-2 [21] and its fitness is computed.

The performance of each individual (antenna) of the population is evaluated by a proper fitness function, which is strongly dependent by the problem at hand, namely by the electromagnetic behavior of the designed antenna and must measure how closely the actual antenna meets the design specifications.

In the specific case of the broadband wire antenna of this paper, the fitness function has been selected in order to lead the evolution process toward a structure with a good input match in a frequency range as wide as possible (within L, S and C Bands), while keeping the highest end-fire gain and a reduced size. In order to obtain a very simple and compact antenna, we impose the following constraints to the evolution process:

1. Individuals must lie over a plane, namely the *xz* plane.
2. No further wire can be connected at the remote end of each of the N wires shown in Fig. 2 (a).
3. A larger weight is assigned to the fitness of the individuals with a size lower than 0.1 square meters.

Since the increase in a parameter (i.e., the gain) usually results in a reduction in the other ones (i.e., frequency bandwidth and input matching), the design procedure must manage an elaborate trade-off between these conflicting goals. Therefore, the form of the fitness function can be a critical point, since only a suitable fitness can lead the design process to significant results. Moreover, depending on the used fitness, the computation time can be largely reduced (i.e., a good result can be obtained with less generations).

The chosen fitness has been built from the desired antenna performances [16-18] as:

$$Fitness = \left(\left| 1 - \overline{SWR} \right| \cdot \alpha_{SWR} + \left| \frac{G_{MAX}}{\overline{G}} \right| \cdot \alpha_{GAIN} \right) \cdot \left(1 + \frac{D_{MAX}}{D_{ANT}} \cdot K_{SIZE} \right), \quad (1)$$

wherein α_{SWR} and α_{GAIN} are suitable weights (whose values depend also on the input impedance of the actual antenna), $\overline{SWR}$ and $\overline{G}$ are, respectively, the mean values of the antenna Standing Wave Ratio (SWR) and of the antenna gain G over the bandwidth of interest, D_{ANT} represents the actual antenna size and D_{MAX} is the maximum allowed size for the antenna; which is equal to 0.2 m^2 in this case. Finally, K_{SIZE} is an appropriate weight, which takes into account the requirement of a small size of the antenna and is equal to 0.65 in this case. The values for the fitness weights have been obtained after a suitable local tuning, following an approach similar to the one described in detail in [16-18] voltage.

The weight α_{GAIN} in the fitness function (1) has the following expression:

$$\alpha_{\text{GAIN}} = \left(1+\alpha_{\text{Back}} * G_{\text{Back}}\right)\cdot\left(1+\alpha_{\text{Rear}} * G_{\text{Rear}}\right) \cdot\left(1+\alpha_{\text{Front}} * G_{\text{Front}}\right) \quad , (2)$$

where G_{Back} is the gain computed in the back direction (θ=90°; φ=180°), G_{Front} is the average gain computed in the front region ($|\theta|>90°+2\Delta\vartheta$; $0°+2\Delta\varphi<\varphi<90°$, where $\Delta\vartheta$ and $\Delta\varphi$ indicate the main lobe amplitude) and G_{Rear} is the average gain computed in the rear region ($0°\leq|\vartheta|\leq180°$; $90°\leq|\varphi|\leq180°$). The weigths α_{Back}, α_{Front} and α_{Rear} are chosen through a local tuning, in order to get the maximum gain in the end-fire direction and an acceptable radiation pattern in the rest of the space. After the evolutionary process, these parameters assume the following values: α_{Back}=0.12, α_{Front}=0.17 and α_{Rear}=0.06.

The weight α_{SWR} in the fitness function (1) is expressed using suitable parameters strictly related to the antenna input impedance, which are individually tuned. The resulting expression for α_{SWR} is:

$$\alpha_{\text{SWR}} = \left(1+\alpha_{\text{IN}}\right)\cdot\left(1+\alpha_{\text{X}}\left|X_{IN}^{A}\right|\right)\cdot\left(1+\alpha_{\text{Q}}\frac{R_{IN}^{A}-\left|X_{IN}^{A}\right|}{R_{IN}^{A}}\right) \cdot\left(1+\alpha_{\text{VarR}}\cdot\sigma_{\text{R}}^{2}\right)\cdot\left(1+\alpha_{\text{VarX}}\cdot\sigma_{\text{X}}^{2}\right) \quad , (3)$$

where:

- α_{IN}=50 if $|X_{IN}^A|> R_{IN}^A$ and α^{IN}=0 otherwise (weight introduced in order to boost up structures with $R_{IN}^A> |X_{IN}^A|$);
- α_X=0.12 (weight related to $|X_{IN}^A|$, introduced in order to force the evolution process to structures with an $|X_{IN}^A|$ as small as possible);
- α_Q=0.2 (weight related to $R_{IN}^A-|X_{IN}^A|$, introduced to advantage structures with a low Q factor);
- $\alpha_{VarR}=\alpha_{VarX}$=0.03 (weight related to the normalized mean square variation of R_{IN}^A and X_{IN}^A in the antenna required bandwidth, introduced to advantage structures with a regular impedance behaviour);

R_{IN}^A and X_{IN}^A are, respectively, the real part and the imaginary part of the antenna input impedance, while σ_{R2} and σ_{X2} are the normalized mean square variation of R_{IN}^A and of X_{IN}^A in the antenna required bandwidth. The two weights α_{IN} and α_Q are both connected to the Q factor of the antenna. However, α_{IN} gives a significant penalization to antennas with a large imaginary part of the input impedance, but it has a step-like behavior. Therefore, in order to get a further, smooth penalization to antennas with a large Q, we have added also the term with α_Q. We have observed that a combination of the two terms is more effective than either one separately.

The requirement of a given and low VSWR all over the design bandwidth, is obviously needed to effectively feed the designed antenna. Moreover, the VSWR requirement (which is a near-field requirement) allows to stabilize the severely ill-conditioned synthesis problem (due to the extremely large SED solution space), at virtually no additional cost.

IV. RESULTS

The best individual of the evolution is shown in Fig. 2 (b), and the Cartesian coordinates of each wire are reported in Table 1; each wire has a diameter of 1.77 mm and is made by copper with a conductivity of $\sigma=5.8*10^7$ S/m. The designed antenna lies on the *xz* plane and occupies an area of only 0.498x0.195 square meters. This antenna is extremely easy to realize, especially due to its planar configuration and can be produced with a very low cost by the same technology used for Yagi and LPDA arrays.

Table 1: Cartesian coordinates of the ends of the wires for the antenna in Fig. 2 (b)

	X [mm]	Z [mm]
A	0	5.327
B	4.511	195.025
C	102.815	101.698
D	280.852	135.408
E	498.249	155.577

The antenna has been designed using a population size of 1000 individuals, with a crossover rate set to 60% and a mutation rate set to 40%. Its convergence plot is shown in Fig. 4, and it appears that 150 generations are enough to reach convergence.

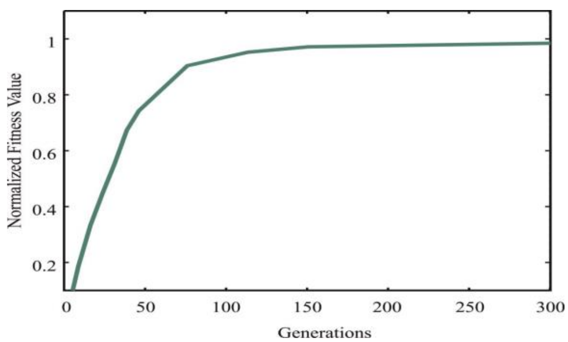

Fig. 4. Plot of convergence of the designed antenna shown in Fig. 2 (b).

The frequency response of the designed antenna, simulated using NEC-2, is reported in Fig. 5. The S11 module is below -10 dB in a frequency band, which extends from 1 GHz up to well beyond 6 GHz, showing a very good input matching within the whole operating bandwidth. In order to validate these results, since sometimes the S11 data of NEC-2 could have a reduced accuracy, the designed antenna has been simulated also with HFSS, a commercial FEM code which has been demonstrated to be in very good agreement with experimental data and the results are reported in Fig. 5. This comparison shows that NEC-2 and HFSS results are in very good agreement.

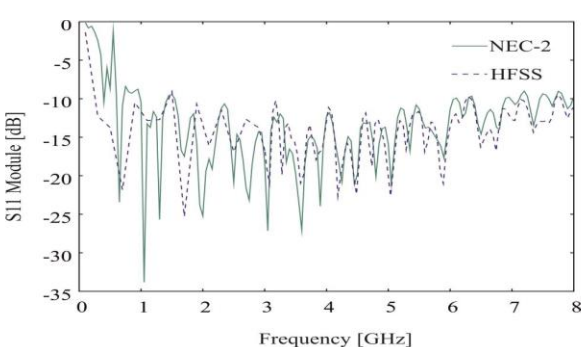

Fig. 5. Reflection coefficient of the designed antenna.

The end-fire Gain of the designed antenna, plotted in Fig. 6, remains higher than 10 dB both in the Bluetooth, Wi-FI and WLAN operating bandwidths. Also, the front-to-back ratio, plotted in Fig. 7, is higher than 10 dB in the frequency bandwidth 2-6 GHz. In the bandwidth 1-6 GHz, the mean Gain of the antenna is equal to 10.5 dB and the mean F/B ratio is about 14 dB.

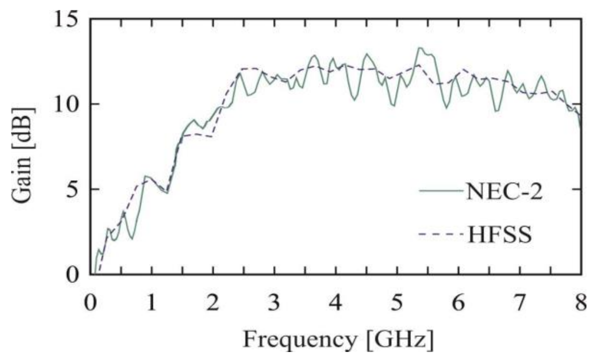

Fig. 6. Gain of the designed antenna.

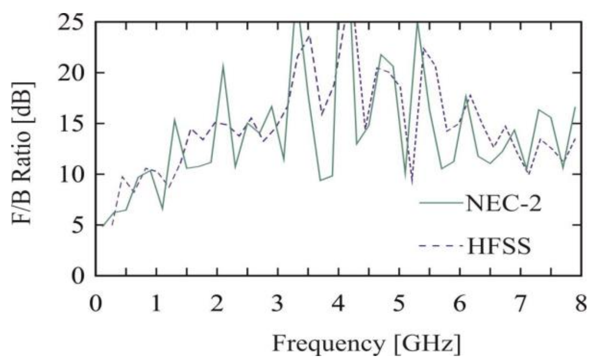

Fig. 7. Front-to-back ratio of the designed antenna.

Figure 8 shows the antenna efficiency, which is above 99% in the bandwidth of interest (2-6 GHz). The inclusion of ohmic losses into the gain computation is very important, since this prevents from selecting super-directive antennas during the evolution, as we thoroughly explained in [22].

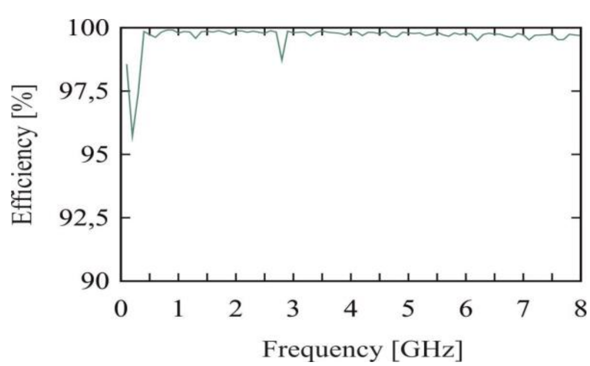

Fig. 8. Efficiency of the designed antenna.

Finally, the NEC-2 Far Field Pattern in the operating frequency bandwidth is plotted in Fig. 9. For each frequency, the E-plane and the H-plane are shown. The reported radiation patterns confirm that the useful bandwidth of the designed antenna is 1-6 GHz, where the input matching is very good and the far field is essentially end-fire, with a good Gain and F/B ratio.

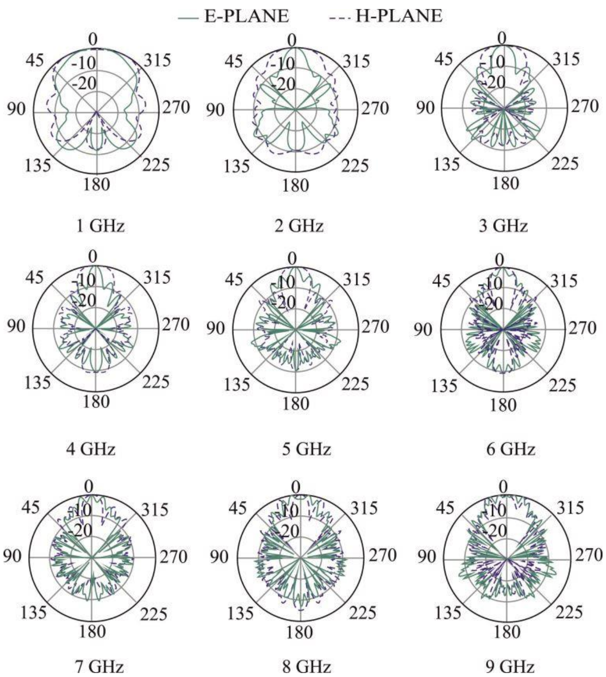

Fig. 9. Simulated (NEC-2) normalized Far-Field pattern of the designed antenna. Continued green line: E-plane and dashed blue line: H-plane.

It is well known as optimization techniques can often lead to solutions very sensitive to little variations both in manufacturing, deployment and/or hosting environments. Therefore, in order to test the robustness of the proposed antenna, we studied several random perturbations related both to manufacturing errors (random rotations and random lengths of the branches) and to the environment (random deformations due, for example, to the effect of the wind). In Fig. 10, three perturbed elements are shown: the first one is obtained by randomly modifying the wire length by adding or subtracting a quantity equal to 10% of the design value (Fig. 10 (a)); the second one is obtained by randomly modifying the wire orientation in the xz plane by clockwise or counterclockwise rotating the wire of an angle equal to 10% of the design value (Fig. 10 (b)); the last one is obtained by randomly modifying the wire orientation in the xy plane by clockwise or counterclockwise rotating the wire of an angle such that the y coordinate of the wire is equal to 10% of the total design length of the wire itself: i.e., $\phi_i = arctan(y_i = L_{i,})$, (Fig. 10 (c)). The first two perturbations are related to manufacturing errors and/or to deployment, while the last perturbation can model the effect of the wind. All the considered perturbations are very huge ones, since the design values have been varied of a significant quantity (10%). Nevertheless, both the simulated reflection coefficient and the simulated gain of all the perturbed configurations, shown in Figs. 11 and 12, respectively, confirm that the antenna is very robust to these huge perturbations (±10% with respect to the design value).

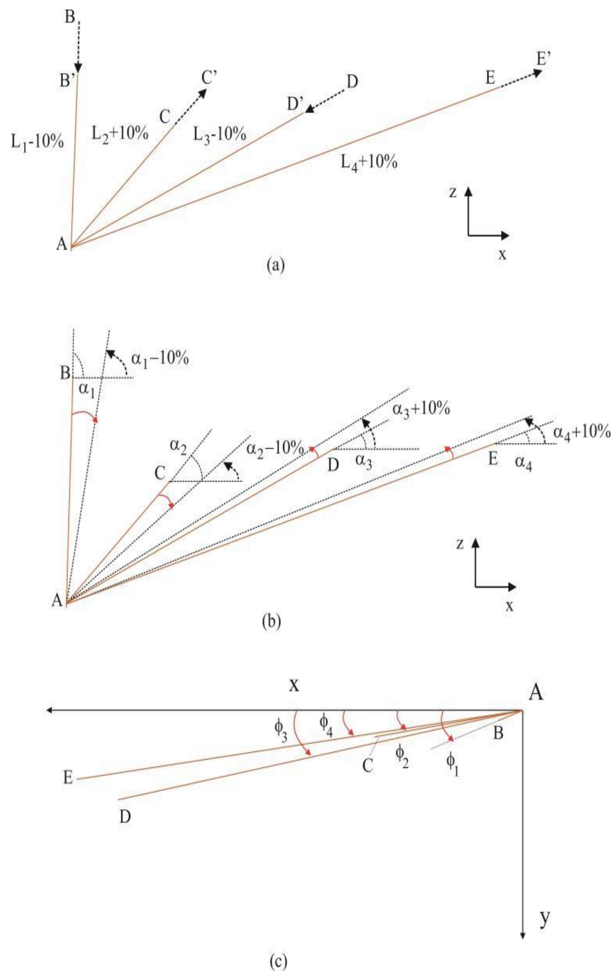

Fig. 10. Perturbed configurations of the designed antenna: (a) random length variations, (b) random rotations in the xz plane and (c) random rotations in the xy plane (ϕ_1=25°, ϕ_2=16°, ϕ_3=20°, ϕ_4=14°).

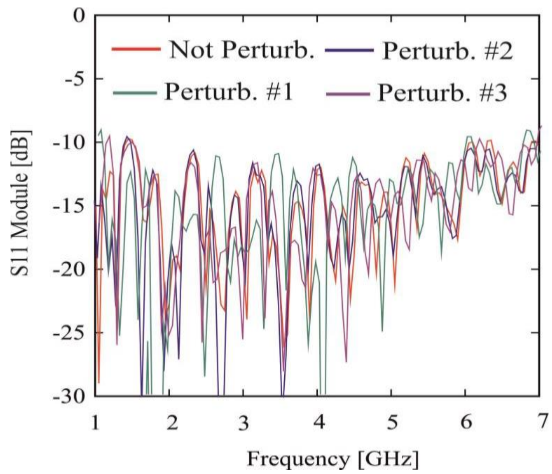

Fig. 11. Reflection coefficient of the perturbed configurations compared with the unperturbed antenna. Perturb #1: random length variations; perturb #2: random rotations in the xz plane; perturb #3: random rotations in the xy plane.

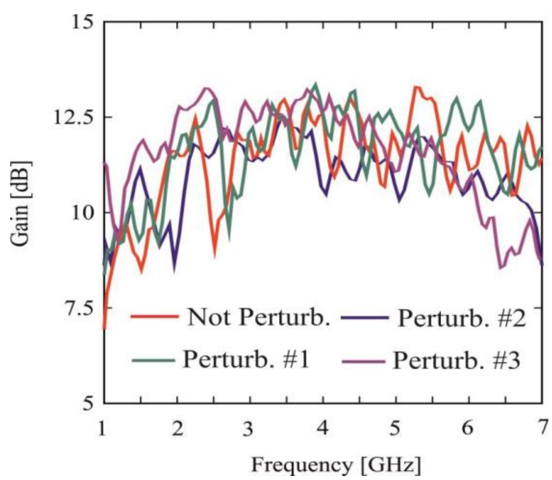

Fig. 12. Gain of the perturbed configurations compared with the unperturbed antenna. Perturb #1: random length variations; perturb #2: random rotations in the xz plane; perturb #3: random rotations in the xy plane.

V. CONCLUSION

In this work, the Structure-Based Evolutionary Design, an innovative antenna design technique based on evolutionary programming, has been used to design a wideband wire antenna for multi-band WLAN application, with an end-fire radiation pattern and a very simple geometry. The chosen fitness function includes far-field requirements, as well as wideband input matching specifications, which allow to stabilize the algorithm and to design both optimal and robust antennas. The designed antenna operates in a range from L to C frequency bands; therefore, covering the required frequencies for multi-band WLAN applications (2.4/5.2/5.8 GHz), showing a very good input matching and keeping an end-fire gain greater than 10 dB.

ACKNOWLEDGMENT

Maxia gratefully acknowledges Sardinia Regional Government for the financial support of his Ph.D. scholarship (P.O.R. Sardegna F.S.E. Operational Programme of the Autonomous Region of Sardinia, European Social Fund 2007-2013-Axis IV Human Resources, Objective l.3, Line of Activity l.3.1.).

Fanti gratefully acknowledges Sardinia Regional Government for the financial support of his Post Doc fellowship (P.O.R. Sardegna F.S.E. Operational Programme of the Autonomous Region of Sardinia, European Social Fund 2007-2013-Axis IV Human Resources, Objective l.3, Line of Activity l.3.1.).

REFERENCES

[1] J. H. Yoon and Y. C. Lee, "Modified bow-tie slot antenna for the 2.4/5.2/5.8 GHz WLAN bands with a rectangular tuning stub," *In Microw. Opt. Technol. Lett.*, vol. 53, RT no. 1, pp. 126-130, 2011.

[2] J. H. Lim, G. T. Back, Y. I. Ko, C. W. Song, and T. Y. Yun, "A reconfigurable PIFA using a switchable PIN-diode and a fine-tuning varactor for USPCS/WCDMA/m-WiMAX/ WLAN," *IEEE Trans. Antennas Propag.*, vol. 58, no. 7, pp. 2404-2411, July 2010.

[3] C. P. Chou, G. Y. Chen, J. S. Sun, and Y. Chen, "Wideband WLAN antenna design for PDA operation," *Proceedings of The 8th WSEAS International Conference on Applied Electromagnetics, Wireless and Optical Communications, ELECTRO '10*, pp. 29-32, 2010.

[4] R. E. Collin, "Antennas and radiowave propagation," *McGraw-Hill*, New York, 1986.

[5] H. J. Orchard, R. S. Elliott, and G. J. Stern, "Optimising the synthesis of shaped beam antenna patterns," *Microwaves, Antennas and Propagation, IEE Proceedings H*, vol. 132, 1985.

[6] G. A. Casula and G. Montisci, "Design of dielectric-covered planar arrays of longitudinal slots," *IEEE Antennas and Wireless Propagation Letters*, vol. 8, pp. 752-755, 2009.

[7] G. Montisci, G. Mazzarella, and G. A. Casula, "Effective analysis of a waveguide longitudinal

slot with cavity," *IEEE Trans. Antennas Propagation*, vol. 60, pp. 3104-3110, 2012.

[8] G. A. Casula, G. Mazzarella, and G. Montisci, "A truncated waveguide fed by a microstrip as radiating element for high performance automotive anti-collision radars," *International Journal of Antennas and Propagation*, 2012.

[9] S. Costanzo, G. A. Casula, A. Borgia, G. Montisci, I. Venneri, G. Di Massa, and G. Mazzarella, "Synthesis of slot arrays on integrated waveguides," *IEEE Antennas and Wireless Propagation Letters*, vol. 9, pp. 962-965, 2010.

[10] G. A. Casula, P. Maxia, G. Mazzarella, and G. Montisci, "Design of a printed log-periodic dipole array for ultra-wideband applications," *Progress In Electromagnetics Research C*, vol. 38, pp. 15-26, 2013.

[11] P. Maxia, G. A. Casula, G. Montisci, G. Mazzarella, and F. Gaudiomonte, "A printed LPDA fed by a coplanar waveguide for broadband applications," submitted to *IEEE Antennas and Wireless Propagation Letters*.

[12] R. Matias, "Characterization of a planar two-arm self-complementary square spiral antenna using the numerical electromagnetics code (NEC)," *27th Annual Review of Progress in Applied Computational Electromagnetics (ACES)*, pp. 630-635, Williamsburg, Virginia, March 2011.

[13] C. M. de J. van Coevorden, A. R. Bretones, M. F. Pantoja, S. G. Garcıa, and A. Monorchio, "A new implementation of the hybrid taguchi GA: application to the design of a miniaturized log-periodic thin-wire antenna," *Applied Computational Electromagnetics Society (ACES) Journal*, vol. 24, no. 1, pp. 21-31, February 2009.

[14] R. Mishra, R. Ghatak, and D. Poddar, "Design formula for sierpinski gasket pre-fractal planar-monopole antennas," *IEEE Antennas and Propagation Magazine*, vol. 50, issue 3, pp. 104-107, 2008.

[15] W. B. Wang, Q. Feng, D. Liu, "Application of chaotic particle swarm optimization algorithm to pattern synthesis of antenna arrays," *Progress In Electromagnetics Research*, vol. 115, pp. 173-189, 2011.

[16] G. A. Casula, G. Mazzarella, and N. Sirena, "Evolutionary design of wide-band parasitic dipole arrays," *IEEE Transactions on Antennas and Propagation*, vol. 59, pp. 4094-4102, 2011.

[17] G. A. Casula, G. Mazzarella, and G. Montisci, "Structure-based evolutionary programming design of broadband wire antennas," *International Journal of Antennas and Propagation*, 2013.

[18] L. Deias, G. Mazzarella, G. Montisci, and G. A. Casula, "Synthesis of artificial magnetic conductors using structure-based evolutionary design," *International Journal of Antennas and Propagation*, 2013.

[19] J. R. Koza, "Genetic programming: on the programming of computers by means of natural selection," *MIT Press*, 1992.

[20] C. Darwin, "The origin of species," *J. Murray*, London, chapter XIII, 1859.

[21] G. J. Burke and A. J. Poggio, "Numerical electromagnetics code-method of moments," *Tech. Rep. UCID-18834, Lawrence Livermore National Laboratory*, 1981.

[22] G. A. Casula, G. Mazzarella, and N. Sirena, "On the effect of the finite metal conductivity in the design of wire antennas using evolutionary design," *IEEE International Symposium on Antennas and Propagation (APSURSI)*, 2011.

Giovanni Andrea Casula received his Laurea degree (summa cum laude) in Electronic Engineering and his Ph.D. degree in Electronic Engineering and Computer Science from the University di Cagliari, Cagliari, Italy, in 2000 and 2004, respectively. Since March 2006, he is an Assistant Professor of Electromagnetic Field and Microwave Engineering in the Dipartimento di Ingegneria Elettrica ed Elettronica, University of Cagliari, teaching courses in electromagnetics and microwave engineering. His current research interests are in the field of synthesis, analysis and design of wire, patch and slot antennas. Casula is author or coauthor of about 26 papers in international journals, serves as reviewer for several international journals and is a member of the Italian Electromagnetic Society (SIEm).

Giorgio Montisci received his Laurea degree (summa cum laude) in Electronic Engineering and his Ph.D. degree in Electronic Engineering and Computer Science from the University of Cagliari, Cagliari, Italy, in 1997 and 2000, respectively. Since November 2000, he is Assistant Professor of Electromagnetic Field in the Dipartimento di Ingegneria Elettrica ed Elettronica, University of Cagliari, teaching courses in electromagnetics and microwave engineering. His research activity is mainly focused on analysis and design of waveguide slot arrays, microwave holographic techniques for the diagnostic of large reflector antennas, numerical methods in electromagnetics and printed antennas. He is author or coauthor of about 40 papers in international journals and Reviewer for EM Journals.

Alessandro Fanti received his Laurea degree in Electronic Engineering and his Ph.D. degree in Electronic Engineering and Computer Science from the

University of Cagliari, Cagliari, Italy, in 2006 and 2012, respectively. He currently holds a post-doc scholarship for design of microwave components. His research activity involves the use of numerical techniques for modes computation of guiding structures.

Paolo Maxia received his Laurea degree in Electronic Engineering from the University of Cagliari, Cagliari, Italy, in 2008 and since 2011 is a Ph.D. student in Electronic Engineering and Computer Science. His research activity involves the analysis, design and characterization of planar structures, such as printed antennas and passive microwave components.

Giuseppe Mazzarella graduated Summa with Laude in Electronic Engineering from the Università "Federico II" of Naples in 1984 and obtained his Ph.D. degree in Electronic Engineering and Computer Science in 1989. In 1990, he became Assistant Professor in the Dipartimento di Ingegneria Elettronica at the Università "Federico II" of Naples. Since 1992, he is with the Dipartimento di Ingegneria Elettrica ed Elettronica of the Università di Cagliari, first as Associate Professor and then, since 2000, as Full Professor, teaching courses in electromagnetics, microwave, antennas and remote sensing. His research activity has focused mainly on efficient synthesis of large arrays of slots, power synthesis of array factor, microwave holography techniques for the diagnostic of large reflector antennas and use of evolutionary programming for inverse problems solving. He is author (or co-author) of about 50 papers in international journals and is a Reviewer for many EM journals.

Compact UWB Antenna with Dual Functionality

Majid Shokri [1], Zhale Amiri [1], Mostafa Pilevari [2], Masoume Masoumi [3], Somayeh Asiaban [1], and Bal Virdee [4]

[1] Young Researchers and Elite Club
Islamic Azad University, Urmia Branch, Urmia, Iran
majed.shokri@gmail.com, zhale.amiri@gmail.com

[2] Department of Electrical Engineering
Islamic Azad University, Tehran Jonoob Branch, Tehran, Iran

[3] Department of Electrical Engineering
Islamic Azad University, Science and Research Branch, Urmia, Iran

[4] Faculty of Life Sciences and Computing
Center for Communications Technology, London Metropolitan University, London, UK
b.virdee@londonmet.ac.uk

Abstract **─** A novel Ultra-Wideband (UWB) monopole antenna is proposed that exhibits stop-band functionality at the WLAN frequency band. It consists of an annular ring shaped radiating patch that is excited with a 50 Ω feedline. The stop-band is generated by etching a parasitic ring on the reverse side of the antenna's substrate. The antenna's impedance bandwidth was enhanced by including a semi-circular notch in the trapezoidal shaped ground-plane in the vicinity of the parasitic ring. The measured results confirm the impedance bandwidth covers a frequency range between 2.42-11.4 GHz for VSWR≤2, which corresponds to a fractional bandwidth of 130%. The UWB antenna is omni-directional in the xz-plane and approximately bi-directional in the yz-plane. The antenna is compact in size with overall dimensions of 30×30×1.6 mm^3.

Index Terms **─** Band-notched antenna, microstrip fed antenna, monopole antenna, ultra-wideband and WLAN.

I. INTRODUCTION

High data rate wireless communications technology is developing rapidly since the release of the Ultra-Wideband (UWB) frequency range by the Federal Communications Commission (FCC) [1]. As in the case of conventional narrowband wireless systems, antennas play a crucial role in UWB systems. However, the design of antennas for UWB systems is more challenging as they need to operate over a bandwidth of 7.5 GHz from 3.1 GHz to 10.6 and at the same time satisfactorily, radiating energy over the entire UWB frequency range. For this, application printed monopole antennas are attractive as they provide the following features:

(i) Large impedance bandwidth.
(ii) Ease of fabrication using conventional microwave integrated circuit technology.
(iii) Ease of fabrication using conventional microwave integrated circuit technology and possessing acceptable radiation characteristics [2]-[4].

Within the UWB spectrum coexists other narrowband systems including WLAN (5.15-5.35 GHz and 5.725-5.825 GHz). As these systems operate using a significantly stronger power density than UWB systems, they are therefore likely to fatally interfere with the operation of UWB systems. This necessitates an additional function from UWB systems to suppress such interfering signals. The conventional solution to

Submitted On: February 16, 2013
Accepted On: July 25, 2014

eliminate or suppress the interfering signal, is by using a band reject filter in the front-end of the UWB system. However, since the filter is wavelength dependent, it will result in an increase of the physical size of the UWB system. To overcome this issue, UWB antenna with a band rejected function is required. UWB antennas with notch bands have been proposed using various techniques, some of which include using H-shaped conductor-backed plane [5], cutting two modified U-shaped slots on the patch [6], inserting two rod-shaped parasitic structures [7], embedding resonant cell in the microstrip feed-line [8], using a fractal tuning stub [9], utilizing a resonant patch [10] and using a MAM and genetic algorithm [11]. In [12] and [13], different configuration slots are shown to provide band-notched property at the WLAN band.

In [14], band-stop function is achieved by using a T-shaped coupled-parasitic element in the ground-plane. In [15]-[19], it is shown that one slot or parasitic element is sufficient to create a stop-band; however, this is contrary to [20] and [21], where multiple identical elements are employed to generate a single notch band in radiators. The shortcoming of these notch antennas is that the notch band is either shorter or wider than the bandwidth of the interference signal. This means that the interfering signal is either partially suppressed or completely suppressed along with some of the desired signal.

In [22], it is shown that excellent bandwidth performance can be achieved with a monopole circular patch antenna with a circular-shaped ring, used as a parasitic element and a slit in the ground-plane. However, this structure lacks in band-stop functionality. In [23], a printed monopole antenna is proposed using a circular patch enclosed in annular ring, to provide ultra-wide bandwidth coverage. However, the antenna's azimuthal radiation pattern is approximately omni-directional and in the elevation plane it resembles a figure eight. The antenna however exhibits nulls in the radiating patterns, which exceed 10 dB resulting from surface current variations with frequency. This antenna also lacks in band-stop functionality. A planar modified circular ring antenna for ultra-wideband applications with band notch performance was reported in [24]. It has a return-loss of 10 dB over the frequency range 3.1-10.6 GHz, except at the notch frequency band. The band-notched characteristic is achieved by introducing a tuning stub inside the ring monopole. The annular ring is mounted vertically on a circular ground-plane.

The structure is relatively complex to fabricate and its radiation pattern is essentially unidirectional.

In this paper, a UWB antenna is presented possessing a band-notch function. The antenna uses a patch consisting of an annular ring and etched on the reverse side of the same substrate is a parasitic ring element that determines the exact frequency of the notch-band. Unlike [22] and [23], the proposed antenna exhibits a band-notch function to eliminate interfering WLAN signals. Unlike [23], its radiation pattern is approximately omni-directional in both azimuthal and elevation planes. The proposed antenna is also much less complicated to fabricate than [24]. The structure of the proposed antenna was optimized using an available EM simulation tool and the antenna fabricated to verify its performance.

II. ANTENNA STRUCTURE

The proposed monopole antenna is composed of an annular ring which is fed through a 50 Ω microstrip line, whose width is 2.8 mm, as shown in Fig. 1. Etched on the reverse side of the same dielectric substrate and immediately behind the annular ring is a parasitic ring. Dimensions of the parasitic element determine the frequency of the notch band (i.e., 5-6 GHz). The ground-plane resembles the shape of a trapezoid to enhance the antenna's impedance bandwidth.

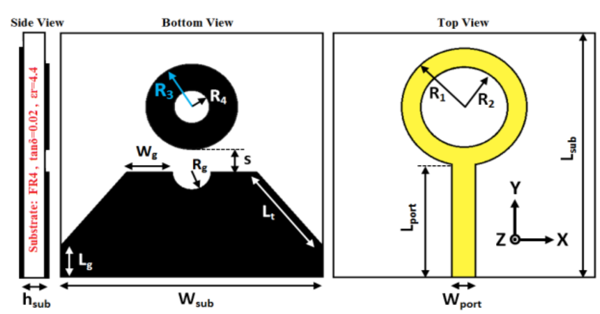

Fig. 1. Geometry of the proposed antenna.

The upper part of the ground-plane is defected with a semi-circular notch next to the annular ring, to further improve the impedance bandwidth. The antenna was fabricated on a low-cost commercially available substrate FR-4 with relative permittivity of 4.4, tanδ=0.02 and thickness of 1.6 mm. The antenna design is terminated with a 50 Ω SMA connector for signal reception/transmission. The optimal dimensions of the antenna, defined in Fig. 1, are given in Table 1.

Table 1: Optimized antenna dimensions (unit: mm)

W_{sub}=30	R_1=7.2	L_t=11.7
L_{sub}=30	R_2=5	L_g=4
h_{sub}=1.6	R_3=5.3	W_g=5.3
W_{port}=2.78	R_4=2	R_g=2.2
L_{port}=13.9	S=2.5	

Figure 2 shows the four steps undertaken to realise the antenna. The first step includes only a circular radiating patch and a rectangular ground-plane; in the second step the ground-plane is defected with a semi-circular notch in the vicinity of the circular patch; in the third step the circular patch is converted to an annular ring and the ground-plane is tapered; in the final step a parasitic ring is added in the ground-plane and the ring is placed directly below the annular ring patch. Figure 2 shows the changes in the VSWR and return-loss performance for the various modifications made to realise the antenna. The proposed antenna corresponding to the final step, exhibits an ultra-wideband impedance bandwidth between 3.06-12 GHz for VSWR≤2 and a band notch function that cover the WLAN band. The insertion of the parasitic ring creates a narrow band notch between approximately 5-6 GHz. This phenomenon can be understood using the Smith chart, plotted in Fig. 3. Embedding the parasitic element leads to capacitance enhancement between the parasitic element and the patch; thus, saving energy instead of propagating it to hence realize a stop band [25].

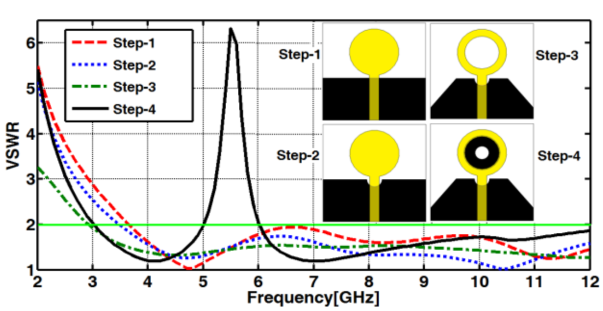

(a)

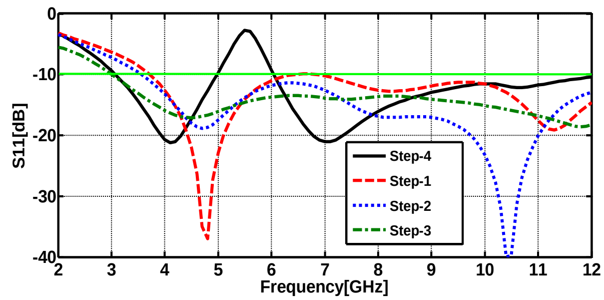

(b)

Fig. 2. (a) Simulated VSWR and (b) S11 characteristics for four steps used to create the proposed antenna structure.

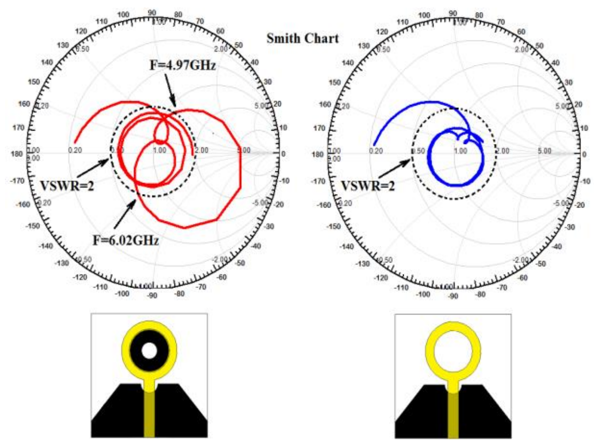

Fig. 3. Smith chart for the proposed antenna and antenna without parasitic element.

Finally, about the ground plane, it’s understood that the radius of the semi-circular notch in the ground plane is important as it affects the impedance match of the antenna.

III. SIMULATION RESULTS AND MEASUREMENTS

In this section, the affect of the various antenna parameters on the performance of the band notched UWB antenna is investigated. Numerical and experimental results of the impedance bandwidth and radiation characteristics are presented and discussed. The parameters of the proposed antenna were studied by changing them systematically one at a time, while keeping all other parameters fixed.

Full-wave electromagnetic analysis was performed on the proposed antenna using Ansoft HFSS (ver 11.1) software.

As mentioned earlier, the band rejection property in the proposed antenna is achieved by printing a parasitic element in the shape of a ring on the reverse side of the substrate, which located immediately below the annular ring shaped patch. The operating frequency of the antenna and the bandwidth of the rejection band were achieved by carefully tuning the dimensions of the annular ring and the parasitic ring, respectively. From this study, it was found that the parasitic element behaves as resonator that is coupled with the annular ring to create a resonance band-stop function at f_r is given by [26]:

$$f_r = \frac{c}{2\pi R_3 \sqrt{\varepsilon_{eff}}} \tag{1}$$

That $2\pi R3$ is the outer circumference of the parasitic ring, ε_{eff} is the effective dielectric constant and c is the speed of light. Figure 4 shows the antenna's impedance bandwidth can be adjusted by varying the outer radius of the annular ring (R_1), which has a marginal effect on the center frequency of the notch and bandwidth. The outer radius (R_3) of the parasitic element significantly affects the center frequency of the notch, as shown in Fig. 5. The change in notch frequency is approximately 1 GHz for radius change from 5-6 mm. The ground-plane notch radius (R_g) affects the impedance bandwidth of the antenna, as shown in Fig. 6, as well as the VSWR magnitude of the notch. Analysis shows the inner radius (R_2) of patch and the gap (S) between the parasitic element and ground-plane play an important role in determining the sharpness and width of the stop-band response. Figure 7 shows the measured radiation patterns of the proposed antenna (co-polarization and cross-polarization) in the H-plane (x-z plane) and E-plane (y-z plane). It can be observed from this result that the radiation patterns in x-z and y-z plane are nearly omni-directional and bi-directional, respectively, at the frequencies of 5 GHz and 6.9 GHz. The measured and simulated gain of the proposed antenna over the antenna's operating bandwidth is shown in Fig. 8. The graph shows that the measured gain varies between 1.7-3.9 dBi, except in the notch band between 5-6 GHz where the signal is attenuated. The current density distribution over the proposed antenna at the center frequency of the notch (i.e., 5.5 GHz) is shown in Fig. 9. The current density is concentrated over the feedline, the ground-plane below the feedline and the parasitic ring. The current emanating from the parasitic element is in the opposite direction to the current flow in the patch. Photograph of the UWB antenna is shown in Fig. 10.

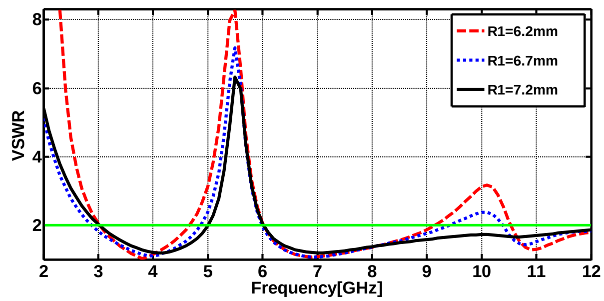

Fig. 4. Simulated VSWR response of the proposed UWB antenna as a function of annular ring's outer radius (R_1).

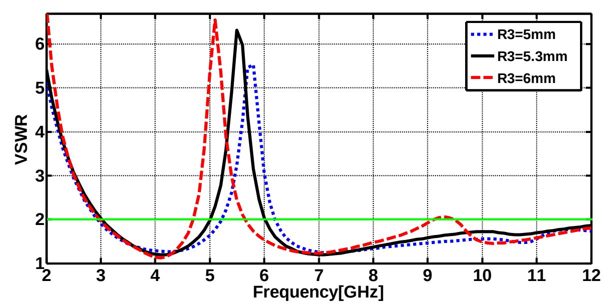

Fig. 5. Simulated VSWR characteristics of the proposed UWB antenna as a function of outer radius of the parasitic element (R_3).

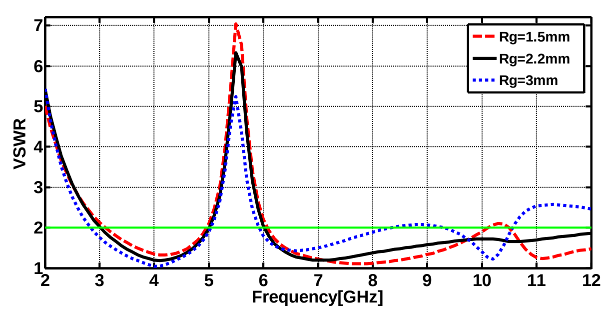

Fig. 6. Simulated VSWR response of the proposed UWB antenna as a function of ground-plane notch radius (R_g).

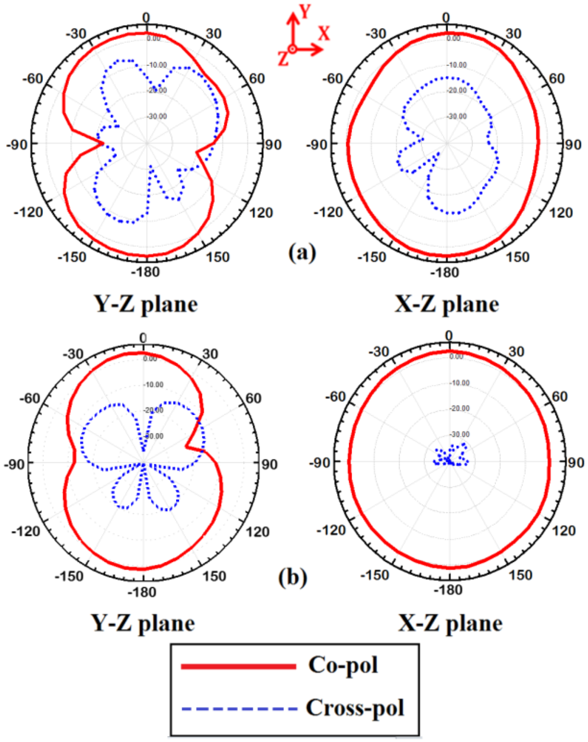

Fig. 7. Measured radiation patterns of the proposed antenna at: (a) 5 GHz and (b) 6.9 GHz.

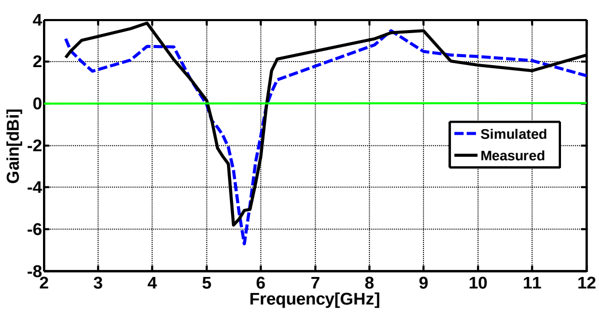

Fig. 8. Measured and simulated gain of the proposed antenna.

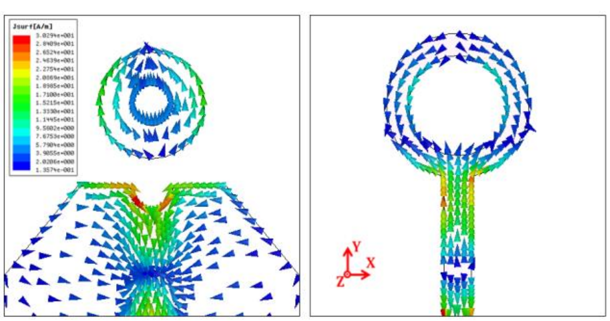

Fig. 9. Surface current distribution over the proposed antenna at 5.5 GHz.

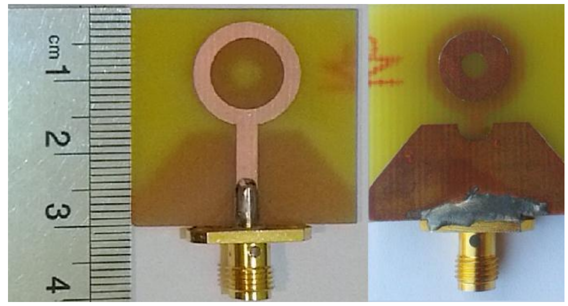

Fig. 10. Photograph of the fabricated antenna.

The measured and simulated reflection-coefficient of the proposed antenna that depicted in Fig. 11 not only verifies its performance up to12 GHz, but also shows a close correspondence between the measured and simulated curves.

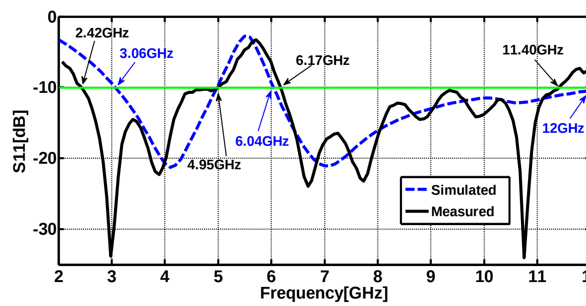

Fig. 11. Measured and simulated return-loss of the proposed antenna.

IV. CONCLUSION

A dual function monopole antenna is reported for UWB applications. The antenna has inherent band-notch characteristic necessary to filter out WLAN interference signals. The proposed antenna has advantages of low-cost, compact size and ease of fabrication. The measured results verify its excellent UWB response (2.42-11.4 GHz) with a prescribed WLAN rejection band and good radiation patterns across the entire UWB spectrum. These characteristics make the antenna a viable good candidate for UWB wireless applications.

REFERENCES

[1] *Federal Communications Commission*: "First report and order, revision of part 15 of the communication's rules regarding ultra-wideband transmission system," 2002.

[2] M. Ojaroudi, C. Ghobadi, and J. Nourinia, "Small square monopole antenna with inverted t-shaped

notch in the ground plane for UWB application," *IEEE Antennas Wireless Propag. Lett.*, vol. 8, pp. 728-731, 2009.

[3] J. Pourahmadazar, C. Ghobadi, J. Nourinia, and H. Shirzad, "Multiband ring fractal monopole antenna for mobile devices," *IEEE Ant. Wireless Propag. Lett.*, vol. 9, 2010.

[4] N. Ojaroudi, S. Amiri, F. Geran, and M. Ojaroudi, "Band-notched small monopole antenna using triple e-shaped structures for UWB systems," *Applied Computational Electromagnetics Society (ACES) Journal*, vol. 27, no. 12, pp. 1022-1028, December 2012.

[5] R. Zaker, C. Ghobadi, and J. Nourinia, "Novel modified UWB planar monopole antenna with variable frequency band-notch function," *IEEE Antennas Wireless Propag. Lett.*, vol. 7, pp. 112-114, 2008.

[6] M. Ojaroudi, G. Ghanbari, N. Ojaroudi, and C. Ghobadi, "Small square monopole antenna for UWB application with variable frequency band-notch function," *IEEE Antennas Wireless Propag. Lett.*, vol. 8, pp. 1061-1064, 2009.

[7] M. Rostamzadeh, S. Mohamadi, J. Nourinia, C. Ghobadi, and M. Ojaroudi, "Square monopole antenna for UWB applications with novel rod-shaped parasitic structures and novel v-shaped slots in the ground plane," *IEEE Antennas and Wireless Propagation Letters*, vol. 11, 2012.

[8] S. W. Qu, J. L. Li, and Q. Xue, "A band-notched ultra-wideband printed monopole antenna," *IEEE Antennas Wireless Propag. Lett.*, vol. 5, pp. 495-498, 2006.

[9] W. J. Lui, C. H. Cheng, Y. Cheng, and H. Zhu, "Frequency notched ultra-wideband microstrip slot antenna with fractal tuning stub," *Electron. Lett.*, vol. 41, no. 6, pp. 294-296, March 2005.

[10] K. G. Thomas and M. A. Sreenivasan, "A simple ultra-wideband planar rectangular printed antenna with band dispensation," *IEEE Trans. Antennas Propag.*, vol. 58, no. 1, pp. 2734, January 2010.

[11] J. Pourahmadazar, H. Shirzad, C. Ghobadi, and J. Nourinia, "Using a MAM and genetic algorithm to optimize UWB microstrip monopole antenna with FEM and HFSS," *5th International Symposium on Telecommunications*, 2010.

[12] S. Yazdanifard, R. A. Sadeghzadeh, and M. Ojaroudi, "Ultra-wideband small square monopole antenna with variable frequency band-notch function," *Prog. Electromagn. Res. C*, vol. 15, pp. 133-144, 2010.

[13] M. Ojaroudi, "Printed monopole antenna with a novel band-notched folded trapezoid ultra-wideband," *J. Electromagn. Waves Appl.*, vol. 23, pp. 2513-2522, 2009.

[14] R. Rouhi, C. Ghobadi, J. Nourinia, and M. Ojaroudi, "Ultra-wideband small square monopole antenna with band notched function," *Microw. Opt. Technol. Lett.*, vol. 52, no. 9, pp. 2065-2069, September 2010.

[15] K. L. Wong, Y. W. Chi, C. M. Su, and F. S. Chang, "Band-notched ultra-wideband circular-disk monopole antenna with an arc-shaped slot," *Microw. Opt. Technol. Lett.*, vol. 45, no. 3, pp. 188-191, May 2005.

[16] Y. J. Cho, K. H. Kim, D. H. Choi, S. S. Lee, and S. O. Park, "A miniature UWB planar monopole antenna with 5-GHz band-rejection filter and the time-domain characteristics," *IEEE Trans. Antennas Propag.*, vol. 54, no. 5, pp. 1453-1460, May 2006.

[17] L. Peng, C. L. Ruan, and X. C. Yin, "Analysis of the small slot-loaded elliptical patch antenna with a band-notched for UWB applications," *Microw. Opt. Technol. Lett.*, vol. 51, no. 4, pp. 973-976, April 2009.

[18] K. H. Kim and S. O. Park, "Analysis of the small band-rejected antenna with the parasitic strip for UWB," *IEEE Trans. Antennas Propag.*, vol. 54, no. 6, pp. 1688-1692, June 2006.

[19] L. Peng, C. L. Ruan, Y. L. Chen, and G. M. Zhang, "A novel bandnotched elliptical ring monopole antenna with a coplanar parasitic elliptical patch for UWB applications," *J. Electromagn. Waves Appl.*, vol. 22, no. 4, pp. 517-528, April 2008.

[20] Y. D. Dong, W. Hong, Z. Q. Kuai, and J. X. Chen, "Analysis of planar ultra wideband antennas with on-ground slot band-notched structures," *IEEE Trans. Antennas Propag.*, vol. 57, no. 7, pp. 1886-1893, July 2009.

[21] A. M. Abbosh and M. E. Bialkowski, "Design of UWB planar band-notched antenna using parasitic elements," *IEEE Trans. Antennas Propag.*, vol. 57, no. 3, pp. 796-799, March 2009.

[22] B. A. L. da Silva and A. G. D'Assuncao, "Analysis of monopole antennas for UWB systems with circular ring patch and parasitic element," *IEEE Conference on Electromagnetic Field Computation (CEFC)*, p. 1, 2010.

[23] K. P. Ray and S. S. Thakur, "Printed annular ring with circular patch monopole UWB antenna," *International Conference on Advances in Computing and Communications*, pp. 270-273, 2012.

[24] S. Ghosh, "Band-notched modified circular ring monopole antenna for ultrawideband applications," *IEEE Antennas and Wireless Propagation Letters*, vol. 9, pp. 276-279, 2010.

[25] M. Shokri, H. Shirzad, S. Movagharnia, B. Virdee, Z. Amiri, and S. Asiaban, "Planar monopole

antenna with dual interference suppression functionality," *IEEE Antennas and Wireless Propagation Letters*, vol. 12, pp. 1554-1557, 2013.
[26] L. H. Hsieh and K. Chang, "Equivalent lumped elements g, l, c, and unloaded q's of closed and open-loop ring resonators," *IEEE Trans. on Microwave Theory and Techniques*, vol. 50, pp. 453-460, 2002.

Majid Shokri was born in February 1979 in Iran. He received his B.Sc. and M.Sc. degrees from the Urmia Branch, IAU and Urmia University in 2001 and 2012, respectively; all in Electrical Engineering.

Zhale Amiri was born in January 1981 in Iran. She received her B.Sc. degree from Urmia Branch, IAU in Electrical Engineering in 2005.

Mostafa Pilevari was born in 1980 in Iran. He received his B.Sc. and M.Sc. degrees from the Urmia Branch, IAU and Tehran Jonoub Branch, IAU in 2004 and 2008, respectively; all in Electrical Engineering.

Masoume Masoumi was born on December 25, 1984 in Iran. She received her B.Sc. degree in Electrical and Telecommunication Engineering from Azad University of Bushehr, Iran and M.Sc. degree in Electrical and Telecommunication Engineering from Azad University of Urmia, Iran. Her primary research interest is in broadband antenna design.

Somayeh Asiaban was born in September 1984 in Iran. She received her B.Sc. degree from Urmia Branch, IAU in Electrical Engineering in 2008.

Bal Virdee is a Professor of Microwave Communications Technology in the Faculty of Life Sciences and Computing at London Metropolitan University, where he Heads the Center for Communications Technology and is the Director of London Metropolitan Microwaves.

A Simple Coupled-Line Wilkinson Power Divider for Arbitrary Complex Input and Output Terminated Impedances

Yongle Wu [1,2], Jiuchao Li [1], and Yuanan Liu [1]

[1] School of Electronic Engineering
Beijing University of Posts and Telecommunications, P.O. Box 171, Beijing 100876, China
wuyongle138@gmail.com, lijiuchao@gmail.com, yuliu@bupt.edu.cn

[2] The State Key Laboratory of Millimeter Waves
Southeast University, Nanjing 210096, China

Abstract **─** A simple and analytical design methodology for a novel coupled-line power divider with arbitrary complex terminated impedances is proposed in this paper. Because of the usage of a single-section coupled line, the additional odd-mode characteristic impedance increases the design degree of freedom and makes the isolation structure still use a single resistor when terminated impedances are extended from real values (such as 50 Ohm) to arbitrary complex values. To design this generalized coupled-line power divider, the electrical parameters including electrical lengths and characteristic impedances can be redesigned by the provided closed-form mathematical expressions when complex terminated impedances are known. The validity of this given design methodology has been confirmed by simulation and measurement of two typical microstrip examples.

Index Terms **─** Arbitrary complex terminated impedances, coupled line and power divider.

I. INTRODUCTION

Conventional Wilkinson power dividers [1] can be applied to split the input signal into two ones with the same amplitude and phase. Also, these power dividers can be used to combine two of the same signals into a single one as combiners. Many efforts have been made to enhance its performance, such as ultra-wideband power divider [2], dual-band and optional isolation power dividers using parallel strip line and open stubs [3,4], compact coupled-line and stepped-impedance transmission lines dual-band Wilkinson power dividers [5-10] and multi-way dual-band planar power dividers[11-14].

Obviously, typical hybrid Wilkinson power dividers are terminated with a constant real-value resistances. To extend the terminated impedances, three-port equal power dividers terminated in different impedances are proposed by Ahn in [15]. As a more generalized case, a novel CAD algorithm for the design of multi-section power dividers terminated in complex frequency-dependent impedances has been developed by Rosloniec in [16]. However, the given power dividers in [15] are only suitable for different terminated resistances, while the rigorous closed-form design equations are not provided in [16]. Moreover, the coupled-line section is not considered in the design of the power dividers in [15] and [16]. In addition, to reduce the circuit size and provide more freedom of design parameters, the coupled-line sections are used in the design of power dividers in [17]; but three terminated impedances of the coupled-line power dividers in [17] are equal to the same constant resistance. The dual-band power divider two-section cascaded coupled-line structure in [18], but has small frequency-ratio limitation, in succession, frequency-ratio limitation of the dual-band divider is improved in [19]. It is necessary to point out that these coupled-line power dividers in [18] and [19] are special cases of structures in [9]. Although, several Wilkinson power dividers with harmonics suppression or for multi-frequency applications are researched in [20-22], the

Submitted On: April 3, 2013
Accepted On: July 25, 2014

complex input and output terminated impedances are not considered.

In this paper, a novel coupled-line power divider with arbitrary complex terminated impedances is proposed, since the complex terminated or equivalent impedances are common in antennas and power amplifiers. Different from the previous coupled-line power divider in [17], these terminated impedances in this paper are extended from real values (such as 50 Ohm) to arbitrary complex values. By using even-mode and odd-mode analysis, a simple and analytical design equations are obtained. Once the complex terminated impedances are known, the even-mode (and odd-mode) characteristic impedances and electrical lengths can be determined uniquely. The design parameters of typical examples for complex impedances are presented. Finally, the given design approach is validated by two fabricated microstrip power dividers with different complex terminated impedances.

II. THE PROPOSED CIRCUIT AND DESIGN APPROACH

The circuit configuration of the proposed coupled-line Wilkinson power divider for complex terminated impedances is shown in Fig. 1. The input-port impedance is $Z_S = R_S + jX_S$ and the matched output-port impedance is $Z_L = R_L + jX_L$. Although, two terminated impedances are complex, the isolation structure only includes a single resistor with the defined parameter R_W. This is because a coupled-line section is used as main impedance matching circuit. The even-mode and odd-mode characteristic impedances are defined as Z_e and Z_o, respectively. Due to match two complex impedances, the electrical length θ of the coupled-line section will not always be 90 degrees, which is determined by given terminated impedances.

When even-mode analysis is considered, the circuit configuration shown in Fig. 1 can be simplified as the equivalent circuit shown in Fig. 2 (a). The input-port impedance Z_S is doubled, while the odd-mode characteristic impedance Z_o and the isolation resistor R_W are neglected. This kind of impedance transformer has been analyzed in [23-25]. Now, we can reconsider the circuit shown in Fig. 2 (a) when different parameters definition is used. The design equations can be written as:

$$Z_e = \sqrt{2R_S R_L + \frac{(4X_S^2 R_L - 2X_L^2 R_S)}{2R_S - R_L}}, \tag{1}$$

$$\theta = \mathrm{atan}[\frac{Z_e(2R_S - R_L)}{2R_S X_L - 2R_L X_S}]. \tag{2}$$

Note, that even-mode characteristic impedance Z_e should be real positive values. This limits the applicable scope of complex terminated impedances. However, the value of the electrical length θ can be real negative; we can obtain the final available values according to the equation $\theta' = \theta + n\pi, (n = 0, \pm 1, \pm 2, ...)$.

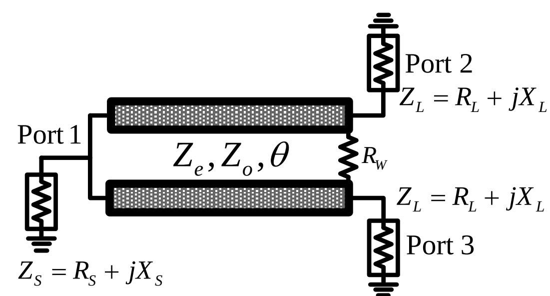

Fig. 1. The circuit configuration of the proposed coupled-line Wilkinson power divider for complex terminated impedances

Next, the odd-mode analysis is considered. The simplified circuit is shown in Fig. 2 (b). Different from the conventional Wilkinson power divider, the odd-mode characteristic impedance Z_o provides a free variable in the design of perfect output-port matching and isolation between them. Therefore, although the terminated impedance Z_L is complex value, the ideal output-port matching and isolation can be easily achieved by modifying Z_o and R_W. The accurate design mathematical expressions are:

$$Z_o = \frac{-(R_L^2 + X_L^2)}{X_L \tan(\theta)}, \tag{3}$$

$$R_W = \frac{2(R_L^2 + X_L^2)}{R_L}. \tag{4}$$

According to the above equations (1)-(4), we can calculate the electrical parameters of this coupled-line Wilkinson power divider with complex terminated impedances. As shown in Fig. 2 (a), the even-mode characteristic impedance Z_e and electrical length θ affect the input-port matching and transmission performance. As shown in Fig. 2 (b), the perfect isolation performance is obtained by varying the odd-mode characteristic impedance Z_o and the isolation resistor R_W.

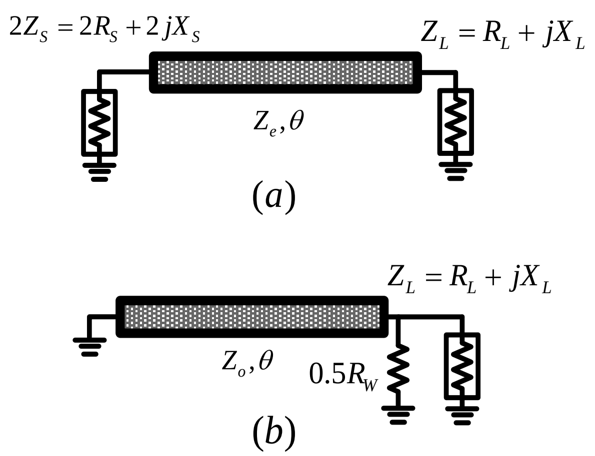

Fig. 2. The equivalent simplified circuits under: (a) even-mode and (b) odd-mode excitations.

In order to explain the applicable scope of the complex terminated impedances, Fig. 3 shows two types of parameter curves for different terminated impedances. The first case has an input-port impedance of $55 - j45\,(\Omega)$ and an output-port resistance of $40\,(\Omega)$, as shown in Fig. 3 (a). The second case has an input-port impedance of $45 - j40\,(\Omega)$ and an output-port resistance of $38\,(\Omega)$, as shown in Fig. 3 (b). The output-port inductance $X_L\,(\Omega)$ of these two cases changes from -25 to -10. Both for Figs. 3(a) and (b), when output-port inductance X_L increases, the characteristic impedances Z_e and Z_o increase, while the electrical length θ and the resistor R_W decrease. There are three main features for available parameters in Figs. 3 (a) and (b): (1) $Z_e \geq Z_o > 0$, (2) $R_W > 0$ and (3) $\theta > 0$.

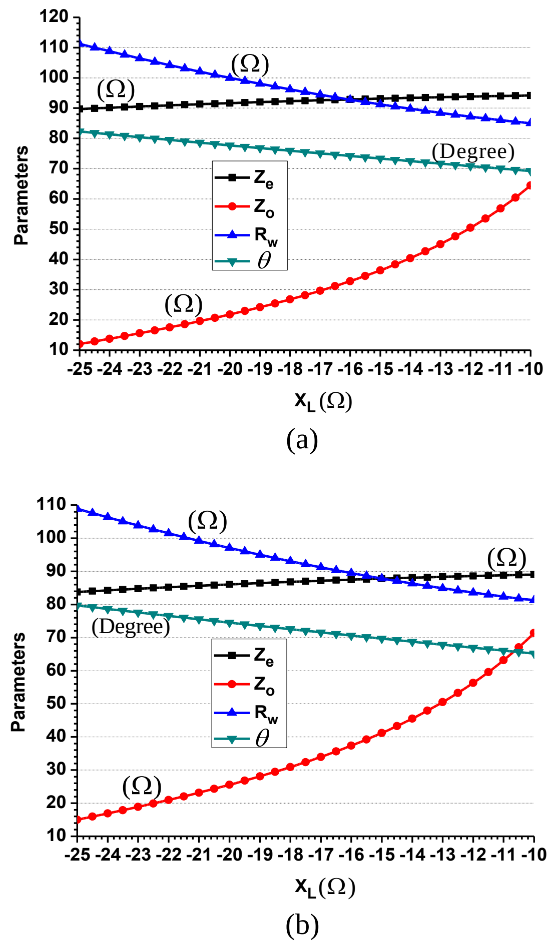

Fig. 3. The design parameters of typical examples for complex impedances: (a) $Z_S = 55 - j45, R_L = 40$ and (b) $Z_S = 45 - j40, R_L = 38$.

III. EXAMPLES

To verify our proposed idea experimentally, two typical examples are designed, fabricated and measured. The Rogers R04350B substrate with a relative dielectric constant of 3.48 and a thickness of 0.762 mm is used in these examples. The first power divider (A) is terminated in input-port impedance of $55 - j40\,(\Omega)$ and output-port impedance of $40 - j10\,(\Omega)$. The calculated electrical parameters of power divider A are $Z_e = 88.8819\,(\Omega)$, $Z_o = 57.3795\,(\Omega)$, $R_W = 85\,(\Omega)$ and $\theta = 71.3491\,(\text{Deg.})$. The second power divider (B) is terminated in input-port impedance of $75 + j40\,(\Omega)$ and output-port impedance of $50 + j10\,(\Omega)$. The calculated electrical parameters of power divider B are $Z_e = 102.7132\,(\Omega)$, $Z_o = 63.2830\,(\Omega)$, $R_W = 104\,(\Omega)$ and $\theta = 103.6796\,(\text{Deg.})$. In addition, the operating center frequency of the power divider A (B) is 2.1 (2) GHz. The accurate physical dimension values (unit: mm) of the power divider A (B) shown in Fig. 4 are $w_p = 1.72(1.72)$, $w_S = 0.46(0.43)$, $w_L = 0.85(0.65)$, $L_1 = L_2 = 8(8)$ and $L_3 = 17.14(26.14)$. The simulation is based on lossless coupled-line models and ideal resistors. The measurement of the power dividers A and B is accomplished by using Agilent N5230A network analyzer. The three-port extension about 7.5 mm physical-length 50-Ohm transmission line is used to obtain the desired scattering parameters. Figure 5 shows the simulated and measured results of the power dividers A and B. In details, the measured center frequency of the power divider A (B) is about 2.1 (2.01) GHz. When the ports matching and isolation are considered in the constant complex terminated impedances, the measured -20 dB fractional bandwidth of the power divider A is about 16 % (from 1.95 to 2.29 GHz), while the similar fractional bandwidth of the power divider B is also about 16% (from 1.85 to 2.17 GHz).

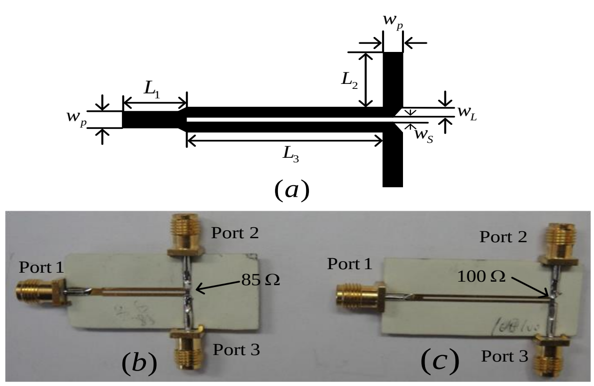

Fig. 4. (a) The physical definition of the proposed power divider; the photograph of the fabricated microstrip power dividers: (b) A and (c) B.

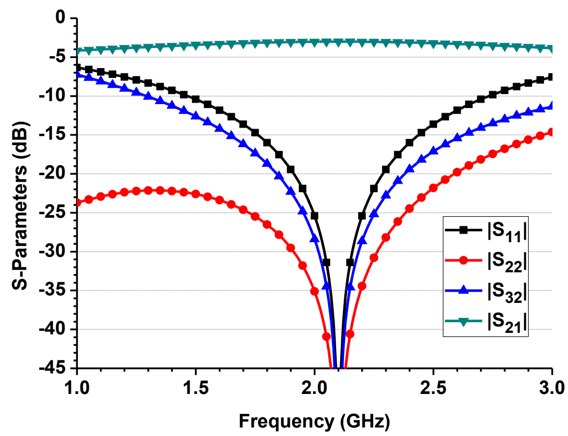

(a1)

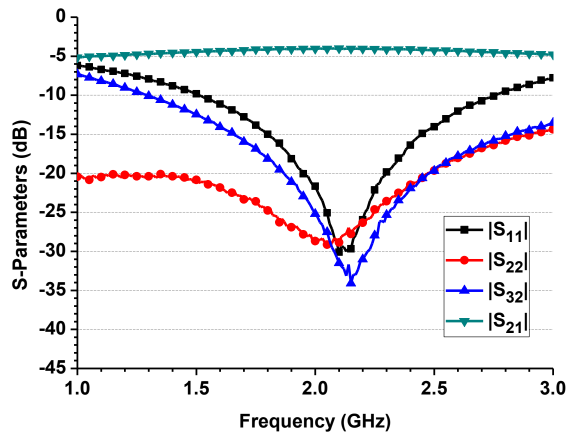

(a2)

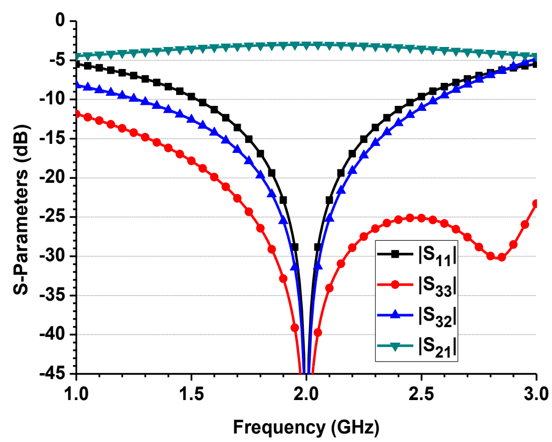

(b1)

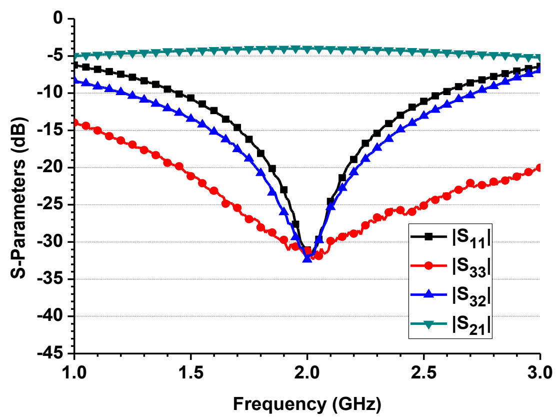

(b2)

Fig. 5. The simulated (a1, b1) and measured (a2, b2) results of the fabricated power divider A (a1, a2) and B (b1, b2).

In general, there is good agreement between the measured and simulated results. Finally, to compare with previous published power dividers, a simple performance comparison is given in Table 1.

Table 1: Performance comparison of this proposed coupled-line power divider with the previous ones

Type	Terminated Impedances	Coupled Line	Design Method	Matching and Isolation
[1]	$Z_0(50\ \Omega)$	No	Simple	Yes
[15]	Arbitrary real	No	Complicated	No
[16]	Complex	No	Complicated	No
[17]	$Z_0(50\ \Omega)$	Yes	Simple	Yes
This work	Arbitrary complex	Yes	Simple and analytical	Yes

IV. CONCLUSION

A novel coupled-line power divider is proposed to satisfy arbitrary complex terminated impedances in this paper. The achieved design approach is analytical and simple. The design parameters of typical examples for complex impedances are illustrated. Furthermore, all the design mathematical expressions are confirmed by the simulation and measurement of two typical examples. Obviously, this proposed power divider not only has small size but also satisfies flexible input and output complex terminated impedances. It is believed that this design approach could be useful in the design of antenna arrays and power amplifiers with complex input impedances.

ACKNOWLEDGMENT

This work was supported in part by National Natural Science Foundation of China (No. 61201027), National Basic Research Program of China (973 Program) (No. 2014CB339900), Open Project of the State Key Laboratory of Millimeter Waves (Grant No. K201316), BUPT Excellent Ph.D. Students Foundation (CX201214) and Beijing Key Laboratory of Work Safety Intelligent Monitoring (Beijing University of Posts and Telecommunications). In addition, the corresponding Chinese patent (No. 201310017148.1) has been pending.

REFERENCES

[1] E. Wilkinson, “An n-way hybrid power divider,” *IRE Trans. Microw. Theory Tech.*, vol. 8, no. 1, pp. 116-118, 1960.

[2] C. Liao, L. Chen, W. Lin, X. Zheng, and Y. Wu, “Design of an ultra-wideband power divider via the coarse-grained parallel micro-genetic algorithm,” *Progress In Electromagnetics Research*, vol. 124, pp. 425-440, 2012.

[3] J. Jin, X. Lin, X. Gao, X. Zhuang, and Y. Fan, “A dual-band power divider using parallel strip line with high isolation,” *Journal of Electromagnetic Waves and Applications*, vol. 26, pp. 1594-1601, 2012.

[4] J. Li, J. Nan, X. Shan, and Q. Yan, “A novel modified dual-frequency wilkinson power divider with open stubs and optional isolation,” *Journal of Electromagnetic Waves and Applications*, vol. 24, pp. 2223-2235, 2010.

[5] J. Li, Y. Wu, Y. Liu, J. Shen, S. Li, and C. Yu, “A generalized coupled-line dual-band wilkinson power divider with extended ports,” *Progress In Electromagnetics Research*, vol. 129, pp. 197-214, 2012.

[6] Y. Wu and Y. Liu, “An unequal coupled-line wilkinson power divider for arbitrary terminated impedances,” *Progress In Electromagnetics Research*, vol. 117, pp. 181-194, 2011.

[7] Z. Lin and Q. X. Chu, “A novel approach to the design of dual-band power divider with variable power dividing ratio based on coupled-lines,” *Progress In Electromagnetics Research*, vol. 103, pp. 271-284, 2010.

[8] B. Li, “Dual-band equal/unequal wilkinson power dividers based on coupled-line section with short-circuited stub,” *Progress In Electromagnetics Research*, vol. 111, pp. 163-178, 2011.

[9] Y. Wu, Y. Liu, and Q. Xue, "An analytical approach for a novel coupled-line dual-band wilkinson power divider," *IEEE Trans. Microw. Theory Tech.*, vol. 59, no. 2, pp. 286-294, 2011.

[10] P. Deng, J. Guo, and W. Kuo, "New wilkinson power dividers based on compact stepped-impedance transmission lines and shunt open stubs," *Progress In Electromagnetics Research*, vol. 123, pp. 407-426, 2012.

[11] H. Chen, and Y. Zhang, "A novel compact planar six-way power divider using folded and hybrid-expanded coupled lines," *Progress In Electromagnetics Research*, vol. 76, pp. 243-252, 2007.

[12] A. S. Al-Zayed and S. F. Mahmoud, "Seven ports power divider with various power division ratios," *Progress In Electromagnetics Research*, vol. 114, pp. 383-393, 2011.

[13] Y. Wu, Y. Liu, Q. Xue, S. Li, and C. Yu, "Analytical design method of multi-way dual-band planar power dividers with arbitrary power division," *IEEE Trans. Microw. Theory Tech.*, vol. 58, no. 12, pp. 3832-3841, 2010.

[14] Y. Wu, Y. Liu, S. Li, C. Yu, and X. Liu, "Closed-form design method of an n-way dual-band wilkinson hybrid power divider," *Progress In Electromagnetics Research*, vol. 101, pp. 97-114, 2010.

[15] H. R. Ahn, "Asymmetric passive components in microwave integrated circuits," New Jersey, *Wiley-Interscience*, chapter 7, pp. 170-185, 2006.

[16] S. Rosloniec, "Three-port hybrid power dividers terminated in complex frequency-dependent impedances," *IEEE Trans. Microw. Theory Tech.*, vol. 44, no. 8, pp. 1490-1493, 1996.

[17] X. Tang and K. Mouthaan, "Analysis and design of compact two-way wilkinson power dividers using coupled lines," *Asia–Pacific Microw. Conf.*, pp. 1319-1322, December 7-10, 2009.

[18] M. J. Park, "Two-section cascaded coupled line wilkinson power divider for dual-band applications," *IEEE Microw. Wireless Compon. Lett.*, vol. 19, no. 4, pp. 188-190, 2009.

[19] M. J. Park, "Dual-band wilkinson divider with coupled output port extensions," *IEEE Trans. Microw. Theory Tech.*, vol. 57, no. 9, pp. 2232-2237, 2009.

[20] M. Hayati, S. Roshani, and S. Roshani, "Miniaturized wilkinson power divider with nth harmonic suppression using front coupled tapered CMRC," *Applied Computational Electromagnetics Society (ACES) Journal*, vol. 28, no. 3, pp. 221-227, 2013.

[21] D. Hawatmeh, K. A. Shamaileh, and N. Dib, "Design and analysis of multi-frequency unequal-split wilkinson power divider using non-uniform transmission lines," *Applied Computational Electromagnetics Society (ACES) Journal*, vol. 27, no. 3, pp. 248-255, 2012.

[22] K. A. Shamaileh, A. Qaroot, N. Dib, and A. Sheta, "Design of miniaturized unequal split wilkinson power divider with harmonics suppression using non-uniform transmission lines," *Applied Computational Electromagnetics Society (ACES) Journal*, vol. 26, no. 6, pp. 530-538, 2011.

[23] Y. Wu, Y. Liu, and S. Li, "A dual-frequency transformer for complex impedances with two unequal sections," *IEEE Microw. Wireless Compon. Lett.*, vol. 19, no. 2, pp. 77-79, 2009.

[24] T. A. Milligan, "Transmission-line transformation between arbitrary impedances," *IEEE Trans. Microw. Theory Tech.*, vol. 24, no. 3, pp. 159, 1976.

[25] M. H. N. Potok, "Comments on transmission-line transformation between arbitrary impedances," *IEEE Trans. Microw. Theory Tech.*, vol. 25, no. 1, pp. 77, 1977.

Band-Rejected UWB Monopole Antenna with Bandwidth Enhancement

S. Ojaroudi [1], Y. Ojaroudi [1], N. Ojaroudi [2], and N. Ghadimi [2]

[1] Young Researchers and Elite Club
Islamic Azad University, Germi Branch, Germi, Iran

[2] Young Researchers and Elite Club
Islamic Azad University, Ardabil Branch, Ardabil, Iran
noradin.ghadimi@gmail.com

Abstract ─ In this study, we present an Ultra-Wideband (UWB) monopole antenna with band-notched function. The proposed antenna is fed by a microstrip line. By using two modified fork-shaped slots in the ground plane, bandwidth is increased that provides a wide usable fractional bandwidth of more than 135% (2.82-15.63). In order to achieve band-rejected performance, a cross-ring slot was inserted at the square radiating patch and a frequency band-notched of 5.11-5.97 GHz has been received. Simulated and experimental results obtained for this antenna show that it exhibits good radiation behavior within the UWB frequency range. The designed antenna has a small size.

Index Terms ─ Band-notched function, cross-ring slot, fork-shaped slot and UWB monopole antenna.

I. INTRODUCTION

In UWB communication systems, one of key issues is the design of a compact antenna while providing wideband characteristic over the whole operating band [1]. Consequently, a number of microstrip antennas with different geometries have been experimentally characterized. Moreover, other strategies to improve the impedance bandwidth, which do not involve a modification of the geometry of the planar antenna have been investigated [2-5].

The Federal Communication Commission (FCC)'s allocation of the frequency range 3.1-10.6 GHz for UWB systems and it will cause interference to the existing wireless communication systems, such as the Wireless Local Area Network (WLAN) for operating in 5.15-5.35 GHz and 5.725-5.825 GHz bands; so the UWB antenna with a single band-stop performance is required [6-9]. Lately, to generate the frequency band-notch function, modified planar monopoles several antennas with band-notch characteristic have been reported [10-13]. In [14], [15] and [16], different shapes of the parasitic structures (i.e., SRR, L-shaped and protruded strips) are used to obtain the desired band notched characteristics. H-ring conductor-backed plane structure is embedded in the antenna backside to generate the single and dual band-notched functions in [17].

In this paper, a new multi-resonance small monopole antenna with band-notched function is presented. In the proposed structure, by inserting a pair of fork-shaped slots in the ground plane, multi-resonance characteristic can be achieved. In order to generate a single band-notched function, we insert a modified cross-ring slot in the radiating patch. The designed antenna has a small size of 12×18 mm^2. Good VSWR and radiation pattern characteristics are obtained in the frequency band of interest.

II. ANTENNA DESIGN

Figure 1 shows the geometry of the proposed planar monopole antenna that is fed by microstrip line, which is printed on an FR4 substrate of thickness 1.6 mm, permittivity 4.4 and loss tangent 0.018. As shown in Fig. 1, the presented antenna

Submitted On: January 21, 2013
Accepted On: July 23, 2014

consists of a square radiating patch with a cross-ring slot and modified ground plane with two fork-shaped slots. The basic antenna structure consists of a square patch, a feed line and a ground plane. The square patch has a width of *W*. The square patch has a width of *W*. The patch is connected to a feed line with the width of W_f and the length of L_f. On the other side of the substrate, a conducting ground plane with the width of W_{Sub} and the length of L_{gnd} is placed. The proposed antenna is connected to a 50 Ω SMA connector for signal transmission.

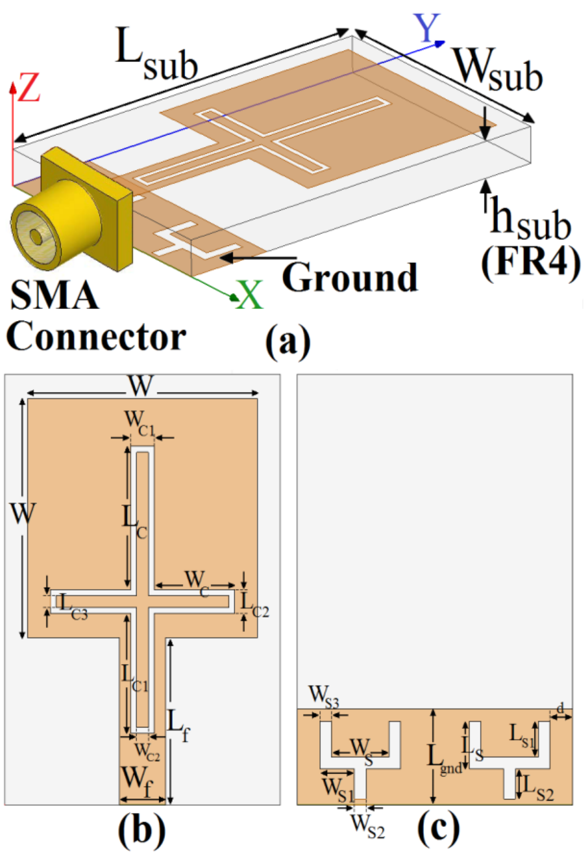

Fig. 1. Geometry of the proposed monopole antenna: (a) side view, (b) top layer and (c) bottom layer.

In this design, to achieve a multi-resonance function and give a bandwidth enhancement performance, two fork-shaped slots inserted in ground plane. By applying a cross-ring slot at radiating patch, a frequency band notch function (5.11-5.97 GHz WLAN) is generated. Regarding Defected Ground Structures (DGS), the creating slots in the ground plane provide an additional current path. Moreover, this structure changes the inductance and capacitance of the input impedance, which in turn leads to change the bandwidth. The DGS applied to a microstrip line causes a resonant character of the structure transmission with a resonant frequency controllable by changing the shape and size of the slot [18]. Therefore, by cutting two fork-shaped slots at the ground plane and carefully adjusting their parameters, much enhanced impedance bandwidth may be achieved. As illustrated in Fig. 1, to achieve a band-notched characteristic, the cross-ring slot is placed on the radiating patch. At the notched frequency, the current flows are more dominant around the cross-ring slot and they are oppositely directed between the slot and the radiation patch. As a result, the desired high attenuation near the notch frequency can be produced [19-20]. Final values of the presented antenna design parameters are specified in Table 1.

Table 1: The final dimensions of the antenna

Param.	W_{sub}	W	W_S	L_{S1}	W_{S3}	W_{C1}	L_{C2}
(mm)	12	10	2.5	2	0.5	1.5	1
Param.	L_{sub}	W_f	L_S	W_{S2}	W_C	L_{C1}	L_{C3}
(mm)	18	2	2	0.5	3.5	6	0.5
Param.	L_{gnd}	L_f	W_{S1}	L_{S2}	L_C	W_{C2}	d
(mm)	3.5	7	1.5	0.5	6	0.5	1

III. RESULTS AND DISCUSSIONS

In this section, the microstrip monopole antenna with various design parameters were constructed and the numerical and experimental results of the input impedance and radiation characteristics are presented and discussed. The proposed microstrip-fed monopole antenna was fabricated and tested to demonstrate the effect of the presented. Ansoft HFSS simulations are used to optimize the design and agreement between the simulation and measurement is obtained [21].

The configuration of the various antenna structures were shown in Fig. 2. VSWR characteristics for ordinary square monopole antenna, square monopole antenna with two fork-shaped slots in the ground plane and the proposed antenna structure are compared in Fig. 3. As shown in Fig. 3, it is observed that the upper frequency bandwidth is affected by using the fork-shaped slots in the ground plane and the notch frequency bandwidth is sensitive to the cross-ring slot at radiating patch.

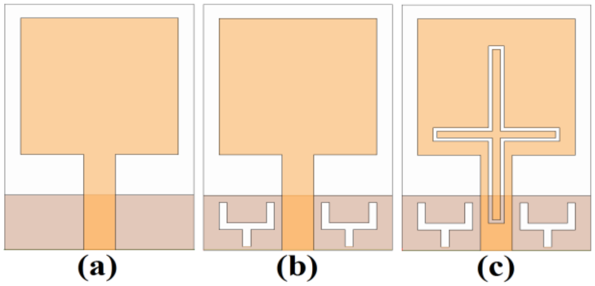

Fig. 2. (a) Basic structure (ordinary square monopole antenna), (b) antenna with a pair of fork-shaped slots in the ground plane and (c) the proposed antenna.

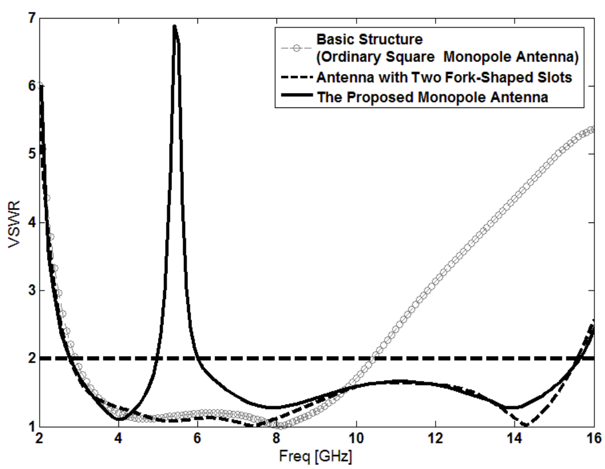

Fig. 3. Simulated VSWR characteristics for the various antennas shown in Fig. 2.

To understand the phenomenon behind this multi resonance performance, the simulated current distributions on the ground plane for the proposed antenna at 14.2 GHz are presented in Fig. 4 (a). It can be observed in Fig. 4 (a), that the current concentrated on the edges of the interior and exterior of two fork-shaped slots at 14.2 GHz. Therefore, the antenna impedance changes at these frequencies due to resonant properties of the fork-shaped slots [22-24]. Another important design parameter of this structure is cross-ring slot used at radiating patch. Figure 4 (b) presents the simulated current distributions in the radiating patch at the notch frequency (5.5 GHz). As shown in Fig. 4 (b), at the notch frequency the current flows are more dominant around of the cross-ring slot. As a result, the desired high attenuation near the notch frequency can be produced.

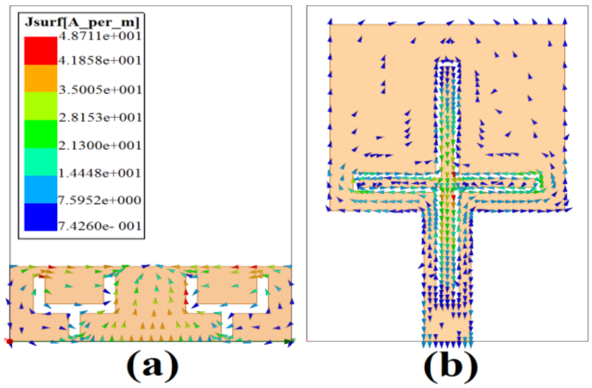

Fig. 4. Simulated surface current distributions for the proposed antenna: (a) on the ground plane at 14.2 GHz and (b) in the radiating patch at 5.5 GHz.

The measured and simulated VSWR characteristics of the proposed antenna were shown in Fig. 5. The fabricated antenna has the frequency band of 2.82 to over 14.63 GHz with notch band function around 5.11-5.97. Figure 6 illustrates the measured radiation patterns, including the co-polarization and cross-polarization in the H-plane (x-z plane) and E-plane (y-z plane). It can be seen that the radiation patterns in *x-z* plane are nearly omni-directional for the three frequencies [25-28].

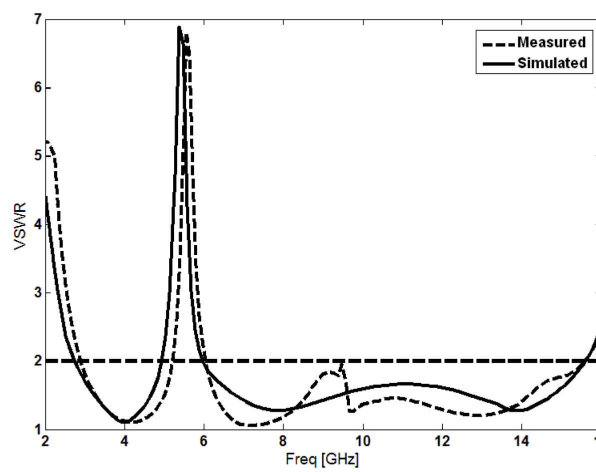

Fig. 5. Measured and simulated VSWR characteristics for the proposed antenna.

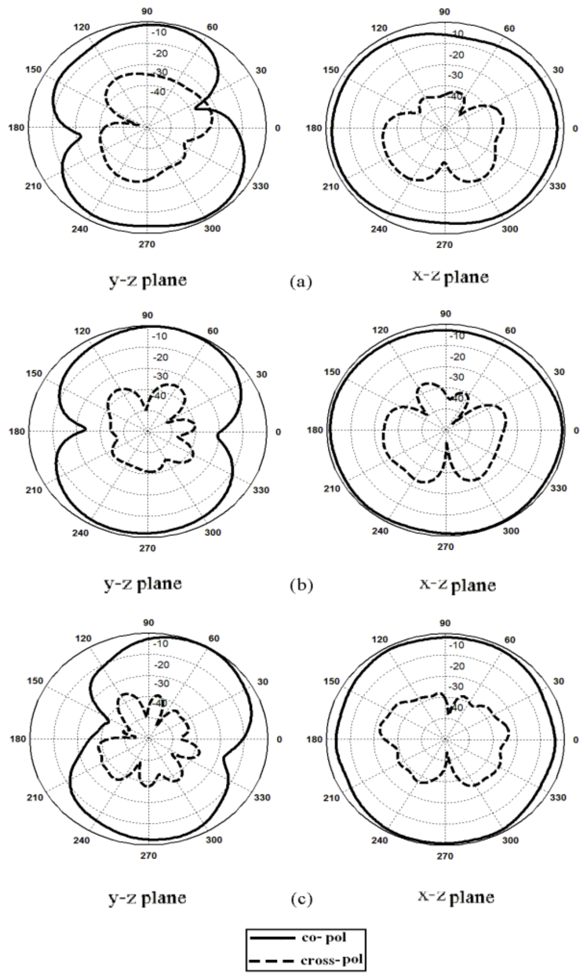

Fig. 6. Measured radiation patterns of the antenna: (a) 4 GHz, (b) 7 GHz and (c) 10 GHz.

IV. CONCLUSION

In this paper, we present a novel multi-resonance monopole antenna for UWB applications with band-notched performance. The proposed antenna can operate from 2.65 to 12.83 GHz with WLAN rejection band around 5.02-5.97 GHz. In order to enhance bandwidth, we insert two fork-shaped slots in the ground plane and also by using cross-ring slot at radiating patch a frequency band-notch function can be achieved. Simulated and experimental results show that the proposed antenna could be a good candidate for UWB applications.

ACKNOWLEDGMENT

The authors are thankful to MWT Company staff (www.microwave-technology.com).

REFERENCES

[1] M. J. Ammann, "Impedance bandwidth of the square planar monopole," *Microw. Opt. Technol. Lett.*, vol. 24, pp. 183-187, 2000.

[2] N. Ojaroudi, "Design of ultra-wideband monopole antenna with enhanced bandwidth," *21st Telecommunications Forum, TELFOR 2013*, Belgrade, Serbia, pp. 1043-1046, November 27-28, 2013.

[3] N. Ojaroudi, "A new design of koch fractal slot antenna for ultra-wideband applications," *21st Telecommunications Forum, TELFOR 2013*, Belgrade, Serbia, pp. 1051-1054, November 27-28, 2013.

[4] N. Ojaroudi, "Compact UWB monopole antenna with enhanced bandwidth using rotated l-shaped slots and parasitic structures," *Microw. Opt. Technol. Lett.*, vol. 56, pp. 175-178, 2014.

[5] N. Ojaroudi, S. Amiri, and F. Geran, "A novel design of reconfigurable monopole antenna for UWB applications," *Applied Computational Electromagnetics Society (ACES) Journal*, vol. 28, pp. 633-639, 2013.

[6] K. Chung, S. Hong, and J. Choi, "Ultra wide-band printed monopole antenna with band-notch filters," *IET Microw. Antennas, Propag.*, vol. 1, pp. 518-522, 2007.

[7] Q. Wu, R. Jin, J. Geng, and J. Lao, "Ultra-wideband rectangular disk monopole antenna with notched ground," *Electron. Lett.*, vol. 43, no. 11, pp. 1100-1101, May 2007.

[8] M. T. Partovi, N. Ojaroudi, and M. Ojaroudi, "Small slot antenna with enhanced bandwidth and band-notched performance for UWB applications," *Applied Computational Electromagnetics Society (ACES) Journal*, vol. 27, pp. 772-778, 2012.

[9] B. H. Siahkal-Mahalle, M. Ojaroudi, and N. Ojaroudi, "Enhanced bandwidth small square monopole antenna with band-notched functions for UWB wireless communications," *Applied Computational Electromagnetics Society (ACES) Journal*, vol. 27, pp. 759-765, 2012.

[10] A. Valizade, C. Ghobadi, J. Nourinia, N. Ojaroudi, and M. Ojaroudi, "Band-notch slot antenna with enhanced bandwidth by using Ω-shaped strips protruded inside rectangular slots for UWB applications," *Applied Computational Electromagnetics Society (ACES) Journal*, vol. 27, pp. 816-822, 2012.

[11] A. M. Montaser, K. R. Mahmoud, and H. A. Elmikati, "Integration of an optimized e-shaped patch antenna into laptop structure for bluetooth and notched-UWB standards using optimization techniques," *Applied Computational Electromagnetics Society (ACES) Journal*, vol. 27,

pp. 786-794, 2012.

[12] M. T. Partovi, N. Ojaroudi, M. Ojaroudi, and N. Ghadimi, "Enhanced bandwidth ultra-wideband small monopole antenna with variable band-stop function," *Applied Computational Electromagnetics Society (ACES) Journal*, vol. 27, pp. 1007-1013, 2012.

[13] N. Ojaroudi and N. Ghadimi, "Band-notched UWB slot antenna," *Microw. Opt. Technol. Lett.*, vol. 56, pp. 1744-1747, 2014.

[14] N. Ojaroudi, "Small microstrip-fed slot antenna with frequency band-stop function," *21st Telecommunications Forum, TELFOR 2013*, Belgrade, Serbia, pp. 1047-1050, November 27-28, 2013.

[15] N. Ojaroudi, "Application of protruded strip resonators to design an UWB slot antenna with WLAN band-notched characteristic," *Progress in Electromagnetics Research C*, vol. 47, pp. 111-117, 2014.

[16] N. Ojaroudi, N. Ghadimi, and Y. Ojaroudi, "UWB microstrip-fed slot antenna with band-rejection performance using an SRR conductor-backed plane," *Applied Computational Electromagnetics Society (ACES) Journal*, vol. 29, pp. 203-207, 2014.

[17] M. Ojaroudi, N. Ojaroudi, and S. A. Mirhashemi, "Bandwidth enhancement of small square monopole antenna with dual band-notch characteristics by using an h-ring slot and conductor backed plane for UWB applications," *Applied Computational Electromagnetics Society (ACES) Journal*, vol. 28, no. 1, pp. 64-70, 2013.

[18] N. Ojaroudi, N. Ghadimi and Y. Ojaroudi, "Planar Ultra-Wideband (UWB) Antenna with C-Band Rejection Using Self-Complementary Structures," *Applied Computational Electromagnetics Society (ACES) Journal*, vol. 29, pp. 203-207, 2014.

[19] N. Ojaroudi, "Microstrip monopole antenna with dual band-stop function for UWB applications," *Microw. Opt. Technol. Lett.*, vol. 56, pp. 818-822, 2014.

[20] N. Ojaroudi, "Circular microstrip antenna with dual band-stop performance for ultra-wideband systems," *Microw. Opt. Technol. Lett.*, vol. 56, pp. 2095-2098, 2014.

[21] "Ansoft high frequency structure simulation (HFSS)," ver. 13, *Ansoft Corporation*, 2010.

[22] N. Ojaroudi and N. Ghadimi, "Design of CPW-fed slot antenna for MIMO system applications," *Microw. Opt. Technol. Lett.*, vol. 56, pp. 1278-1281, 2014.

[23] N. Ojaroudi and N. Ghadimi, "Dual-band CPW-fed slot antenna for LTE and WiBro applications," *Microw. Opt. Technol. Lett.*, vol. 56, pp. 1013-1015, 2014.

[24] N. Ojaroudi and N. Ghadimi, "UWB multi-resonance antenna with rejection of intelligent transport system band using a cross-shaped conductor-backed plane," *Microw. Opt. Technol. Lett.*, vol. 56, pp. 1641-1644, 2014.

[25] N. Ojaroudi, S. Amiri, and F. Geran, "Reconfigurable monopole antenna with controllable band-notched performance for UWB communications," *20th Telecommunications Forum, TELFOR 2012*, Belgrade, Serbia, pp. 1176-1178, November 20-22, 2012.

[26] N. Ojaroudi, "Design of microstrip antenna for 2.4/5.8 GHz RFID applications," *German Microwave Conference, GeMic 2014*, RWTH, Aachen University, Germany, March 10-12, 2014.

[27] N. Ojaroudi, M. Mehranpour, S. Ojaroudi, and Y. Ojaroudi, "Microstrip-fed monopole antenna with triple band performance for WLAN/WiMAX applications," *Applied Computational Electromagnetics Society (ACES) Journal*, vol. 29, pp. 203-207, 2014.

[28] N. Ojaroudi, M. Mehranpour, S. Ojaroudi, and Y. Ojaroudi, "Application of the protruded structures to design an UWB slot antenna with band-notched characteristic," *Applied Computational Electromagnetics Society (ACES) Journal*, vol. 29, pp. 184-189, 2014.

A New Compact Rectangle-Like Slot Antenna with WiMAX and WLAN Rejection

M. Akbari [1,2], M. Khodaee [3], S. Zarbakhsh [1], and Abdelrazik Sebak [2]

[1] Young Researchers and Elite Club
Islamic Azad University, Central Tehran Branch, Tehran, Iran
akbari.telecom@gmail.com

[2] Electrical and Computer Department
Concordia University, Quebec H3G 1M8, Canada

[3] Faculty of Eng., Department of Electrical Engineering
Shahid Beheshti University, Tehran, Iran

Abstract **─** In this manuscript, a new CPW-fed slot antenna with two band-notches for ultra-wideband communication systems is proposed. The antenna contains a trapezoid-shaped patch and a slotted ground plane. To achieve two notched bands, both of the inverted L-shaped strip and triangle-shaped element connecting to patch by a via are used. The designed antenna is printed on an FR4 substrate with compact size of 20×27 mm^2. Moreover, the antenna has been successfully fabricated and measured, indicating extended impedance bandwidth (3-11.2 GHz, VSWR≤2) and dual band-notched (3.2-3.9 GHz and 5-5.9 GHz), respectively.

Index Terms **─** Coplanar Waveguide (CPW) antennas, notched band, Ultra-Wideband (UWB).

I. INTRODUCTION

In recent years, planar structures or printed antennas have attracted much attention due to the set of benefits including simple structure, low profile, easy integration with Monolithic Microwave Integrated Circuits (MMICs), and ease of fabrication. In spite of all these advantages, the narrow impedance bandwidth is one of the main challenges of antenna design. Newly, various techniques have been proposed to overcome the narrow bandwidth of these antennas. A big number of antennas with different structures have been experimentally characterized; which a patch of this type of reported antennas has different shapes, such as rectangular, Disc, triangle and oval forms [1-5]. There are many techniques that contain changes in configuration and geometry of patch, feed line, and ground structure, which is introduced as the most important of all to enhance the bandwidth and access to UWB bandwidth [6-7]. On the other hand, the frequency range for UWB systems between 3.1 and 10.6 GHz will end up interfering with the existing wireless communication systems, such as the Wireless Local Area Network (WLAN) for IEEE 802.11a operating at 5.15-5.35 and 5.725-5.825 GHz, the IEEE 802.16 WiMAX system at 3.3-3.69, 5.25-5.85 GHz; therefore, the UWB antenna with a band-stop performance is needed. For this goal, different techniques with single, dual, and multiple notch functions have been recently reported [8-12]. In this paper, a novel rectangle-like slot antenna with wide impedance bandwidth and dual band-notched characteristic is proposed. By employing both triangle-shaped coupling element and an inverted L-shaped strip, dual band-notch function can be achieved at the central frequencies 3.5 and 5.5 GHz.

II. ANTENNA DESIGN

The configuration and photo of the fabricated antenna are shown in Fig. 1, the proposed antenna has a compact size 20× 27 mm^2, which is printed on a FR4 substrate with thickness of 1.6 mm and

Submitted On: November 27, 2013
Accepted On: August 17, 2014

permittivity of 4.4. The only reason for using FR4 is its cheap cost. The width of the CPW feedline, Wf, and the gap between the ground and feedline g are fixed at 2.6 and 0.4 mm, respectively. The basic antenna structure contains a trapezoid-shaped patch and a slotted ground plane. As illustrated in Fig. 1, the rectangle-like slot of the ground plane has a width W1 and length L1 and the proposed antenna is connected to a 50 Ω SMA connector for signal transmission. To achieve two notched bands, two different techniques has been used; the former an inverted L-shaped strip for filtering 3.2 up to 3.9 GHz, the latter triangle-shaped coupling element on the back side which is connected to patch by a via for generating another notch from 5 up to 5.9 GHz, that both of them seem to be very sharp, which will be more examined as follows.

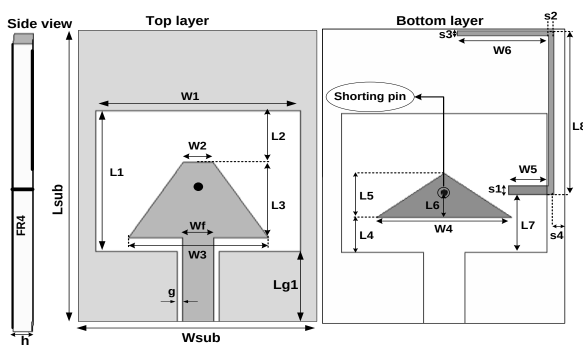

(a)

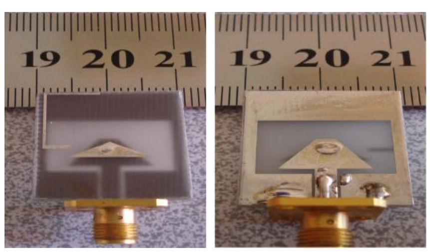

(b)

Fig. 1. (a) Geometry and (b) photo of the fabricated antenna.

III. ANTENNA PERFORMANCE AND DISCUSSION

This section is followed in two parts to include: time-domain analysis and frequency-domain analysis.

A. Time-domain analysis

Computation of the dispersion that occurs when the antenna radiates a pulse signal is also of interest. The transmit transfer functions of the antennas were used to compute the radiated pulse in different directions when a reference signal was applied at the antenna input. This signal should present an UWB spectrum covering the antenna bandwidth and particularly the FCC mask from 3.1 to 10.6 GHz. It is shown in Fig. 2 that an acceptable approximation to a FCC mask compliant pulse can be obtained with a Gaussian seventh derivative. This pulse is represented in the time domain by:

$$\mathrm{G(t)} = \mathrm{A.exp}\left(\frac{-\mathrm{t}^2}{2\delta^2}\right), \tag{1}$$

$$\mathrm{G^n(t)} = \frac{\mathrm{d^n G}}{\mathrm{dt^n}} = (-1)^{\mathrm{n}} \frac{1}{(\sqrt{2}\delta)^2} . \mathrm{H_n}\left(\frac{\mathrm{t}}{\sqrt{2}\delta}\right) . \mathrm{G(t)}, \tag{2}$$

$$\mathrm{H_7(t)} = 128\mathrm{t}^7 - 1344\mathrm{t}^5 + 3360\mathrm{t}^3 - 1680\mathrm{t}. \tag{3}$$

This signal and its spectrum are represented in Fig. 2. The pulse bandwidth is exactly into mask desired. Luckily, after drawing various Gaussian pulses from the first to eighth derivative, it was obtained that the best pulse for covering FCC mask can be the seventh derivative. Besides, with a bit tolerance, the sixth and eighth derivative are acceptable. In telecommunications systems, the correlation between the Transmitted (TX) and Received (RX) signals is evaluated using the fidelity factor (4):

$$\mathrm{F} = \max_\tau \left| \frac{\int_{-\infty}^{+\infty} \mathrm{S(t)r(t-\tau)dt}}{\sqrt{\int_{-\infty}^{+\infty} \mathrm{S(t)^2} \cdot \int_{-\infty}^{+\infty} \mathrm{r(t)^2 dt}}} \right|, \tag{4}$$

where S(t) and r(t) are the TX and RX signals, respectively. For impulse radio in UWB communications, it is necessary to have a high degree of correlation between the TX and RX signals to avoid losing the modulated information.

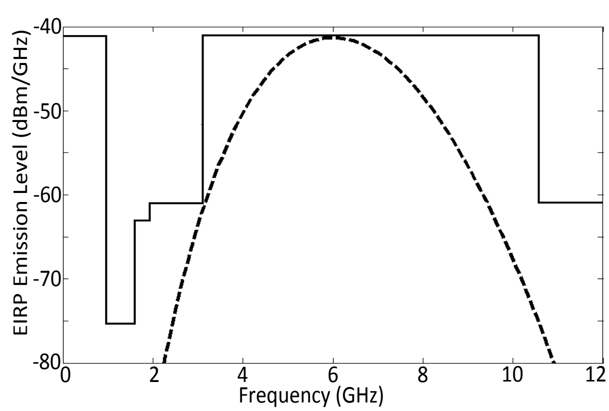

Fig. 2. Power spectrum density compared to FCC mask.

However, for most other telecommunication systems, the fidelity parameter is not that relevant. In order to evaluate the pulse transmission characteristics of the proposed antenna in the case of without notch, two configurations (side-by-side and face-to-face orientations) were chosen. The transmitting and receiving antennas were placed in a d=25 cm distance from each other [13].

As shown in Figs. 3 and 4, although the received pulses in each of the two orientations are broadened, a relatively good similarity exists between the RX and TX pulses. Using (4), the fidelity factor for the face-to-face and side-by-side configurations was obtained equal to 0.94 and nearly 0.96 in order. These values for the fidelity factor show that the antenna imposes negligible effects on the transmitted pulses. The pulse transmission results are obtained using CST [14].

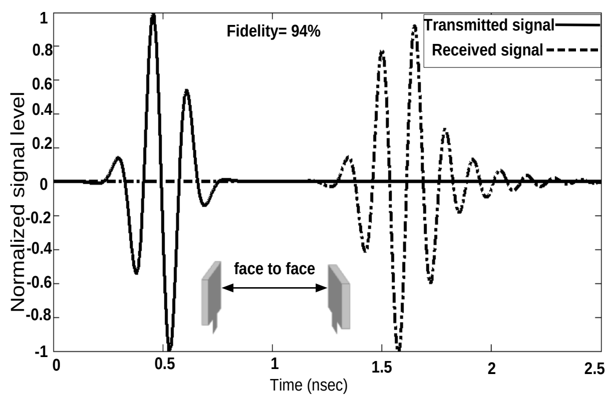

Fig. 3. Transmitted and received pulses in time domain for a UWB link with identical antennas without notches in face-to-face orientation.

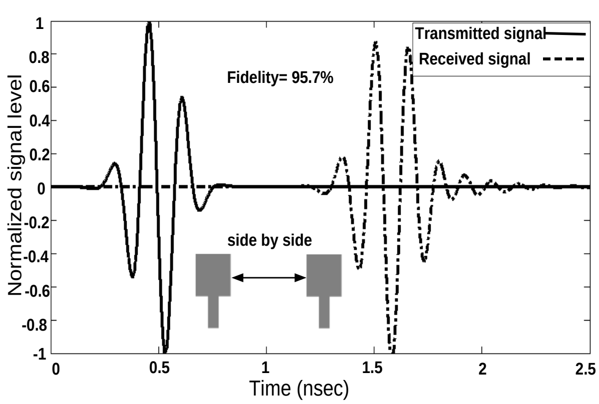

Fig. 4. Transmitted and received pulses in time domain for a UWB link with identical antennas without notches in side by side orientation.

B. Frequency-domain analysis

In UWB systems, the information is transmitted using short pulses. Therefore, it is important to study the temporal behavior of the transmitted pulse. The communication system for UWB pulse transmission must limit distortion, spreading and disturbance as much as possible. Group delay is an important parameter in UWB communication, which represents the degree of distortion of pulse signal. The key in UWB antenna design is to obtain a good linearity of the phase of the radiated field, because the antenna should be able to transmit the electrical pulse with minimal distortion. Usually, the group delay is used to evaluate the phase response of the transfer function because it is defined as the rate of change of the total phase shift with respect to angular frequency. Ideally, when the phase response is strictly linear, the group delay is constant.

$$\text{group delay} = \frac{-d\theta(w)}{dw}. \quad (5)$$

As depicted from Fig. 5, the group delay variation for the antenna is presented, which its variation is approximately flat and less than 0.6 ns over the frequency band of interest, except dual notched bands which ensure us pulse transmitted or received by the antenna will not distort seriously and will retain its shape. Hence, the antenna is useful for modern UWB communication systems. Phase S21 for face to face and side by side orientations are also illustrated in Figs. 6 and 7. As previously expected, the plot shows a linear variation of phase in the total operating band, except stop bands. It is important to note again that the distance between both the identical antennas in face to face and side by side orientations is 25 cm, which has been extracted from [14].

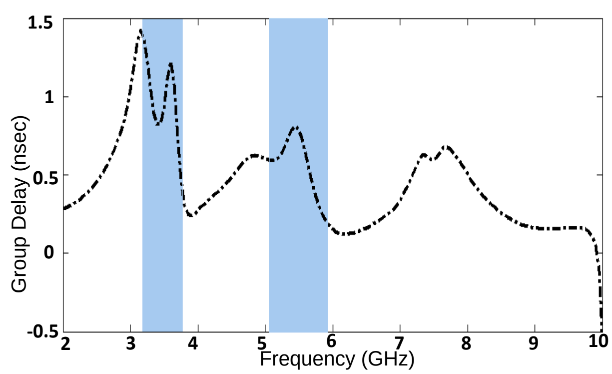

Fig. 5. Group delay of the antenna.

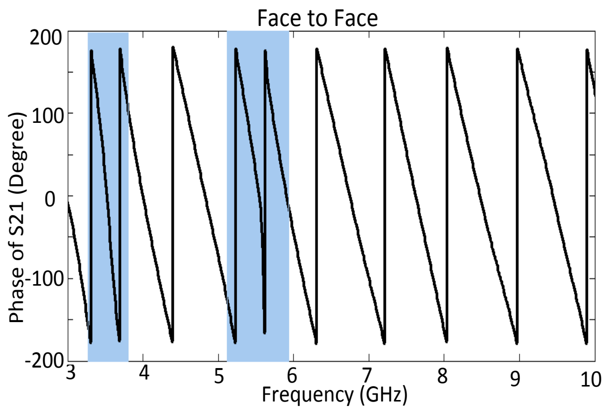

Fig. 6. Simulated phase S21 with a pair of identical antennas for face to face orientation.

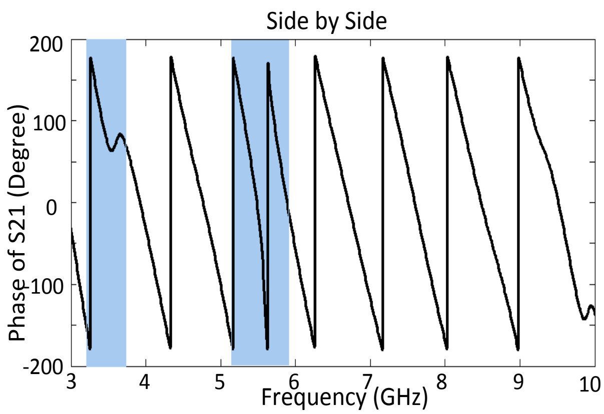

Fig. 7. Simulated phase S21 with a pair of identical antennas for side by side orientation.

In the following, the square antenna with different parameters were constructed, and the numerical and experimental results of the input impedance and radiation characteristics are presented and discussed.

The parameters of this proposed antenna are studied by changing one parameter at a time and fixing the others. The simulated results are achieved using the Ansoft simulation software high-frequency structure simulator [15]. The optimal dimensions of the antenna are demonstrated in Table 1. Figure 8 displays the structure of the different slot antennas including: (a) the simple slot antenna without notched bands, (b) the slot antenna with triangle-shaped coupling element which is connected to patch by a via, and (c) the proposed antenna. Meanwhile, Fig. 8 also illustrates the antenna topology. VSWR (Voltage Standing Wave Ratio) characteristics for three antennas mentioned in Fig. 8 are exhibited in Fig. 9. According to it, by using triangle-shaped coupling element, which is connected to patch by a via shown in Fig. 8 (b), the antenna can filter the WLAN interference band from 5 up to 5.9 GHz. Moreover, the inverted L-shaped strip on the back side shown in Fig. 8 (c), can create another notched band from 3.2 up to 3.9 GHz. There is an interesting point to note, that both of the notched bands obtained are approximately sharp and independent from each other. It means that they have no effect on each other. As depicted in Fig. 10, parameter W6 has a noticeable influence on frequency shifting. With regard to it, with increasing length W6, the center frequency is decreased regularly in a way that with rising 1.5 mm in length, W6 center frequency of the notched band is reduced about 0.5 GHz.

The best value W6 for covering 5.15 to 5.85 corresponds to 7.5 mm. As mentioned before, in this study to generate the band-stop performance on WiMAX band with center frequency 5.5 GHz, a triangle-shaped coupling element is used, which is connected to patch by a via. The simulated VSWR curves with different values W4 are plotted in Fig. 11. As exhibited in Fig. 11, when the length W4 increases gradually, center frequency of the notched band is diminished steadily. Thus, the optimized W4 is 11 mm. From these results, it can be found that the notch frequencies are controllable by changing the lengths W6 and W4. The proposed antenna was fabricated and tested in the Antenna Measurement Laboratory at Iran Telecommunication Research Center.

Table 1: Optimal dimensions of the antenna

Wsub	20	W5	3.3	L7	5.3
Lsub	27	W6	7.5	L8	14.9
h	1.6	L1	12.7	Lg1	6.6
Wf	2.6	L2	4.6	g	0.4
W1	16.8	L3	6.9	S1	0.8
W2	2.4	L4	3.2	S2	0.4
W3	11.5	L5	4	S3	0.4
W4	11	L6	2.25	S4	1

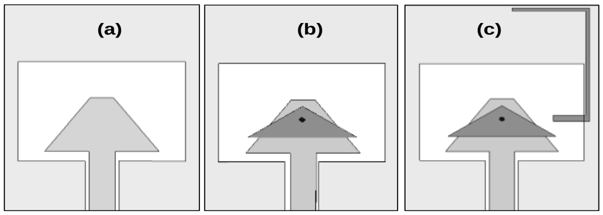

Fig. 8. (a) The simple slot antenna without notched bands, (b) the slot antenna with triangle-shaped element and via, and (c) the proposed antenna.

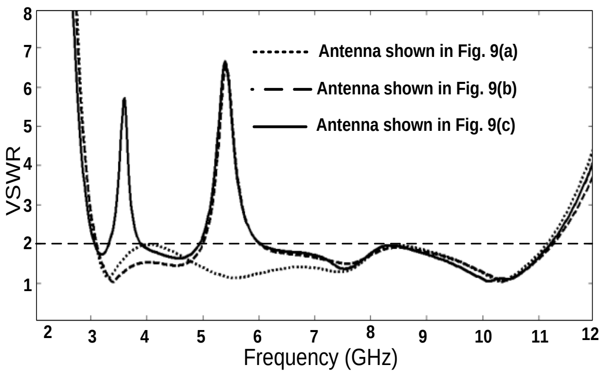

Fig. 9. Simulated VSWR characteristics for antennas shown in Fig. 8.

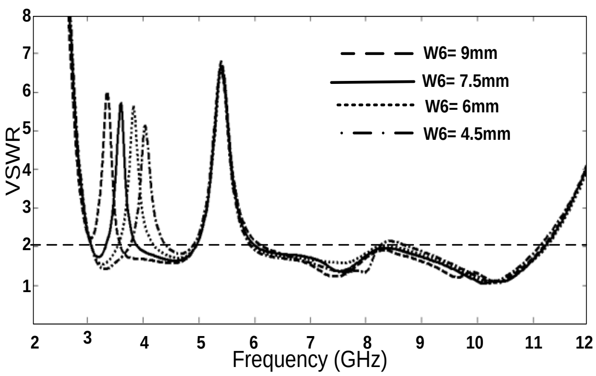

Fig. 10. VSWR characteristics for the antenna with different values W6.

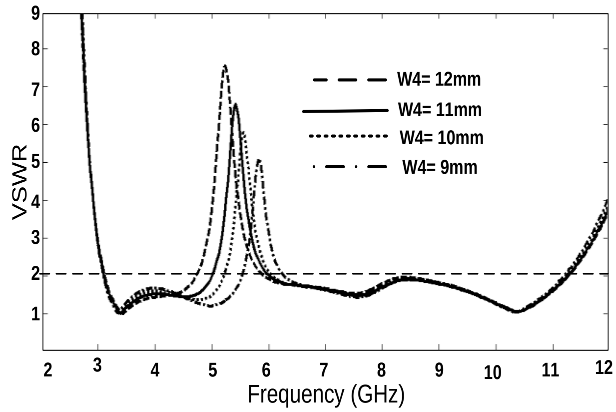

Fig. 11. Simulated VSWR characteristics of the antenna with triangle-shaped element and via with different values W4.

To clear more, Fig. 12 is used showing the simulated current distributions on both the sides of the antenna. It can also be observed in Fig. 12 (a), by using the triangle-shaped element, the current at 5.5 GHz is more concentrated on it and via. On the other hand, Fig. 12 (b) depicts the current distribution at 3.5 GHz in a way that most current is seen on L-shaped strip indicating its effect in creating the second notched band at center frequency 3.5 GHz. Figure 13 exhibits the measured and simulated VSWR characteristics of the antenna. The fabricated antenna can cover the frequency band from 3 to 11.2 GHz. The antenna has a compact size of 20×27 mm^2; whereas, showing the band rejection performance in the frequency bands of 3.2 up to 3.9 GHz and 5 to 5.9 GHz, respectively. As illustrated in Fig. 13, there is a discrepancy between measured result and simulated data; it is more likely due to the effect of the SMA port. The return loss of the antenna has been measured using an Agilent E8362B network analyzer in its full operational span (10 MHz-20 GHz).

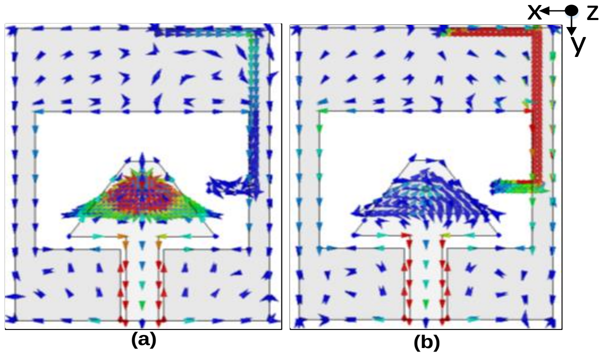

Fig. 12. Simulated current distributions: (a) on the triangle-shaped element and via at 5.5GHz and (b) on L-shaped strip at 3.5 GHz.

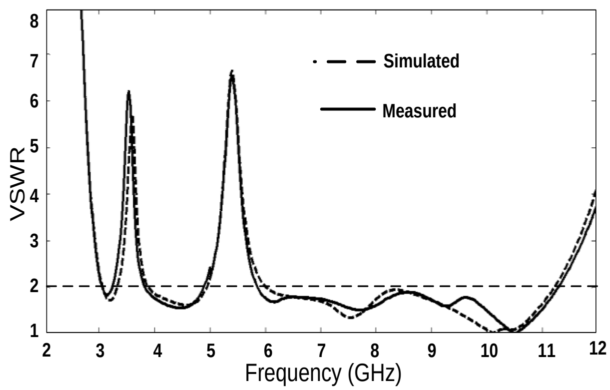

Fig. 13. Measured and simulated VSWR characteristics for the antenna.

To confirm the correct VSWR characteristics for the antenna, it is recommended that the manufacturing and measurement process need to be performed carefully. Figure 14 shows the measured gain of the antenna with and without stop bands. A sharp fall in gain of the antenna at the center frequencies of notched bands 3.5, 5.5 GHz, is seen. For other frequencies outside the notched frequency bands, the antenna gain with notch is similar to those without it. Figure 15 depicts the radiation patterns including the co-polarization and cross-polarization in the H-plane (x-z plane) and E-plane (y-z plane) at two frequencies, 4.5 GHz and 9 GHz. It can be observed that the radiation patterns in x-z plane are nearly omnidirectional for the two frequencies, while radiation patterns in y-z plane or E-plane are about dipole-like shape.

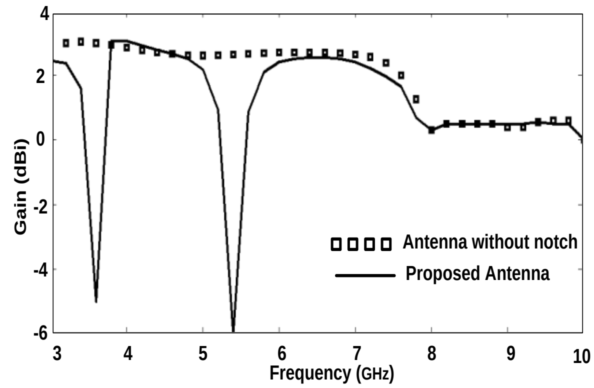

Fig. 14. Measured gain of the antenna without and with notched bands.

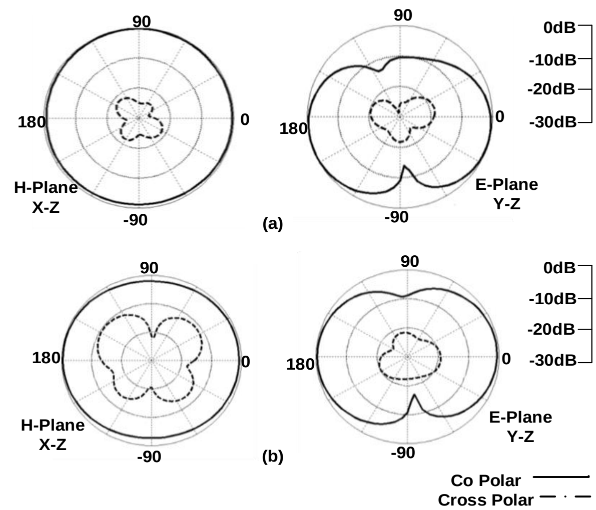

Fig. 15. Radiation patterns of the antenna at: (a) 4.5 and (b) 9 GHz.

IV. CONCLUSION

In this paper, a new CPW antenna with capability of broad impedance bandwidth for UWB applications is presented. The antenna can cover impedance bandwidth from 3 to 11.2 GHz with VSWR≤2, and indicates a good omnidirectional radiation pattern even at higher frequencies. The antenna has a compact size of 20×27 mm^2, while exhibiting the band stop performance in the frequency bands from 3.2 to 3.9 GHz and 5 up to 5.9 GHz, respectively. Simulated and experimental results exhibits that the antenna could be a good candidate for UWB application.

REFERENCES

[1] L. Jui-Han Lu and Y. Chih-Hsuan, "Planar broadband arc-shaped monopole antenna for UWB system," *IEEE Transactions on Antennas and Propagation*, vol. 60, no. 7, pp. 3091-3095, 2012.

[2] C. C. Lin, Y. C. Kan, L. C. Kuo, and H. R. Chuang, "A planar triangular monopole antenna for UWB communication," *IEEE Microwave and Wireless Components Letters*, vol. 15, no. 10, pp. 624-626, 2005.

[3] C. Y. Huang and W. C. Hsia, "Planar elliptical antenna for ultra-wideband communications," *Electronics Letters*, vol. 41, no. 6, pp.296-297, 2005.

[4] J. Liang, L. Guo, C. C. Chiau, X. Chen, and C. G. Parini, "Study of CPW-fed circular disc monopole antenna for ultra-wideband applications," *IEE Proceedings: Microwaves, Antennas and Propagation*, vol. 152, no. 6, pp. 520-526, 2005.

[5] Z. N. Chen, T. S. P. See, and X. Qing, "Small printed ultra-wideband antenna with reduced ground plane effect," *IEEE Transactions on Antennas and Propagation*, vol. 55, no. 2, pp. 383-388, 2007.

[6] M. Mighani, M. Akbari, and N. Felegari, "A novel SWB small rhombic microstrip antenna with parasitic rectangle into slot of the feed line," *Applied Computational Electromagnetics Society (ACES) Journal*, vol. 27, no. 1, pp. 74-79, January 2012.

[7] R. Zaker, C. Ghobadi, and J. Nourinia, "Bandwidth enhancement of novel compact single and dual band-notched printed monopole antenna with a pair of l-shaped slots," *IEEE Transactions on Antennas and Propagation*, vol. 57, no. 12, 2009.

[8] W. Jiang and W. Che, "A novel UWB antenna with dual notched bands for WiMAX and WLAN applications," *IEEE Antennas and Wireless Propagation Letters*, vol. 11, pp. 293-296, 2012.

[9] X. J. Liao, H. C. Yang, N. Han, and Y. Li, "Aperture UWB antenna with triple band-notched characteristics," *Electronics Letters*, vol. 47, no. 2, pp. 77-79, January 2011.

[10] M. Ojaroudi, S. Yazdanifard, N. Ojaroudi, and R. A. Sadeghzadeh, "Band-notched small square-ring antenna with a pair of t-shaped strips protruded inside the square ring for UWB applications," *IEEE Antennas and Wireless Propagation Letters*, vol. 10, pp. 227-230, 2011.

[11] R. Emadian, M. Mirmozafari, C. Ghobadi, and J. Nourinia, "Bandwidth enhancement of dual band-notched circle-like slot antenna," *Electronics Letters*, vol. 48, no. 7, pp. 356-357, March 2012.

[12] M. Mighani, M. Akbari, and N. Felegari, "A CPW dual band notched UWB antenna," *Applied Computational Electromagnetics Society (ACES) Journal*, vol. 27, no. 4, pp. 352-359, April 2012.

[13] C. R. Medeiros, J. R. Costa, and C. A. Fernandes, "Compact tapered slot UWB antenna with WLAN band rejection," *IEEE Antennas and Wireless Propagation Letters*, vol. 8, pp. 661-664, 2009.

[14] *CST Microwave Studio*, ver. 2008, "Computer simulation technology," Framingham, MA, 2008.

[15] "Ansoft HFSS user's manual," *Ansoft Corporation*, Beta Release 11.0, April 2007.

Mohammad Akbari was born on February 3, 1983 in Tehran, Iran. He received his B.Sc. degree in Engineering-Telecommunication from the University of Shahid Bahonar, Kerman, Iran, in 2007 and his M.Sc. degrees in Electrical Engineering-Telecommunication from the University of Urmia, Urmia, Iran in 2011. He has taught courses in microwave engineering, antenna theory, Fields & Waves, and electromagnetic at Aeronautical University, Tehran, Iran. He is currently pursuing his Ph.D. degree jointly at Concordia University, Montreal, Canada. His main field of research contains analysis and design of microstrip antennas, modeling of microwave structures, radar systems, electromagnetic theory and analysis of UWB antennas for WBAN applications, antenna interactions with human body, computational electromagnetics (time and frequency-domain methods), and microwave circuits and components. He is the author or co-author of approximately 40 peer-reviewed scientific journals and international conference papers. Akbari was awarded Graduate Concordia Merit Scholarship.

Meghdad Khodaee was born in Ilam, Iran, in 1986. He received his B.Sc. degree in Electrical and Electronic Engineering from Zanjan University, Zanjan, Iran, and his M.Sc. degrees in Electrical and Telecommunication Engineering from Shahid Beheshti Univesity, Tehran, Iran. His research interests include antenna theory, microwave active circuits and RF communication links.

Saman Zarbakhsh was born on January 7, 1984 in Tehran, Iran. He received his B.Sc. degree in Electrical Engineering at Azad University of South Tehran, Tehran, Iran, in 2007 and his M.Sc. degree in Electrical Engineering from Urmia University, Urmia, Iran, in 2010. His research interests contain antenna design, antenna miniaturization and broadband circular polarized antennas. He has taught courses in Electrical Engineering Department at Azad University of Shahr Rey University, Tehran, Iran.

Abdel Razik Sebak (F'10) received his B.Sc. degree (with honors) in Electrical Engineering from Cairo University, in 1976 and his B.Sc. degree in Applied Mathematics from Ein Shams University, in 1978. He received his M.Eng. and Ph.D. degrees from the University of Manitoba, in 1982 and 1984, respectively, both in Electrical Engineering. From 1984 to 1986, he was with the Canadian Marconi Company, working on the design of microstrip phased array antennas. From 1987 to 2002, he was a Professor in the Electrical and Computer Engineering Department, University of Manitoba. He is a Professor of Electrical and Computer Engineering at Concordia University. His current research interests include phased array antennas, computational electromagnetics, integrated antennas, electromagnetic theory, interaction of EM waves with new materials and bioelectromagnetics. Sebak received the 2000 and 1992 University of Manitoba Merit Award for Outstanding Teaching and Research, the 1994 Rh Award for Outstanding Contributions to Scholarship and Research, and the 1996 Faculty of Engineering Superior Academic Performance. He is a Fellow of IEEE. He has served as Chair for the IEEE Canada Awards and Recognition Committee (2002-2004), and the Technical Program Chair of the 2002 IEEE-CCECE and 2006 ANTEM conferences.

Electromagnetic Scattering by Multiple Cavities Embedded in the Infinite 2D Ground Plane

Peijun Li [1] and Aihua W. Wood [2]

[1] Department of Mathematics
Purdue University, West Lafayette, IN 47907, USA
lipeijun@math.purdue.edu

[2] Department of Mathematics and Statistics
Air Force Institute of Technology, WPAFB, Dayton, OH 45433, USA
aihua.wood@afit.edu

Abstract **─** This paper is concerned with the mathematical analysis and numerical computation of the electromagnetic wave scattering by multiple open cavities, which are embedded in an infinite two-dimensional ground plane. By introducing a new transparent boundary condition on the cavity apertures, the scattering problem is reduced to a boundary value problem on the two-dimensional Helmholtz equation imposed in the separated interior domains of the cavities. The existence and uniqueness of the weak solution for the model problem is studied by using a variational approach. A block Gauss-Seidel iterative method is introduced to solve the coupled system. Numerical examples are presented to show the efficiency and accuracy of the proposed method.

Index Terms **-** Electromagnetic cavity, finite element method, Helmholtz equation, variational formulation.

I. INTRODUCTION

A cavity is referred to as a local perturbation of the infinite ground plane. Given the cavity structure and an incident wave, the scattering problem is to predict the electromagnetic field scattered by the cavity. It has been extensively examined by researchers for the time-harmonic analysis of cavity-backed apertures with penetrable material filling the cavity interior [14-16, 18, 28]. Mathematical analysis of the problem including overfilled cavities, where the aperture is not planar and may protrude the ground plane, can be found in [1-4, 17, 19-24, 27]. A lot of work has been devoted to solve the problem by various numerical methods including finite element, finite difference, boundary element, and hybrid methods [5, 7, 8, 11, 12, 25, 26, 29, 30]. All the model problems have been focused on a single cavity, which may limit the application of the problem in industry and military. This paper aims to extend the single cavity model to a more general multiple cavity model, and analyze and develop numerical methods for the associated boundary value problem.

In this paper we focus on the Transverse Magnetic polarization (TM), where the modeling equation is the two-dimensional Helmholtz equation. Based on Fourier transform, a nonlocal transparent condition is introduced on the aperture, which connects the electric field in each individual cavity. By using the boundary condition, we reduce the multiple cavity problem into a boundary value problem imposed in the interiors of the cavities. The existence and uniqueness of the weak solution for the model problem is studied by using a variational approach. A block Gauss-Seidel iterative method is introduced to solve the coupled system, where only a single cavity problem needs to be solved at each iteration. Thus, it is applicable of any efficient single cavity solver to the multiple cavity problem. Numerical examples are presented to show the efficiency and accuracy of the proposed method. We refer to [9, 10, 13] for numerical methods to solve a related multiple obstacle scattering problem.

Submitted On: November 26, 2013
Accepted On: March 8, 2014

The paper is outlined as follows. In Section 2, a mathematical model for the single cavity problem is introduced, the variational formulation is presented, and the uniqueness and existence of the solution are examined. Section 3 is devoted to the study of the solution for the multiple cavity problem. The major new ingredient is the introduction of a transparent boundary condition. Section 4 addresses the numerical implementation and examples are shown to illustrate the method. The paper is concluded with some general remarks and directions for future research in Section 5.

II. SINGLE CAVITY SCATTERING

In this section, we study a single cavity problem, which is intended to serve as a basis for the multiple cavity problem.

A. Model problem

We focus on a two-dimensional geometry. The medium is assumed to be non-magnetic and has a constant magnetic permeability; i.e., $\mu = \mu_0$, where μ_0 is the magnetic permeability of vacuum. The medium is characterized by the dielectric permittivity ε.

As shown in Fig. 1, an open cavity Ω enclosed by the aperture Γ and the wall S, is placed on a perfectly conducting ground plane Γ^c. Above the flat surface $\{y=0\} = \Gamma \cup \Gamma^c$, the medium is assumed to be homogeneous with a positive dielectric permittivity ε_0. The medium inside the cavity is inhomogeneous with a variable dielectric permittivity $\varepsilon(x,y)$. Assume further that:

$$\varepsilon \in L^\infty(\Omega),\ \mathrm{Re}\,\varepsilon > 0,\ \mathrm{Im}\,\varepsilon \ge 0\,.$$

For the TM polarization, the magnetic field is transverse to the invariant direction. The time-harmonic Maxwell equations can be reduced to the two-dimensional Helmholtz equation:

$$\Delta u + \kappa^2 u = 0 \text{ in } \Omega \cup R_+^2\,. \tag{1}$$

The total field satisfies the boundary condition:

$$u = 0 \text{ on } \Gamma^c \cup S\,, \tag{2}$$

where $\kappa^2 = \omega^2 \varepsilon \mu_0$ is the wavenumber and ω is the angular frequency.

Let an incoming plane wave $u^i = e^{i\kappa_0(x\sin\theta - y\cos\theta)}$ be incident on the cavity from above, where θ is the incident angle with respect to the positive y axis, and $\kappa_0 = \omega\sqrt{\varepsilon_0\mu_0}$ is the wavenumber of the free space.

Denote the reference field u^{ref} as the solution of the homogeneous Helmholtz equation in the upper half space:

$$\Delta u^{ref} + {\kappa_0}^2 u^{ref} = 0 \text{ in } R_+^2\,, \tag{3}$$

together with boundary condition:

$$u^{ref} = 0 \text{ on } \Gamma^c \cup \Gamma\,. \tag{4}$$

It can be shown from (3) and (4) that the reference field consists of the incident field and the reflected field:

$$u^{ref} = u^i + u^r\,,$$

where $u^r = -e^{i\kappa_0(x\sin\theta + y\cos\theta)}$.

The total field is composed of the reference field and the scattered field:

$$u = u^{ref} + u^s.$$

It can be verified from (1) and (3) that the scattered field satisfies:

$$\Delta u^s + \kappa_0^2 u^s = 0 \text{ in } R_+^2\,. \tag{5}$$

In addition, the scattered field is required to satisfy the radiation condition:

$$\lim_{\rho\to\infty} \sqrt{\rho}\left(\frac{\partial u^s}{\partial\rho} - i\kappa_0 u^s\right) = 0, \rho = |(x,y)|\cdot \tag{6}$$

To describe the boundary value problem, we need to introduce some functional spaces. For $u \in L^2(\Gamma^c \cup \Gamma)$, which is identified with $L^2(R)$, we denote by $\hat{u}$ the Fourier transform of u defined as:

$$\hat{u}(\xi) = \int_R u(x) e^{ix\xi} dx.$$

Using Fourier modes, the norm on the space $L^2(R)$ can be characterized by:

$$\|u\|_{L^2(R)} = \left[\int_R |u|^2\, dx\right]^{\frac{1}{2}} = \left[\int_R |\hat{u}|^2\, d\xi\right]^{\frac{1}{2}}.$$

Denote the Sobolev space:

$$H^1(\Omega) = \{u : D^s u \in L^2(\Omega), \text{ for } |s| \le 1\}\,,$$

and the trace functional space:

$$H^s(R) = \{u \in L^2(R) : \int_R (1+\xi^2)^s\, |\hat{u}|^2\, d\xi < \infty\}\,,$$

whose norm is defined by:

$$\|u\|_{H^s(R)} = \left[\int_R (1+\xi^2)^s\, |\hat{u}|^2\, d\xi\right]^{\frac{1}{2}}\cdot$$

By taking the Fourier transform of (5) with respect to x, we obtain:

$$\frac{\partial^2 \hat{u}^s(\xi,y)}{\partial y^2} + (\kappa_0^2 - \xi^2)\hat{u}(\xi,y) = 0, y > 0. \tag{7}$$

Since the solution of (7) satisfies the radiation condition (6), we deduce that:

$$\hat{u}^s(\xi,y) = \hat{u}^s(\xi,0) e^{i\beta(\xi)y}\,, \tag{8}$$

where

$$\beta(\xi)=\begin{cases}(\kappa_0^2-\xi^2)^{\frac{1}{2}} \text{ for} |\xi|<\kappa_0,\\ i(\xi^2-\kappa_0^2)^{\frac{1}{2}} \text{ for} |\xi|>\kappa_0.\end{cases}$$

Taking the inverse Fourier transform of (8), we find that:

$$u^s(x,y)=\int_R \hat{u}^s(\xi,0)e^{i\beta(\xi)y}e^{-i\xi x}d\xi \text{ in } R_+^2.$$

Taking the normal derivative on $\Gamma^c \cup \Gamma$, which is the partial derivative with respect to y, and evaluating at $y=0$ yield:

$$\partial_y u^s(x,y)|_{y=0}=\int_R i\beta(\xi)\hat{u}(\xi,0)e^{-i\xi x}d\xi. \quad (9)$$

For given u on $\Gamma^c \cup \Gamma$, define the boundary operator T:

$$Tu=\int_R i\beta(\xi)\hat{u}(\xi,0)e^{-i\xi x}d\xi, \quad (10)$$

which leads to the transparent boundary condition for the scattered field on $\Gamma^c \cup \Gamma$:

$$\partial_y(u-u^{ref})=T(u-u^{ref}).$$

Equivalently we have a transparent boundary condition for the total field:

$$\partial_y u=Tu+g \text{ on } \Gamma^c \cup \Gamma, \quad (11)$$

where

$$g=\partial_y u^{ref}-Tu^{ref}=-2i\kappa_0\cos\theta e^{i\kappa_0 x\sin\theta}.$$

It can be shown that the boundary operator is continuous from $H^{\frac{1}{2}}(R)$ to $H^{-\frac{1}{2}}(R)$. Furthermore, it has the following properties which ensures the uniqueness of the solution of the single cavity problem.

Lemma 1. *Let* $u\in H^{\frac{1}{2}}(R)$. *It holds that* $\mathrm{Re}\langle Tu,u\rangle\le 0$ *and* $\mathrm{Im}\langle Tu,u\rangle\ge 0$. *Furthermore, if* $\hat{u}$ *is an analytical function with respect to* ξ, $\mathrm{Re}\langle Tu,u\rangle=0$ *or* $\mathrm{Im}\langle Tu,u\rangle=0$ *implies* $u=0$.

To derive a transparent boundary condition for the total field on the aperture Γ, we need to make the zero extension as follows: for any given u on Γ, define

$$\tilde{u}(x)=\begin{cases}u, x\in\Gamma,\\ 0, x\in\Gamma^c.\end{cases}$$

The zero extension is consistent with the problem since the ground plane is a perfectly electrical conductor. Based on the extension and the transparent boundary condition (11), we have the transparent boundary condition for the total field on the aperture:

$$\partial_y u=T\tilde{u}+g \text{ on } \Gamma. \quad (12)$$

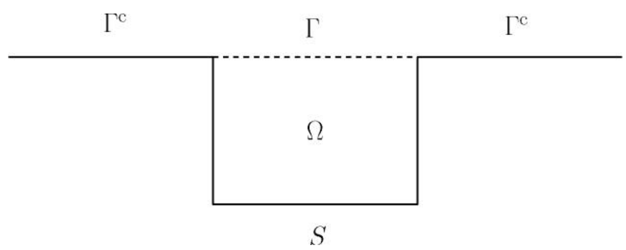

Fig. 1. The problem geometry of a single cavity.

B. Well-posedness

Define a trace functional space:

$$\tilde{H}^{\frac{1}{2}}(\Gamma)=\{u:\tilde{u}\in H^{\frac{1}{2}}(R)\},$$

whose norm is defined as the $H^{\frac{1}{2}}(R)$ norm for its extension; i.e.,

$$\|u\|_{\tilde{H}^{\frac{1}{2}}(\Gamma)}=\|\tilde{u}\|_{H^{\frac{1}{2}}(R)}.$$

Define a dual paring:

$$\langle u,v\rangle_\Gamma=\int_\Gamma u\bar{v}.$$

This dual paring for u and v is equivalent to the scalar product in $L^2(R)$ for their extensions; i.e.,

$$\langle u,v\rangle_\Gamma=\langle\tilde{u},\tilde{v}\rangle.$$

Denote by $H^{-\frac{1}{2}}(\Gamma)$ the dual space of $\tilde{H}^{\frac{1}{2}}(\Gamma)$; i.e., $H^{-\frac{1}{2}}(\Gamma)=(\tilde{H}^{\frac{1}{2}}(\Gamma))'$. The norm on this space is characterized by:

$$\|u\|_{H^{-\frac{1}{2}}(\Gamma)}=\sup_{\tilde{v}\in H^{\frac{1}{2}}(R)}\frac{\langle\tilde{u},\tilde{v}\rangle}{\|\tilde{v}\|_{H^{\frac{1}{2}}(R)}}.$$

Introduce a space:

$$H_S^1(\Omega)=\{u\in H^1(\Omega): u=0 \text{ on } S\},$$

which is a Hilbert space with the usual norm.

Multiplying a test function v on both sides of (1) and using the boundary conditions (2) and (12), we may deduce a variational problem: find u such that

$$a(u,v)=\langle g,v\rangle_\Gamma \text{ for all } v\in H_S^1(\Omega), \quad (13)$$

where the sesquilinear form is:

$$a(u,v)=\int_\Omega(\nabla u\cdot\nabla\bar{v}-\kappa^2 u\bar{v})-\langle T\tilde{u},v\rangle_\Gamma. \quad (14)$$

Theorem 1. *The variational problem (13) has a unique weak solution in* $H_S^1(\Omega)$ *and the solution* *satisfies the estimate:*

$$\|u\|_{H^1(\Omega)} \le C\|g\|_{H^{-\frac{1}{2}}(\Gamma)},$$

where C is a positive constant.

Proof: Decompose the sesquilinear form (14) into $a = a_1 - a_2$, where

$$a_1(u,v) = \int_\Omega \nabla u \cdot \nabla \bar{v} - \langle T\tilde{u}, \tilde{v} \rangle,$$

and

$$a_2(u,v) = \int_\Omega \kappa^2 u \bar{v}.$$

We conclude that from Lemma 1 and Poincare inequality that a_1 is coercive from:

$$\operatorname{Re} a_1(u,u) = \int_\Omega |\nabla u|^2 - \operatorname{Re}\langle T\tilde{u}, \tilde{v}\rangle \ge \int_\Omega |\nabla u|^2$$
$$\ge C\|u\|^2_{H^1(\Omega)} \text{ for all } u \in H^1_S(\Omega).$$

Next we prove the compactness of a_2. Define an operator $K : L^2(\Omega) \to H^1(\Omega)$ by:

$$a_1(Ku,v) = a_2(u,v) \text{ for all } v \in H^1_S(\Omega),$$

which explicitly gives that for all $v \in H^1_S(\Omega)$,

$$\int_\Omega \nabla Ku \cdot \nabla \bar{v} - \langle TK\tilde{u}, \tilde{v}\rangle = \int_\Omega \kappa^2 u \bar{v}.$$

Using the coercivity of a_1 and the Lax-Milgram lemma, it follows that:

$$\|Ku\|_{H^1(\Omega)} \le C\|u\|_{L^2(\Omega)}. \quad (15)$$

Thus, K is bounded from $L^2(\Omega)$ to $H^1(\Omega)$ and $H^1(\Omega)$ is compactly imbedded into $L^2(\Omega)$. Hence, $K : L^2(\Omega) \to L^2(\Omega)$ is a compact operator.

Define a function $w \in L^2(\Omega)$ by requiring $w \in H^1_S(\Omega)$ and satisfying:

$$a_1(w,v) = \langle g, v\rangle_\Gamma \text{ for all } v \in H^1_S(\Omega).$$

It follows from the Lax-Milgram lemma again that:

$$\|w\|_{H^1(\Omega)} \le C\|g\|_{H^{-\frac{1}{2}}(\Gamma)}. \quad (16)$$

Using the operator K, we can see that the variational problem (13) is equivalent to find $u \in L^2(\Omega)$ such that:

$$(I - K)u = w. \quad (17)$$

It follows from the uniqueness result and the Fredholm alternative that the operator $I - K$ has a bounded inverse. We then have the estimate:

$$\|u\|_{L^2(\Omega)} \le C\|w\|_{L^2(\Omega)}.$$

Combining (15)-(17), we deduce that:

$$\|u\|_{H^1(\Omega)} \le \|Ku\|_{H^1(\Omega)} + \|w\|_{H^1(\Omega)}$$
$$\le C\|u\|_{L^2(\Omega)} + \|w\|_{H^1(\Omega)}$$
$$\le C\|w\|_{H^1(\Omega)} \le C\|g\|_{H^{-\frac{1}{2}}(\Gamma)},$$

which completes the proof.

III. MULTIPLE CAVITY SCATTERING

As shown in Fig. 2, we consider a situation of n cavities, where the multiple open cavities $\Omega_1,\ldots,\Omega_n$ enclosed by the apertures $\Gamma_1,\ldots,\Gamma_n$ and the walls $S_1,\ldots,S_n$ are placed on Γ^c. Above the flat surface $\{y=0\} = \Gamma_1 \cup \cdots \cup \Gamma_n \cup \Gamma^c$, the medium is assumed to be homogeneous with a positive dielectric permittivity ε_0. The medium inside the cavity Ω_j is inhomogeneous with a variable dielectric permittivity $\varepsilon_j(x,y)$, which satisfies $\varepsilon_j \in L^\infty(\Omega)$, $\operatorname{Re}\varepsilon_j > 0$, $\operatorname{Im}\varepsilon_j \ge 0$ for $j = 1,\ldots,n.$

We consider the two-dimensional Helmholtz equation for the total field:

$$\Delta u + \kappa^2 u = 0, \text{ in } \Omega_1 \cup \cdots \cup \Omega_n \cup R^2_+, \quad (18)$$

together with the boundary condition:

$$u = 0, \text{ on } S_1 \cup \cdots \cup S_n \cup \Gamma^c. \quad (19)$$

Let the plane wave u^i be incident on the cavities from above. The total field u is consisted of the incident field u^i, the reflected field u^r, and the scattered field u^s, where the scattered field is required to satisfy the radiation condition (6).

To reduce the problem into the bounded domains $\Omega_j, j = 1,\ldots,n,$ we need to derive a transparent boundary condition on Γ_j. Rewrite (18)-(19) into n single cavity scattering problem:

$$\begin{aligned} \Delta u_j + \kappa_j^2 u_j &= 0 \text{ in } \Omega_j, \\ u_j &= 0 \text{ on } S_j, \end{aligned} \quad (20)$$

where $\kappa_j^2 = \omega^2 \varepsilon_j \mu_0$. If u is the solution of (18)-(19) and u_j is the solution of (20), respectively, then we have $u_j = u|_{\Omega_j}$ for $j = 1,\ldots,n.$

For $u_j(x,0)$, define its zero extension:

$$\tilde{u}_j(x,0) = \begin{cases} u_j(x,0) \text{ for } x \in \Gamma_j, \\ 0 \text{ for } x \in R \setminus \Gamma_j. \end{cases}$$

For the total field u, define its extension:

$$\tilde{u}(x,0) = \begin{cases} u_j(x,0) \text{ for } x \in \Gamma_j, \\ 0 \text{ for } x \in \Gamma^c. \end{cases}$$

It follows from the definition of the extensions that we have:

$$\tilde{u} = \sum_{j=1}^n \tilde{u}_j \text{ on } \Gamma_1 \cup \cdots \cup \Gamma_n \cup \Gamma^c.$$

Repeating the same steps as those for the single cavity problem, we have the following transparent boundary condition for the extended field:

$$\partial_y \tilde{u} = T\tilde{u} + g \text{ on } \Gamma_1 \cup \cdots \cup \Gamma_n \cup \Gamma^c, \quad (21)$$

which gives the transparent boundary for u_j:

$$\partial_y u_j = T\tilde{u}_j + \sum_{i=1, i\neq j}^{n} T\tilde{u}_i + g \text{ on } \Gamma_j. \quad (22)$$

As we can see from (22), the boundary condition for $u_j, j = 1,\ldots,n$ is coupled with each other, which is the major difference between the single cavity problem and the multiple cavity problem.

Next we present a variational formulation for the multiple cavity problem. Denote $\Omega = \Omega_1 \cup \cdots \cup \Omega_n$, $\Gamma = \Gamma_1 \cup \cdots \cup \Gamma_n$ and $S = S_1 \cup \cdots \cup S_n$. Define a trace functional space:

$$\tilde{H}^{\frac{1}{2}}(\Gamma) = \tilde{H}^{\frac{1}{2}}(\Gamma_1) \times \cdots \times \tilde{H}^{\frac{1}{2}}(\Gamma_n).$$

Its norm is characterized by:

$$\|u\|^2_{\tilde{H}^{\frac{1}{2}}(\Gamma)} = \sum_{j=1}^{n} \|u_j\|^2_{\tilde{H}^{\frac{1}{2}}(\Gamma_j)}.$$

Denote $H^{-\frac{1}{2}}(\Gamma) = H^{-\frac{1}{2}}(\Gamma_1) \times \cdots \times H^{-\frac{1}{2}}(\Gamma_n)$, which is the dual space of $\tilde{H}^{\frac{1}{2}}(\Gamma)$. The norm on the space is characterized by:

$$\|u\|^2_{H^{-\frac{1}{2}}(\Gamma)} = \sum_{j=1}^{n} \|u_j\|^2_{H^{-\frac{1}{2}}(\Gamma_j)}.$$

Introduce the space:

$$H^1_S(\Omega) = H^1_{S_1}(\Omega_1) \times \cdots \times H^1_{S_n}(\Omega_n),$$

which is a Hilbert space with norm characterized by:

$$\|u\|^2_{H^1(\Omega)} = \sum_{j=1}^{n} \|u_j\|^2_{H^1(\Omega_j)}.$$

Similarly, we may obtain the variational formulation for the multiple cavity problem: find $u \in H^1_S(\Omega)$ with $u_j = u|_{\Omega_j}$ such that

$$a(u,v) = \sum_{j=1}^{n} \langle g, v_j \rangle_{\Gamma_j} \text{ for all } v \in H^1_S(\Omega), \quad (23)$$

where the sesquilinear form is:

$$a(u,v) = \sum_{j=1}^{n} \int_{\Omega_j} (\nabla u_j \cdot \nabla \bar{v}_j - \kappa_j^2 u_j \bar{v}_j) - \sum_{j=1}^{n}\sum_{i=1}^{n} \langle T\tilde{u}_i, \tilde{v}_j \rangle.$$

We have the following well-posedness result. The proof is similar in nature as that of the single cavity problem and is omitted here for brevity.

Theorem 2. *The variational problem (23) has a unique weak solution in and the solution satisfies the estimate*:

$$\|u\|_{H^1(\Omega)} \leq C \|g\|_{H^{-\frac{1}{2}}(\Gamma)},$$

where C is a positive constant.

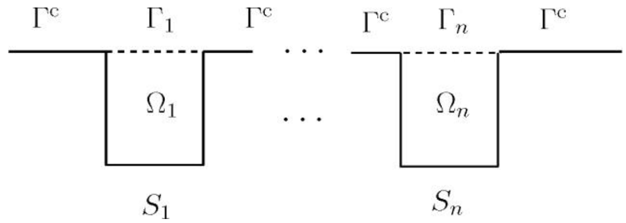

Fig. 2. The problem geometry for multiple cavities.

IV. NUMERICAL EXPERIMENTS

In this section, we discuss the computational aspects and present some examples for the multiple cavity problem.

A. Finite element formulation

Let M_j be a regular conforming triangulation of Ω_j and $V_j \subset H^1_{S_j}(\Omega_j)$ be the conforming linear finite element space over M_j. Denote $V = V_1 \times \cdots \times V_n$. The finite element approximation to the multiple cavity problem is to find u^h with $u^h \in V_j$ such that

$$a(u^h, v^h) = \sum_{j=1}^{n} \langle g, v_j^h \rangle_{\Gamma_j} \text{ for all } v^h \in V, \quad (24)$$

where the sesquilinear form

$$a(u^h, v^h) = \sum_{j=1}^{n} \int_{\Omega_j} (\nabla u_j^h \cdot \nabla \bar{v}_j^h - \kappa_j^2 u_j^h \bar{v}_j^h) - \sum_{j=1}^{n}\sum_{i=1}^{n} \langle T\tilde{u}_j^h, \tilde{v}_j^h \rangle.$$

For any $1 \leq j \leq n$, we denote by P_j the set of vertices of M_j, which are not on the cavity wall S_j, and let $\varphi_j(r) \in V_j$ be the nodal basis function belonging to vertex $r \in P_j$. Using the basis functions, the solution of (24) is represented as:

$$u_j^h = \sum_{r \in P_j} u_j(r) \varphi_j(r).$$

The discrete problem (24) is equivalent to the following system of algebraic equations:

$$AU = G, \quad (25)$$

where

$$A = \begin{bmatrix} A_1 - B_{1,1} & -B_{2,1} & \cdots & -B_{n,1} \\ -B_{1.2} & A_2 - B_{2,2} & \cdots & -B_{n,2} \\ \vdots & \vdots & \ddots & \vdots \\ -B_{1,n} & -B_{2,n} & \cdots & A_n - B_{n,n} \end{bmatrix},$$

$$U = (u_1, u_2, \ldots, u_n)^T,$$
$$G = (g_1, g_2, \ldots, g_n)^T.$$

Hence, each u_j is an unknown vector whose entries are $u_j(r) = u_j^h(r)$ for all $r \in P_j$, A_j is the stiffness matrix for the discrete problem and its entries are defined by:

$$A_j(r, r') = \int_{\Omega_j} [\nabla \varphi_j(r) \cdot \nabla \varphi_j(r') - \kappa_j^2 \varphi_j(r) \varphi_j(r')],$$

for all $r, r' \in P_j$. The entries of $B_{j,i}$ are defined by:

$$B_{j,i}(r, r') = \langle T\tilde{\phi}_i, \tilde{\phi}_j \rangle \text{ for all } r, r' \in P_j \cap \Gamma_j,$$

and the entries of each vector g_j are given by:

$$g_j(r) = \langle g, \varphi_j(r) \rangle_{\Gamma_j} \text{ for all } r \in P_j \cap \Gamma_j.$$

A block Gauss-Seidel method is adopted to solve (25). Given $U^{(0)}$, define $U^{(k)}, k \ge 1$ by the solution of the following system of equations:

$$(A_j - B_{j,j}) u_j^{(k)} = g_j + \sum_{i=1}^{j-1} B_{j,i} u_i^{(k)} + \sum_{i=j+1}^{n} B_{j,i} u_i^{(k-1)}, 1 \le j \le n. \tag{26}$$

The block Gauss-Seidel iteration (26) is equivalent to apply the finite element method to solve the following problem: let $u_j^{(0)} = 0$, define $u_j^{(k)}$ for $k \ge 1$ by the solutions of the decoupled equations

$$\begin{aligned} \Delta u_j^{(k)} + \kappa_j^2 u_j^{(k)} &= 0 \text{ in } \Omega_j, \\ u_j^{(k)} &= 0 \text{ on } S_j, \\ \partial_y u_j^{(k)} &= \sum_{i=1}^{j} T\tilde{u}_i^{(k)} + \sum_{i=j+1}^{n} T\tilde{u}_i^{(k-1)} + g \text{ on } \Gamma_j, \end{aligned} \tag{27}$$

for $j = 1, \ldots, n$. Therefore, we only need to solve a single cavity problem (27) at each iteration.

B. Transparent boundary condition

The transparent boundary conditions (11) and (22) are not convenient to be implemented numerically. We take an alternative and equivalent transparent boundary condition [7].

Let

$$G(r, r') = \frac{i}{4} [H_0^{(1)}(\kappa_0 \rho) - H_0^{(1)}(\kappa_0 \bar{\rho})]$$

be the Green function of the two-dimensional Helmholtz equation in the upper half space, where $H_0^{(1)}$ is the Hankel function of the first kind with order zero; $r = (x, y), r' = (x', y'), \rho = | r - r' |, \bar{\rho} = | r - \bar{r}' |$, and $\bar{r}' = (x', -y')$ is the image of r' with respect to the real axis. By the Green's theorem and the radiation condition, we obtain:

$$\partial_y u^s(x, 0) = \frac{i\kappa_0}{2} \int_\Gamma \frac{1}{| r - r' |} H_1^{(1)}(\kappa_0 | r - r' |) u^s(r', 0) dr',$$

where $H_1^{(1)}$ is the Hankel function of the first kind with order one. Hence, the alternative boundary condition is:

$$\partial_y u = Tu + g \text{ on } \Gamma, \tag{28}$$

where the boundary operator T is defined as:

$$Tu = \frac{i\kappa_0}{2} \int_\Gamma \frac{1}{| r - r' |} H_1^{(1)}(\kappa_0 | r - r' |) u(r', 0) dr'. \tag{29}$$

Here the integral is understood in the sense of Hadamard finite-part. For multiple cavities with apertures $\Gamma_1 \cup \cdots \cup \Gamma_n$, the boundary operator is defined as:

$$Tu = \frac{i\kappa_0}{2} \sum_{j=1}^{n} \int_{\Gamma_j} \frac{1}{| r - r' |} H_1^{(1)}(\kappa_0 | r - r' |) u(r', 0) dr'.$$

The boundary operator (29) can be approximated by:

$$Tu(x_i) \approx \sum_{k=1}^{m} g_{ik} u(x_k, 0),$$

where

$$\operatorname{Re} g_{ik} = -t_{ik} \frac{\kappa_0 | x_i - x_j |}{2} Y_1(\kappa_0 | x_i - x_j |),$$
$$\operatorname{Im} g_{ik} = \frac{\kappa_0 h_x}{2} \frac{J_1(\kappa_0 | x_i - x_j |)}{| x_i - x_k |},$$

and

$$t_{ik} = \begin{cases} \frac{1}{h_x}(1 - \ln 2) \text{ for} | i - k | = 1, \\ -\frac{2}{h_x} \text{ for} | i - k | = 0, \\ \frac{1}{h_x} \ln \frac{| i - k |^2}{| i - k |^2 - 1} \text{ for} | i - k | \ge 2, \end{cases}$$

where h_x is the step size of the partition for the cavity aperture Γ, Y_1 and J_1 are Bessel functions of the second and first kind with order one, respectively. Therefore, the boundary integral $\langle Tu, v \rangle$ in the weak formulation for the cavity problem can be approximated by any numerical quadratures.

C. Numerical examples

The physical parameter of interest is the Radar Cross Section (RCS), which is defined by:

$$\sigma = \frac{4}{\kappa_0} | P(\phi) |^2.$$

Here ϕ is the observation angle and P is the far-field coefficient given by:

$$P(\phi) = \frac{\kappa_0}{2}\sin\phi \int_{\Gamma} u(x,0)e^{i\kappa_0 x\cos\phi}dx.$$

When the incident and observation directions are the same, σ is called the backscatter RCS, which is defined by:

$$\text{Backscatter RCS } (\phi) = 10\log_{10}\sigma(\phi)\text{dB}.$$

Example 1. Consider a plane wave scattering from a rectangular cavity with 1 meter wide and 0.25 meters deep at normal incidence; i.e., $\theta = 0$. Two different cases are considered: an empty cavity with $\kappa = \kappa_0$ and a cavity filled with a homogeneous medium with $\kappa^2 = \kappa_0^2(4+i)$. These two cases have been considered as standard test problems in [14]. The Rectangular domain $[-0.5, 0.5]\times[-0.25, 0.0]$ is first divided into 160×40 small equal rectangles and then each small rectangle is subdivided into two equal triangles. Numerical results are obtained by using a linear finite element over triangles at the wavenumber $\kappa_0 = 2\pi$. Figures 3 and 4 show the magnitude and the phase of the total field on the aperture at the normal incidence, the backscatter RCS for the empty cavity and the filled cavity, respectively. We observe the coincidence of the numerical results obtained in [19] (circled) and our numerical method (solid line).

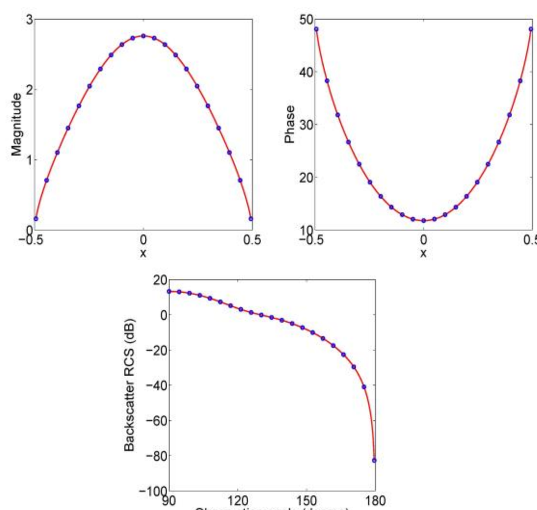

Fig. 3. The magnitude, phase, and backscatter RCS of the total field for Example 1 of the empty cavity.

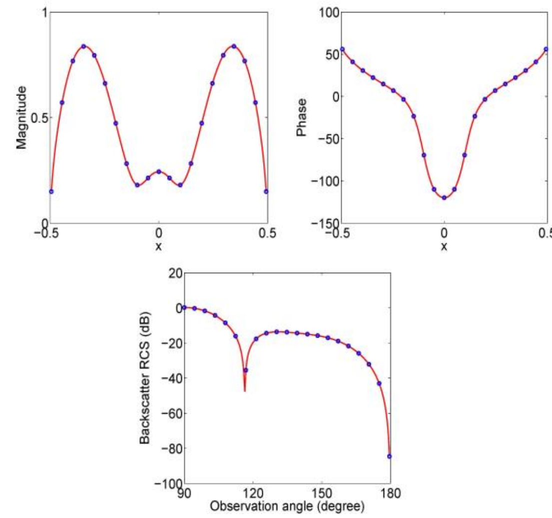

Fig. 4. The magnitude, phase, and backscatter RCS of the total field for Example 1 of the filled cavity.

Example 2. Consider the normal incidence of a plane wave onto two identical rectangular cavities. Each cavity is 1 meter wide and 0.25 meters deep; they are 1 meter distance away from each other. The two rectangular domains are given as follows:

cavity one: $[-1.5, -0.5]\times[-0.25, 0.0]$,

cavity two: $[0.5, 1.5]\times[-0.25, 0.0]$.

Each rectangular domain is divided into 160×40 small equal rectangles and then each small rectangle is subdivided into two equal triangles. Three types of cavities are considered: (type one) two empty cavities with $\kappa_1 = \kappa_2 = \kappa_0$; (type two) two filled cavities with $\kappa_1^2 = \kappa_2^2 = \kappa_0^2(4+i)$; (type three) one empty cavity with $\kappa_1 = \kappa_0$ and one filled cavity with $\kappa_2^2 = \kappa_0^2(4+i)$. Figures 5, 6 and 7 show the magnitude and the phase of the total field on the apertures at the normal incidence and the backscatter RCS for the type one, type two and type three cavities, respectively. These numerical results are obtained by the block Gauss-Seidel iterative method. To show the convergence of the iterative method, we define the error between two consecutive approximations:

$$e_k = \max_{1\le j\le k}\left\| u_j^{(k)} - u_j^{(k-1)} \right\|_{L^2(\Gamma_j)},$$

where k is the number of iteration. Figure 8 shows the error e_k of two consecutive approximations against the number of iterations for all three types of cavities. It can be seen from Fig. 8, that more number of iterations are needed for the type one cavities to reach the same level accuracy as the other two types of cavities. The reason is that the cavity for either type two or type three is filled with complex medium, which accounts for the absorption of the energy, and thus, the damping of the amplitude of the field.

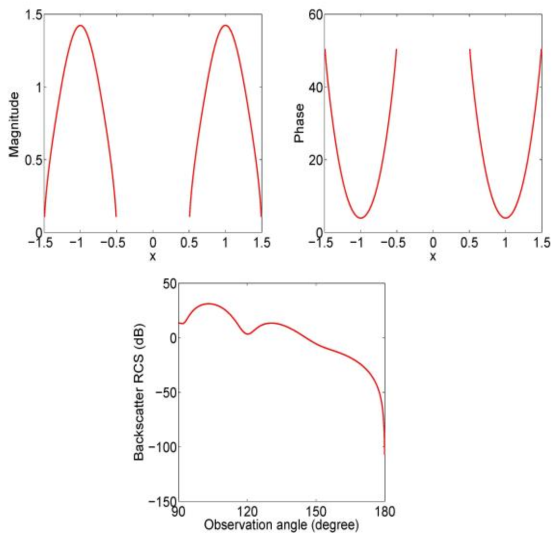

Fig. 5. The magnitude, phase, and backscatterer RCS for Example 2 of the type one cavity.

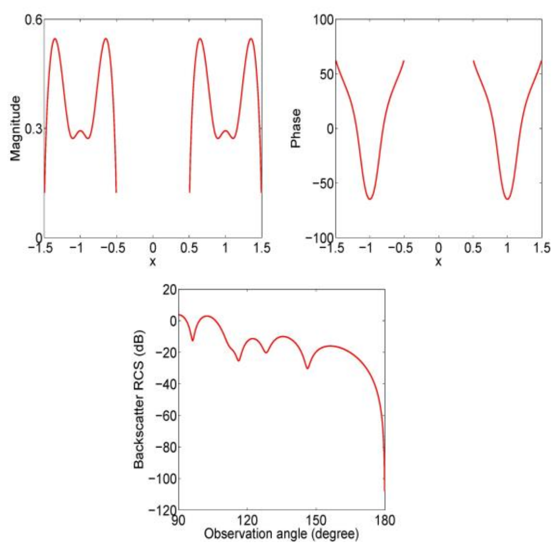

Fig. 6. The magnitude, phase, and backscatterer RCS for Example 2 of the type two cavity.

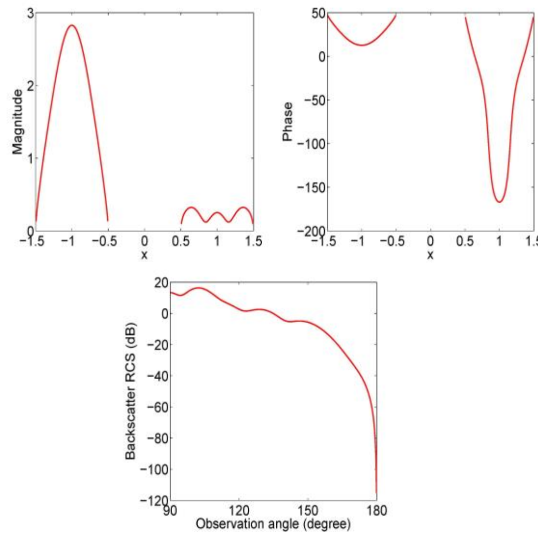

Fig. 7. The magnitude, phase, and backscatterer RCS for Example 2 of the type three cavity.

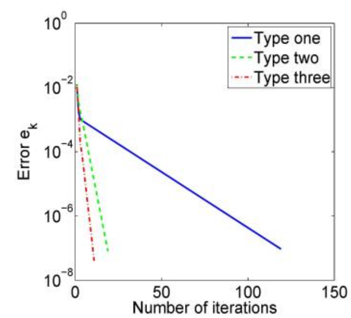

Fig 8. Convergence of the Gauss-Seidel iteration for Example 2.

Example 3. Consider the scattering of a triple cavity model. Let a plane wave be incident onto three identical rectangular cavities at the normal direction. Each cavity is 1 meter wide and 0.25 meters deep; there are 1 meter distance away from each other. The three rectangular domains are given as follows:

cavity one: $[-2.5, -1.5]\times[-0.25, 0.0]$,

cavity two: $[-0.5, 0.5]\times[-0.25, 0.0]$,

cavity three: $[1.5,\ 2.5]\times[-0.25, 0.0]$.

Again, each rectangular domain is divided into 160×40 small equal rectangles and then each small rectangle is subdivided into two equal triangles.

Cavities one and three are filled with the same homogeneous medium with $\kappa_1^2 = \kappa_3^2 = \kappa_0^2(4+i)$ and cavity two is an empty cavity with $\kappa = \kappa_0$. Figure 9 shows the magnitude and the phase of the total field on the apertures at the normal incidence and the backscatter RCS.

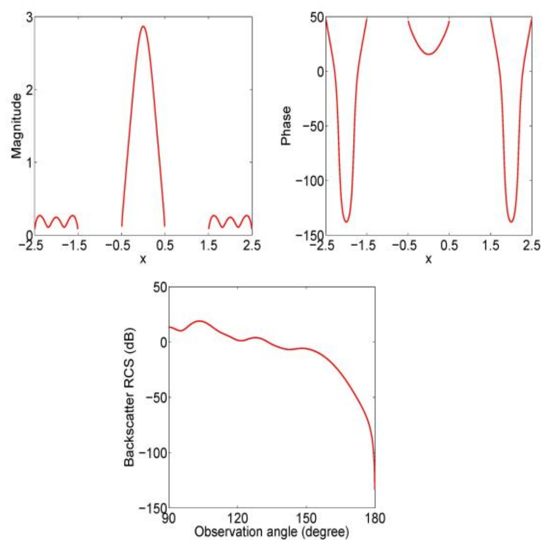

Fig 9. The magnitude, phase, and backscatter RCS of the total field for Example 3.

V. CONCLUSION

We studied the problem of electromagnetic scattering by multiple cavities embedded in the infinite two-dimensional ground plane. The scattering problem was reduced into a boundary value problem by introducing a transparent boundary condition. Based on the variational formulation, we proved the uniqueness and existence of the weak solution for the model problem. We employed a block Gauss-Seidel iterative method to decouple the coupled system arising from the multiple interaction among cavities. At each step of iteration, it required to solve only a single cavity problem. Three numerical examples were considered, a single cavity, two cavities and three cavities, with and/or without filling. The results show the convergence of the block Gauss-Seidel iterative method for the examples. We point out some future directions along the line of our present work. The first is to analyze the convergence of the Gauss-Seidel iterative method and investigate the parameters, such as separation distance among cavities, wavenumber and cavity size, which requires further mathematical analysis of the stability of the cavity scattering problem [6]. Another project is to study the multiple overfilled cavity problem and the model problem of three-dimensional Maxwell equations.

ACKNOWLEDGMENT

The research of PL was supported in part by NSF Grant DMS-115130. The research of AW was supported in part by AFOSR Grants F1ATA02059J001 and F1ATA01103J001.

REFERENCES

[1] H. Ammari, G. Bao, and A. Wood, "An integral equation method for the electromagnetic scattering from cavities," *Math. Meth. Appl. Sci.*, 23, pp. 1057-1072, 2000.

[2] H. Ammari, G. Bao, and A. Wood, "Analysis of the electromagnetic scattering from a cavity," *Jpn. J. Indus. Appl. Math.*, 19, pp. 301-308, 2001.

[3] H. Ammari, G. Bao, and A. Wood, "A cavity problem for maxwell's equations," *Meth. Appl. Anal.*, 9, pp. 249-260, 2002.

[4] G. Bao, J. Gao, and P. Li, "Analysis of direct and inverse cavity scattering problems," *Numer. Math. Theor. Meth. Appl.*, 4, pp. 419-442, 2011.

[5] G. Bao and W. Sun, "A fast algorithm for the electromagnetic scattering from a large cavity," *SIAM J. Sci. Comput.*, 27, pp. 553-574, 2005.

[6] G. Bao, K. Yun, and Z. Zhou, "Stability of the scattering from a large electromagnetic cavity in two dimensions," *SIAM J. Math. Anal.*, 44, pp. 383-404, 2012.

[7] K. Du, "Two transparent boundary conditions for the electromagnetic scattering from two-dimensional overfilled cavities," *J. Comput. Phys.*, 230, pp. 5822-5835, 2011.

[8] K. Du, "A composite preconditioner for the electromagnetic scattering from a large cavity," *J. Comput. Phys.*, 230, pp. 8089-8108, 2011.

[9] M. Grote and C. Kirsch, "Dirichlet-to-neumann boundary conditions for multiple scattering problems," *J. Comput. Phys.*, 201, pp. 630-650, 2004.

[10] K. Huang, P. Li, and H. Zhao, "An efficient algorithm for the generalized foldy-lax formulation," *J. Comput. Phys.*, 234, pp. 376-398, 2013.

[11] J. Huang and A. Wood, "Numerical simulation of electromagnetic scattering induced by an overfilled cavity in the ground plane," *IEEE Antennas Wireless Propag. Lett.*, 4, pp. 224-228, 2005.

[12] J. Huang, A. Wood, and M. Havrilla, "A hybrid finite element-laplace transform method for the

analysis of transient electromagnetic scattering by an over-filled cavity in the ground plane," *Commun. Comput. Phys.*, 5, pp. 126-141, 2009.

[13] X. Jiang and W. Zheng, "Adaptive uniaxial perfectly matched layer method for multiple scattering problems," *Comput. Methods Appl. Mech. Engrg.*, 201, pp. 42-52, 2012.

[14] J. Jin, "Electromagnetic scattering from large, deep, and arbitrarily-shaped open cavities," *Electromagnetics*, 18, pp. 3-34, 1998.

[15] J. Jin, J. Liu, Z. Lou, and S. Liang, "A fully high-order finite-element simulation of scattering by deep cavities," *IEEE Trans. Antennas Propag*., 51, pp. 2420-2429, 2003.

[16] J. Jin and J. L. Volakis, "A hybrid finite element method for scattering and radiation by micro strip patch antennas and arrays residing in a cavity," *IEEE Trans. Antennas Propag.*, 39, pp. 1598-1604, 1991.

[17] P. Li, H. Wu, and W. Zheng, "An overfilled cavity problem for maxwell's equations," *Math. Meth. Appl. Sci.*, 35, pp. 1951-1979, 2012.

[18] J. Liu and J. M. Jin, "A special higher order finite-element method for scattering by deep cavities," *IEEE Trans. Antennas Propag.*, 48, pp. 694-703, 2000.

[19] T. Van and A. Wood, "Finite element analysis for 2-D cavity problem," *IEEE Trans. Antennas Propag.*, 51, pp. 1-8, 2003.

[20] T. Van and A. Wood, "Analysis of time-domain maxwell's equations for 3-D electromagnetic cavities," *Adv. Comput. Math.*, 16, pp. 211-228, 2002.

[21] T. Van and A. Wood, "A time-domain finite element method for 2-D cavities," *J. Comput. Phys.*, 183, pp. 486-507, 2002.

[22] T. Van and A. Wood, "A time-marching finite element method for an electromagnetic scattering problem," *Math. Meth. Appl. Sci.*, 26, pp. 1025-1045, 2003.

[23] T. Van and A. Wood, "Finite element analysis of transient electromagnetic scattering from 2D cavities," *Methods Appl. Anal.*, 11, pp. 221-236, 2004.

[24] T. Van and A. Wood, "Analysis of transient electromagnetic scattering from overfilled cavities,"| *SIAM J. Appl. Math.*, 64, pp. 688-708, 2004.

[25] Y. Wang, K. Du, and W. Sun, "A second-order method for the electromagnetic scattering from a large cavity," *Numer. Math. Theor. Meth. Appl.*, 1, pp. 357-382, 2008.

[26] Y. Wang, K. Du, and W. Sun, "Preconditioning iterative algorithm for the electromagnetic scattering from a large cavity," *Numer. Linear Algebra Appl.*, 16, pp. 345-363, 2009.

[27] A. Wood, "Analysis of electromagnetic scattering from an overfilled cavity in the ground plane," *J. Comput. Phys.*, 215, pp. 630-641, 2006.

[28] W. Wood and A. Wood, "Development and numerical solution of integral equations for electromagnetic scattering from a trough in a ground plane," *IEEE Trans. Antennas Propag.*, 47, pp. 1318-1322, 1999.

[29] M. Zhao, Z. Qiao, and T. Tang, "A fast high order method for electromagnetic scattering by large open cavities," *J. Comput. Math.*, 29, pp. 287-304, 2011.

[30] D. Zhang, F. Ma, and H. Dong, "A finite element method with rectangular perfectly matched layers for the scattering from cavities," *J. Comput. Math.*, 27, pp. 812-834, 2009.